Prediction and Modelling of Snow Accumulation on Commercial Vehicles using CFD Simulations and Experimental Methods

Master's thesis in Automotive Engineering

DIMITRIOS KOUTSIMANIS
LUKASZ SOBIERAJ

DEPARTMENT OF MECHANICS AND MARITIME SCIENCES

CHALMERS UNIVERSITY OF TECHNOLOGY
Gothenburg, Sweden 2021
www.chalmers.se

MASTER'S THESIS IN AUTOMOTIVE ENGINEERING

Prediction and Modelling of Snow Accumulation on Commercial Vehicles using CFD Simulations and Experimental Methods

DIMITRIOS KOUTSIMANIS
LUKASZ SOBIERAJ

Department of Mechanics and Maritime Sciences
Division of Fluid Dynamics
CHALMERS UNIVERSITY OF TECHNOLOGY

Göteborg, Sweden 2021

Prediction and Modelling of Snow Accumulation on Commercial Vehicles using CFD Simulations and Experimental Methods
DIMITRIOS KOUTSIMANIS
LUKASZ SOBIERAJ

Master's thesis 2021:47
Department of Mechanics and Maritime Sciences
Division of Fluid Dynamics
Chalmers University of Technology
SE-412 96 Göteborg
Sweden
Telephone: +46 (0)31-772 1000

Cover:
Snow pattern predicted using the simplified multiphase method at the front of a Volvo FH truck.

Chalmers Reproservice
Göteborg, Sweden 2021

Prediction and Modelling of Snow Accumulation on Commercial Vehicles using CFD Simulations and Experimental Methods
Master's thesis in Automotive Engineering
DIMITRIOS KOUTSIMANIS
LUKASZ SOBIERAJ
Department of Mechanics and Maritime Sciences
Division of Fluid Dynamics
Chalmers University of Technology

Abstract

Snow contamination poses great challenges for the uninterrupted operation of commercial vehicles. The purpose of this project has been to contribute towards a better understanding of the properties and mechanisms that drive snow accumulation on commercial vehicles. Computational Fluid Dynamics (CFD) tools and simple experimental methods were utilized.

Initially, the idea of using only aerodynamic properties to predict snow accumulation was explored. The flow velocity was used to approximate the snow particle impact velocity and wall shear stress was used as the snow removing force. However, utilizing flow velocity proved to be challenging given the available tools and using only wall shear stress did not give accurate predictions. Therefore, a passive scalar was used to approximate snow. A method combining the passive scalar with wall shear stress was created. The performance of the method was enhanced by incorporating surface temperature data from field tests. Additionally, snow accumulation was influenced by surface orientation, i.e. the direction and inclination of the vehicle's surfaces could either help or hinder snow packing. The method was validated against infield test data, achieving satisfactory agreement in most sections of the vehicle. Studying snow-surface interaction was deemed too complicated and therefore it was decided to substitute snow with ice cubes. Simple experiments were performed to investigate the effects of temperature and surface material, as well as the influence of adhesion on ice-surface friction. The behaviour of ice varied significantly depending on temperature and material. The effect of adhesion varied between materials, contributing to higher values of static friction coefficient around the melting point of ice. At lower temperatures the effect of adhesion was less significant.

Angle of repose experiments were performed using artificially created snow. The effects of ambient temperature, surface material and snow fall height were investigated. It was observed that as temperature increased, larger angle of repose was obtained. Additionally, an increase in fall height resulted in smaller angle of repose. Differences in the angle of repose were observed also for the different surface materials that were tested. The possibility of replicating snow with substitute materials was also assessed. It was found that the behaviour of the tested substitute materials was influenced mainly by the shape and size of their grains.

A multiphase model was developed to study the physics of adhesive ice particles in detail. Discrete Element Method was chosen as the most suitable framework. Data obtained from the experiments were utilized to allow for a direct comparison between the CFD and test results. Sensitivity analysis was performed for inter-particle static friction coefficient, tangential restitution and rolling resistance model. It was found that an increase in inter-particle static friction coefficient resulted in a linear increase of the angle of repose. It was observed that as the tangential restitution coefficient increased, more time was needed to obtain the final angle of repose. Because all simulations had the same time limit, the angles of repose obtained in some cases were not stabilized and prevented the establishment of a trend. In the case of the rolling resistance model, it was found that the constant torque model resulted in smaller angle of repose compared to the force proportional model.

Keywords: Computational Fluid Dynamics, Discrete Element Method, Commercial Vehicles, Snow Contamination, Angle of Repose, Adhesion, Multiphase Flow

Preface

The following report covers the work performed during the Master's thesis project in the field of fluid dynamics. The project accounts for 2 × 30 ECTS and was carried out as an obligatory part of the Master's Programme at Chalmers University of Technology in Gothenburg, Sweden. The project took place between January and June 2021 at Volvo Group Trucks Technology on their behalf to investigate and develop the analysis methods for predicting snow contamination on the external surfaces of commercial vehicles developed by the company. The work was conducted both at the premises of Volvo GTT in Gothenburg and remotely. CFD Analysis Engineer Johan Forsgren was supervising the project on behalf of Volvo GTT. Professor Srdjan Sasic (Division of Fluid Dynamics, Department of Mechanics and Maritime Sciences, Chalmers University of Technology) was an examiner of the Master's thesis project.

Acknowledgements

We would like to express our gratitude to our supervisor, Johan Forsgren, for his constant assistance, engagement and motivation during this Master's thesis. His insightful remarks and comments made the learning process both effective and pleasant. Moreover, we would like to thank our examiner, Prof. Srdjan Sasic, for his valuable feedback. His interest in the project resulted in several enlightening discussions that allowed us to get deeper understanding of the topic.

Furthermore, we would like to acknowledge Anton Lundberg for the continuous support throughout the project. Also, we would like to thank Manel Galan Losada who was carrying out his project simultaneously for making the process enjoyable. Although the situation did not allow us to carry out the entire project at the office, we would like to acknowledge all the colleagues in the Cab Analysis group at Volvo for welcoming us. We would like to acknowledge Peter Rundberget for the involvement and making us feel part of the team.

Our gratitude extends to Elin Dornerus for the help with testing materials and providing feedback to our testing method and Amelie Eldh for providing us with the thermal camera photos. Also, we would like to thank Nils Johanson and Mikael Palmqvist for their help during the experimental part of our project.

Finally, we would like to express our appreciation to our families and friends for their constant support and motivation both during this project and throughout our former education.

Lukasz Sobieraj and Dimitrios Koutsimanis, Gothenburg, June 2021

Nomenclature

Symbols and Constants

α	$[°]$	Angle
Γ	$[J/m^2]$	Work of cohesion
δ	$[m]$	Overlap at the point of contact
ε	$[m^2/s^3]$	Turbulent dissipation rate
η	$[(F \cdot s)/m]$	Damping
η	$[-]$	Damping coefficient
θ	$[°C]$	Temperature
κ	$[m^2/s]$	Diffusivity
μ	$[kg/(m \cdot s)]$	Dynamic viscosity
μ	$[-]$	Friction coefficient
μ	$[m]$	Mean diameter
μ	$[-]$	Tabor number
μ_r	$[-]$	Coefficient of rolling resistance
ν, ν_t	$[m^2/s]$	Kinematic viscosity, Turbulent kinematic viscosity
ν	$[-]$	Poisson's modulus
ρ	$[kg/m^3]$	Density
σ	$[-]$	Standard deviation
τ_{xp}	$[s]$	Particle response time
τ_{ij}	$[Pa]$	Viscous stress tensor component
τ_w	$[Pa]$	Wall shear stress
τ	$[s]$	Time step
ϕ	$[-]$	Passive scalar field
ϕ^*	$[-]$	Effective quantity
$\overline{\phi}$	$[-]$	Time-averaged quantity
$\phi\,'$	$[-]$	Fluctuating quantity
ω	$[1/s]$	Angular velocity
Ω_i	$[1/s]$	Rotational velocity component in i-direction
A	$[m^2]$	Area
$\mathbf{A}$	$[-]$	Surface normal vector
C_D	$[-]$	Drag force coefficient
C_p	$[J/(kg \cdot K)]$	Specific heat capacity
D, D_t	$[m^2/s]$	Diffusion coefficient, Eddy mass diffusivity
e	$[-]$	Coefficient of restitution
E	$[Pa]$	Young's modulus
$\mathbf{F}$	$[N]$	Force vector
f_i	$[N/m^3]$	Net volume force in i-direction
G	$[Pa]$	Shear modulus
I_p	$[kg \cdot m^2]$	Inertia
k	$[F/m]$	Spring stiffness
k	$[W/(m \cdot K)]$	Thermal conductivity
k	$[m^2/s^2]$	Turbulent kinetic energy
m	$[kg]$	Mass
MW	$[g/mol]$	Molecular weight
$\mathbf{M}$	$[N \cdot m]$	Torque
p	$[Pa]$	Pressure
Re_p	$[-]$	Particle Reynolds number
Sc, Sc_t	$[-]$	Schmidt number, Turbulent Schmidt number
t	$[s]$	Time
$u_{Rayleigh}$	$[m/s]$	Rayleigh wave speed
u_i	$[m/s]$	Velocity vector component in i-direction
V_c	$[m/s]$	Particle critical velocity
V_i	$[m/s]$	Particle impact velocity
y	$[-]$	Mole fraction

Abbreviations and Acronyms

CFD	Computational Fluid Dynamics
DEM	Discrete Element Method
DES	Detached Eddy Simulation
DMT	Derjaguin-Muller-Toporov
DNS	Direct Numerical Simulation
DPM	Discrete Particle/Phase/Parcel Method/Model
E-E/TF	Euler-Euler/Two-Fluid Method
FVM	Finite Volume Method
JKR	Johnson-Kendall-Roberts
LES	Large Eddy Simulation
LPT/LPM	Lagrangian Particle Tracking/Method
LWC	Liquid Water Content
RANS	Reynolds-Averaged Navier Stokes
RH	Relative Humidity
SRP	Snow Removing Potential
UDF	User-defined Function
URANS	Unsteady Reynolds-Averaged Navier Stokes

Contents

Abstract i

Preface iii

Acknowledgements iii

Nomenclature v

Contents vii

1 Introduction 3
1.1 Background . . . 3
1.1.1 Snow contamination . . . 3
1.1.2 Previous work . . . 4
1.2 Aim and objective . . . 6
1.2.1 Literature study . . . 6
1.2.2 Simplified simulation method for snow accumulation . . . 6
1.2.3 Testing . . . 7
1.2.4 Multiphase method for snow accumulation . . . 7
1.2.5 Design guidelines . . . 7
1.3 Limitations . . . 7
1.4 Thesis Outline . . . 8

2 Theory 9
2.1 Snow and ice characteristics . . . 9
2.1.1 Snow metamorphism . . . 9
2.1.2 Density . . . 10
2.1.3 Thermal conductivity . . . 10
2.1.4 Specific heat . . . 10
2.1.5 Young's modulus . . . 10
2.1.6 Ice/snow adhesion and friction . . . 11
2.1.7 Angle of repose . . . 12
2.1.8 Particle size and size distribution . . . 12
2.2 Snow contamination on vehicles . . . 13
2.2.1 In-field tests . . . 14
2.2.2 Climatic wind tunnel experiments . . . 15
2.3 Computational Fluid Dynamics . . . 15
2.3.1 Governing equations for a single phase fluid flow . . . 15
2.3.2 Time Averaged Navier-Stokes equations . . . 16
2.3.3 Turbulence modelling . . . 17
2.3.4 Wall shear stress . . . 18
2.4 Multiphase flow . . . 18
2.4.1 Multiphase flow frameworks . . . 18
2.4.2 Discrete Element Method . . . 20
2.4.3 Contact force . . . 22
2.4.4 Rolling resistance . . . 24
2.4.5 Linear cohesion . . . 24
2.4.6 Aerodynamic force . . . 24
2.4.7 Gravity force . . . 25
2.4.8 Time step . . . 25
2.5 Humidity of air . . . 26

3 Method **29**
3.1 Predicting snow accumulation of a complete vehicle . . . 29
3.1.1 Simulation setup . . . 29
3.1.2 Evaluation of aerodynamic properties . . . 31
3.1.3 Simplified multiphase method . . . 32
3.1.4 Additional properties . . . 32
3.1.5 Proposed methods . . . 33
3.1.6 Field functions . . . 33
3.2 Climate chamber experiments . . . 35
3.2.1 Experimental setup . . . 35
3.2.2 Ice-surface friction test . . . 37
3.2.3 Angle of repose test . . . 38
3.2.4 Tests with substitute materials . . . 38
3.3 Postprocessing of experimental results . . . 38
3.4 Multiphase method for snow accumulation . . . 40
3.4.1 Simulation setup . . . 41
3.4.2 Material properties . . . 43
3.4.3 Properties of air . . . 43
3.4.4 Phase coupling . . . 43
3.4.5 Size distribution . . . 43
3.4.6 Tabor number . . . 43
3.4.7 Contact model . . . 44
3.4.8 Rolling resistance coefficient . . . 45

4 Results and discussions **47**
4.1 Snow accumulation based on aerodynamic properties . . . 47
4.1.1 Aerodynamic properties . . . 47
4.1.2 Simple multiphase method . . . 48
4.1.3 Comparison between different methods . . . 48
4.1.4 Discussion . . . 52
4.2 Experiment results . . . 54
4.2.1 Ice-surface friction/adhesion tests . . . 54
4.2.2 Comparison of different materials . . . 56
4.2.3 Effect of adhesion . . . 56
4.2.4 Angle of repose test . . . 57
4.2.5 Substitute Materials for Snow . . . 58
4.2.6 Discussion . . . 60
4.3 Multi-phase method for Snow Accumulation . . . 62
4.3.1 Comparison between standard and custom contact force model . . . 62
4.3.2 Baseline simulation . . . 63
4.3.3 Sensitivity analysis . . . 64
4.3.4 Discussion . . . 65

5 Conclusions **67**
5.1 Discussions . . . 67
5.2 Conclusions . . . 68
5.2.1 Literature study . . . 68
5.2.2 Simplified simulation method for snow accumulation . . . 69
5.2.3 Testing . . . 69
5.2.4 Multiphase simulation method . . . 70
5.3 Future work . . . 70

References **73**

A Appendix 1 **I**

List of Figures

2.1 The angle of repose formed by crushed ice particles on a metal surface. 12
2.2 The morphology diagram of snow crystals as a function of humidity and temperature [45]. . . . 14
2.3 Illustration of self-contamination and third-party contamination. 14
2.4 The difference between a stratified multiphase flow (top) and a dispersed multiphase flow (bottom). In a stratified flow, there is one (or a few) interfaces between the phases, while in a dispersed flow there are multiple interfaces between the dispersed phase (phase 2) and the carrier phase (phase 1). 18
2.5 The analogy between the DEM framework and the mechanical components. The normal force is represented by the parallel arrangement of a slider, spring and dashpot. The tangential force is imitated by the serial arrangement of a slider and a parallel connection of a spring and dashpot. The spring represents the repulsive force; the dashpot replicates viscous damping; the friction slider expresses the friction force. 21
3.1 CAD geometries of the trucks used during the development and validation of the method. . . . 30
3.2 Thermal camera images of the FH truck. Note that the color bar temperature range is different between the images. 33
3.3 Image of the climate chamber and its control panel. 36
3.4 Image of the test rig used for the experiments. 37
3.5 Snapshots of the different tests performed to investigate friction and adhesion. In both cases ice cube samples can be seen on the surface. 38
3.6 Example of angle of repose estimation using different methods. The height of the triangle in the equivalent triangle in the second method is larger, indicating a higher angle of repose compared to the first method. 40
3.7 Domain in the DEM simulation. The cylinder is located in the center. The injection grid is positioned 1 mm below the top surface of the domain. 41
3.8 Section of the generated mesh. In the abscence of air flow in the domain, a base size of 15 mm is deemed as sufficient. Mesh consists of polyhedral elements. 42
3.9 Size distribution of the ice particles. 44
4.1 Line integral convolution (LIC) plots of the velocity components around the simplified truck. Abnormal behavior is noticed in regions with differenly angled surfaces. 47
4.2 Snow accumulation predicted by different methods, plotted at the front of a Volvo FH truck. . 49
4.3 Snow accumulation predicted by different methods, plotted at the door instep of a Volvo FH truck. 49
4.4 Snow accumulation predicted by different methods, plotted at the front mudflap of a Volvo FH truck. 50
4.5 Snow accumulation predicted by different methods, plotted at the rear mudflap of a Volvo FH truck. 50
4.6 Snow accumulation predicted by different methods, plotted at the top of the fuel tank of a Volvo FH truck. 51
4.7 Snow accumulation predicted by different methods, plotted at the top of the wheel cover of a Volvo FH truck. 51
4.8 Snow accumulation predicted by different methods, plotted at the lower side of the chassis of a Volvo FH truck. 52
4.9 Friction/adhesion test results obtained from the static and the continuous rotation tests for two ABS plastic surfaces with different surface quality. 54
4.10 Friction/adhesion test results obtained from the static and the continuous rotation tests for two aluminum surfaces with different surface finish as well as a glass surface. 55
4.11 Snow accumulation predicted by different methods, plotted at the top of the wheel cover of a Volvo FH truck. 56
4.12 Analysis of the adhesion effect, performed for different groupping criteria of the results. 57
4.13 Angle of repose of sbow with respect to fall height. The angle is estimated with two methods: by eye and by calculating the projected area of the pile. 57
4.14 Angle of repose of substitute materials with respect to level of wetness. 59
4.15 Angle of repose of substitute materials with respect to level of wetness. 60

4.16 Comparison of angles of repose for all tested substitute materials. Snow results are included. Note that there is only one level of wetness for every material (0 for all materials except for Material 1 where 1:1 ratio of water to material volume is used). 60
4.17 Comparison between the behaviour of particles in different contact models. Both screenshots are taken at 0.46 seconds of simulation time. 63
4.18 Comparison between the angle of repose obtained from experiments and the result of the DEM baseline simulation. 64
4.19 The sensitivity analysis is performed to investigate the effect of various parameters on the angle of repose of snow at -10°C. 65
A.1 Picture of the test rig used for the friction/adhesion tests. III
A.2 Simple drawing of the test process, including all the relevant forces. IV
A.3 Angle of repose test setup. V
A.4 Different methods of estimating the angle of repose. Visual estimation allows for a quick but possibly biased evaluation while the equivalent method provides a more consistent estimation. . . VII

List of Tables

3.1 Materials used in the ice-surface friction/adhesion experiments. 37
3.2 Materials used in the angle of repose experiments. Both materials used are of cylindrical shape. The dimensions are included in the table. 38
3.3 Materials tested as potential substitutes for snow. A qualitative description is provided. 39
3.4 The properties of materials. 42
3.5 Mass fraction of air and water vapour at different temperatures. Relative Humidity of 95%. . . 43
3.6 The estimations of Tabor number for particle-particle and particle-wall interactions for different effective radii. 44
A.1 Materials used in the ice-surface friction/adhesion experiments. II
A.2 Materials used in the angle of repose experiments. Both materials used where of cylindrical shape. Their dimensions are included in the table. II
A.3 Materials used in the angle of repose experiments. Both materials used where of cylindrical shape. Their dimensions are included in the table. III

1 Introduction

Modern societies rely heavily on commercial vehicles for the transportation of people and goods. As a result, automotive companies are constantly investigating new technologies to enhance safety, drivability, ease of operation and efficiency of commercial vehicles. These include various forms of driver aids such as line departure warning systems, emergency braking systems and more. The smooth operation of these systems depends on multiple sensors and cameras, placed on the exterior of the vehicles. A major concern is the surface contamination that occurs while a vehicle is driving under various conditions. The main reason is that it has the potential to affect the performance of sensitive equipment that is located on the external surfaces of the truck.

Surface contamination refers to accumulation of any foreign substance on a vehicle surface [1]. The types of contamination depend on the road and weather conditions and include e.g. water, snow, dust, mud etc. Snow is particularly interesting since it is a complex material and its accumulation on surfaces depends on many factors such as ice particle shape and size, surface properties and surrounding environment conditions [2], [3].

Snow is typically encountered under harsh weather conditions where proper function of driver aids is essential. However, at the same time, snow contamination increases the risk of malfunction of the equipment which operation is mostly needed at such conditions. According to the U.S. Federal Highway Administration [4], 70% of the road network is located in regions where snowfall occurs annually. As a result, 24% of the annual accidents occur on snow or ice-covered roads. Understanding and predicting the ways in which snow contamination occurs can lead to vast improvements in the future vehicles designs. Computational Fluid Dynamics (CFD) has emerged as a valuable virtual development tool that gives engineers the ability to model physical phenomena early in the design phase of a vehicle and provide directions for the design of the final product.

1.1 Background

In [1] it has been marked that any substance can be regarded as a contaminant given certain requirements. The contaminant has been defined there as a substance that does not belong to a considered surface of a vehicle. In addition to that, it deteriorates the vision of the driver [5], affects the aesthetics of a vehicle [6], contributes to the malfunction of the sensors [7], increases the weight (thus the fuel consumption is higher), reduces both the manoeuvrability of the vehicle and pavement friction [4]. It may also damage certain components (such as actuators and valves), cover and block lights and cables (resulting in deteriorated accessibility) and it can cause certain surfaces to become slippery. The contaminants can be divided with respect to the phase in which they are present on the surface of the vehicle (e.g. liquid, solid or a liquid-solid composition) or their origin (natural or man-made) [1]. The natural solid contaminants are e.g. ocean salt, de-icing salt [8], sand, dust or snow in a liquid (supercooled) or solid form, or an ice-water mixture [9]. The examples of the man-made category are the results of combustion of diesel fuels or tyre wear. During a typical operation of a vehicle, the road soiling is usually composed of multiple types of both man-made and natural particles or complex compounds [1]. During winter months, one of the most significant contributors to contamination is snow.

1.1.1 Snow contamination

There are several possible ways for snow contamination to occur. In the division proposed by Gaylard et al. [7] and described more in detail by Eidevåg [3], the distinguished snow contamination scenarios are the contamination due to falling snow, self-contamination and third-party contamination. The following project focuses primarily on the last two types of surface contamination, which are very similar to each other in many aspects. These driving scenarios are exceptionally problematic for a commercial vehicle as there is a high chance of contaminating the sensors and cameras located around the vehicle.

There are several testing methods that are currently used for predicting the snow contamination on ground vehicles. In the automotive industry, the most established ones are the in-field tests, experiments performed in climatic wind tunnels or climate chambers or the usage of substitute materials [7]. All these testing methods are widely used by the automotive companies and some of them are utilized in the following project.

Another way of predicting snow packing on external surfaces of a vehicle is the use of Computational Fluid Dynamics (CFD) tools. This approach is utilized throughout the design phase of a vehicle. CFD simulations are considered a viable option since they are considerably cheaper compared to almost all common testing methods, they allow for evaluating multiple design concepts and they are able to capture more and more complicated physics. In addition to that, the currently available post-processing techniques of CFD simulations allow for evaluating the designs in a more descriptive, in-depth way, placing CFD as a preferable tool in a product development process. On the other hand, a computational time required to perform multiphase CFD simulations is still a significant problem. The simulation time only rises with increasing complexity of the multiphase interactions or if the simulation is unsteady. Moreover, the simulations of multiphase flows are not that well validated, which raises the issue of reliability of similar methods. Regardless, of these shortcomings, as the available computational power and the accuracy of the models are continuously increasing, CFD is expected to gain even more importance in the future and is perceived as an emerging tool for predicting surface contamination of the road vehicles [1].

1.1.2 Previous work

Previous research within the field of snow contamination of vehicles has focused on developing multiphase methods to predict snow accumulation. However, there are also attempts to develop simplified methods that give an adequate estimation of contaminated regions on the car. In [10], Star-CCM+ software was utilized and it was found that using Eulerian-Lagrangian framework with Lagrangian Particle Method (LPM) for modelling the snow particles did not give adequately good results. Therefore, an alternative, simple single phase method was developed in order to get a better prediction. In this method, a ratio between a near-wall aerodynamic force and a friction force preventing the particle from being ripped-off from the considered surface was calculated. Based on its values a snow removing potential (SRP) of the airflow was determined. This approach does not allow for determining snow packing rate, however, it is significantly cheaper and faster than LPM. It was also concluded that the snow removing potential method correlates better with the wind tunnel test results compared to LPM based method. LPM was sufficient for the particles sizes up to 0.2 mm, whereas SRP method predicted the contamination for the whole spectrum of analysed particle sizes.

In [11], the problem of snow ingress into an air intake of an automobile was investigated. The authors pointed out that the particle-wall collisions and the particle shape and size are exceptionally important when it comes to the amount of snow entering an air intake.

An extensive research on how material properties affect the tendency of dry snow particles to adhere to a surface was performed by Eidevåg et al. [12]. Numerical simulations for impacts in normal direction of single ice particle and both small and large agglomerates with different surfaces were performed. The velocity at which ice particles and agglomerates adhere to a surface was investigated. The critical sizes for sliding and rolling for snow particles, namely, the diameters above which the weight of a particle is high enough to prevent it from adhering to a vertical exterior surface were determined. They also pointed out that the energy dissipated upon collision with a wall by an agglomerate differs substantially from that experienced by a single ice particle.

There have been several attempts to expand the current CFD methodology utilized by automotive companies for the problem of snow accumulation. Enmark [13] and Lind [14] investigated a possibility of first creating and then implementing a regime map for snow particles into a CFD model. The combined results of their work allow for predicting the snow build-up around the vehicle at much lower computational cost compared to CFD-DEM approach that is currently infeasible for the analyses of a detailed vehicle.

In his Master Thesis, Lind focused on developing a Discrete Element Method (DEM) model for particle-wall interaction for dry snow in LIGGGHTS [14]. It stands for a basis for the regime map determining whether the particles stick or bounce upon the contact with the surface. The parameters deemed important for the regime map are the particle normal velocity and particle diameter. He indicated that wall shear stress and tangential velocity are also necessary in order to evaluate snow adhesion. It was also pointed out that the way the friction is modelled should be investigated further, as the current one was perceived unrealistic. It applies also to the sliding and rolling friction coefficients. Therefore, it was suggested that either an extensive literature research or experimental studies should be performed in order to determine more reasonable values. This would allow for studying the influence of impact angle for a particle-wall collision.

Enmark focused on the ways to implement the snow adhesion regime map in a commercial CFD software [13]. He investigated the options that were available in Ansys Fluent and decided to utilize User Defined Functions (UDFs). Different UDFs were developed, for example a Discrete Particle Model (DPM) boundary condition dependant on normal and tangential impact velocities, which allows for predicting whether a snow particle will stick or bounce upon collision with the wall. Another one is a post-processing tool that removes the snow if time-averaged wall shear stresses reach a certain threshold. It was observed that the snow build-up pattern from the infield test can be replicated very well with the wall shear stress obtained from either steady-state or transient simulation. He concluded that the regions with low values of wall shear stress are more prone to snow accumulation compared to the regions with high wall shear stress, where the rip-off of snow occurs. It was suggested that further investigation of the effect of wall shear stress on the snow build-up should be undertaken.

In [15], an angle of repose study on non-adhesive sand particles was performed using numerical methods. A modified DEM framework was employed in this project. The adhesive particles were studied in the work of Tanneru [16]. Here, the angle of repose of the ice particles was analysed. The simulations were also performed with the DEM approach. The dependency of the angle of repose on the temperature of ice was investigated. Additionally, several other contact parameters, such as friction coefficients, work of adhesion and visco-elastic damping coefficient were assessed in terms of their influence on the angle of repose. It was found that the angle of repose is influenced at a certain level by both sliding and rolling resistance. It was proposed that higher values of resistance between particles can be beneficial in order to fully match the experimental data used in this work. A usage of different rolling and sliding resistance models to the ones that were utilized was suggested. An extrapolation method for predicting the coefficient of restitution of smaller ice particles was proposed, which is based on the results of the experiments performed by Higa et al. [17]. For experimental tests, an interesting post-processing method was proposed in [18]. In this work, the influence of cohesion and shape on the angle of repose was evaluated and it occurred that the importance of both of these properties was equally high.

Wang et al. [19] investigated snow packing on the bogies of a high-speed train through a coupling of unsteady aerodynamic simulation (Unsteady Reynolds Averaged Navier-Stokes or Detached Eddy Simulation) for the continuous phase with Discrete Phase Model (DPM) used for simulating the discrete phase. In this research, the particle-particle interactions are disregarded. Moreover, the trap condition, namely, the adhesion of snow particles to the relevant surfaces of the bogie without any rebounds was applied. The outcome of the analysis was that URANS coupled with DPM provides satisfying results regarding snow accumulation and is less expensive compared with DES-DPM method.

In the work of Allain et al. [20], the ways of reducing the snow packing on high-speed trains were explored. Here, an Euler-Lagrange approach was selected. The continuous phase was resolved using steady-state RANS equations with a standard $k - \varepsilon$ realizable turbulence model utilizing wall functions. The discrete phase was calculated using DPM with one-way coupling with the continuous phase. A reflection condition at all walls reduces the momentum after impact and ensures that the collisions are not perfectly elastic. Here, the indicator function (dependant on both the relative angle between the normal vector to the surface and the snow particle's path and the so-called local threshold friction velocity of the fluid) representing trapping of snow was replaced with a mathematical formula. This formula takes into account the mass flux of snow that accumulates on the surface. It utilizes the ratio of the number of snow particles that are encountered in a mesh cell at the wall to the mesh cell face area. This accretion rate is then turned into the snow thickness, which gives a continuous function replicating the snow accumulation in each cell. According to the authors, this criterion - dependant on the relative angle of impact - allowed for more realistic representation of snow packing. The developed method was believed to be applicable to more complex geometries (an entire train according to the authors), which makes this approach an interesting alternative for predicting snow packing in industrial applications.

The influence of several physical and computational parameters on predicting the snow drifting by means of CFD simulations has been evaluated in [21]. In this work, the transport of snow over uniformly rough, flat and open terrain was taken into consideration. The snow drifting was computed using an Eulerian approach, since it was considered as computationally inexpensive and appropriate for this application. In the snow phase equation the drift flux of snow was included in order to represent the outcome of the sedimentation of snow due to the gravity with respect to the falling velocity. The simulations were performed using steady-state RANS. One of the analysed parameters was a turbulent Schmidt number and its impact on the results was considered substantial, as slight variations in the value of the turbulent Schmidt number affected the snow concentration noticeably.

1.2 Aim and objective

The aim of the first part of the thesis is to provide Volvo Group Trucks Technology AB with a tool which allows for prediction of snow packing on a complete vehicle and does not contribute to a significant increase in computational cost. In the second part, the aim is to perform ice-surface experiments with a purpose to determine static friction coefficients between ice and numerous surfaces, as well as explore how friction is affected by the adhesion effects. Moreover, the angle of repose experiments were performed in order to evaluate the impact of temperature and surface material on the formation of the angle. The values of static friction coefficients serve as an input data, while the angles of repose form a validation dataset for the third part. The third part of the project is performed with a view to developing a multiphase simulation tool, which allows for predicting the snow accumulation on commercial vehicles in a more detailed way.

The objectives of the project can be obtained by answering the following questions:

1.2.1 Literature study

When does snow accumulate on the vehicle?

- What are the most severe cases for snow accumulation?
- What is the importance of surrounding conditions on this phenomenon (temperature, humidity etc.)?

Where does snow accumulate on the vehicle?

- What is the effect of the surface material on snow accumulation?
- What is the effect of the surface topology on snow accumulation?

How does snow accumulate on the vehicle?

- What are the properties and mechanisms that govern snow adhesion?
- How does the adhesion change with varying types of snow and surrounding air conditions?
- How does size distribution of snow particles affect accumulation?

1.2.2 Simplified simulation method for snow accumulation

How can snow accumulation behaviour be predicted using simplified simulation tools?

- Is it possible to predict the snow packing using only aerodynamic properties?
- If the aerodynamic properties are insufficient, is it then possible to use a simplified multiphase method coupled with aerodynamic properties and other functions in order to evaluate snow accumulation?
- Which of the utilized properties have the most significant impact on snow packing?
- What are the benefits and drawbacks of such a simplified approach?
- Would a more complex multiphase model produce results that could be more useful from a design perspective?

1.2.3 Testing

Which snow/ice properties can be evaluated through the climate chamber test?

- What is the dependence of material and temperature on ice-surface adhesion?

How should a physical snow accumulation test be performed?

- Can the properties of snow be matched by a substitute material?

1.2.4 Multiphase method for snow accumulation

How can snow accumulation be predicted using a more detailed method, i.e. a multiphase flow model?

- What is the most appropriate multiphase framework for modelling snow accumulation?
- What are the relevant forces that should be included in the mathematical model?
- What collisional model can adequately capture the particle-particle and particle-wall interactions (in-build or custom collisional model)?
- What is the level of complexity that is sufficient in order to replicate the behaviour of the snow?

1.2.5 Design guidelines

How can a vehicle be designed so that snow accumulation problems are minimized?

- What is the influence of a surface material and which materials are suggested?
- What would be the optimal locations for the placement of sensors?
- Which properties should be assessed during the design in order to mitigate the negative impact of snow contamination?

1.3 Limitations

Due to the given time frame, the following thesis must be carried out under certain limitations. The major limitations that the project is subjected to are listed below:

- Snow is an interdisciplinary field and depends on several parameters, such as temperature gradient and time. The following simplifications must be introduced:
  - The snow morphing cannot be considered, as it is currently impossible to take this phenomenon into account with the available computational power.
  - Only certain types of snow can be considered for most of the applications (e.g., cold and dry snow for snow smoke simulations).
- Even less computationally demanding simulation method like coupling of external aerodynamic simulation with particle-tracking model can be infeasible for industrial applications. Hence, the developed simulation method should be both of similar computational cost as a single phase aerodynamic simulation and correlate sufficiently well with the test results. It should capture relevant physics well enough, while not being excessively computationally demanding.
- The multiphase DEM simulation of the entire, detailed model of commercial vehicle is beyond the available computational resources. Therefore, the aim is to replicate the test performed in the climate chamber using this simulation framework.
- Snow testing of a truck is complicated and limited to relatively few testing facilities. Therefore, no full-scale snow testing is performed during this project. Instead, field test results are utilized for validation of the simplified snow accumulation method.

- The ice-surface friction and adhesion tests are carried out using simple testing method that is attainable in a climate chamber used in the project. The angle of repose tests are carried out using simplified, small geometries.
- The computational cluster that is utilized during this project is shared within the aerodynamics analysis team at Volvo, therefore the resources are limited.

1.4 Thesis Outline

This thesis consists of 6 chapters. A short description for each one of them is presented below.

Chapter 1 - Introduction: This chapter contains the background as well as the aim and limitations of this thesis.

Chapter 2 - Theory: This chapter describes the theoretical background which is fundamental in order to successfully carry out the project.

Chapter 3 - Method: This chapter contains the methods developed for each part of the project, i.e. the simplified method for prediction of snow accumulation and the multiphase method for modelling of snow accumulation. Additionally the physical test method is described in this section.

Chapter 4 - Results and Discussions: This chapter presents the results obtained from implementation of each method. Additionally, the results are compared to data obtained from physical testing. The important aspects of the methods are discussed, such as the accuracy in reproducing the phenomena that are investigated.

Chapter 5 - Conclusion: The final chapter of the thesis contains a summary of the project along with the most important results and conclusions that have been reached by performing this thesis. In this chapter, the answers for the research questions are provided, along with the proposal for the future work in this topic.

2 Theory

In this chapter, the theory related to snow and ice, as well as the basics of both single and multiphase fluid dynamics are presented. At the beginning, the relevant information regarding the characteristics of snow and ice is introduced. The next section of the theoretical background is devoted to the concepts of fluid dynamics that are applicable to the work performed within the project. Along with the basic concepts of single and multiphase fluid flows, the Computational Fluid Dynamics (CFD) simulation tool is introduced. Firstly, the modelling approach of single phase fluid flow is presented together with the aerodynamic properties that are relevant for prediction of snow accumulation. In the subsection devoted to multiphase flows, a number of modelling frameworks is briefly described and the theory of Discrete Element Modelling (DEM) concept is explained in detail. Lastly, the relevant contact and cohesion models are introduced.

In some parts of the following work, the particles forming the snow pack are treated individually which is necessary with a view to evaluating both their shape and size. In order to maintain consistency, single snow or ice particles are now addressed as ice particles (alternatively ice grains).

2.1 Snow and ice characteristics

Within this section, the material properties and the most important observations related to snow and ice particles are introduced. The concepts such as snow metamorphism and particle size distribution are presented more in detail.

Snow is a sintered, granular material consisting of an ice structure with pore space [22]. Both ice grains and pores define the microstructure of snow. The mechanical and physical (e.g. thermal) properties of snow are tightly connected with the type and state of snow. The snow type is determined by its microstructure along with its density, while some other parameters are necessary in order to evaluate the state of the snow of particular type. These additional parameters are: liquid water content (LWC), impurities, snow hardness and temperature of snow [22].

Both wet and dry snow laying on the ground undergo a process called sintering. During sintering of dry snow, strong inter-granular ice bonds are formed between slowly growing, rounded grains [23]. The process is governed by the thermodynamic need to reduce surface energy [24].

2.1.1 Snow metamorphism

Snow metamorphism stands for the process of transformation of the ground snow over time [25]. It occurs due to the fact that the temperature of snow is most frequently around its melting point [22]. In this process, both shape and size of an ice particle can change. For the snow in general, the structure of the particle is affected by both the melt-freeze cycles and the goal of minimizing the surface free energy [26]. There is a significant difference between dry snow at sub-freezing temperature and the wet snow at the melting point [26]. These types of snow can be treated as two entirely different materials, since the difference can be noticed in terms of the size, shape and the arrangement of crystals. The snow metamorphism phenomenon varies substantially between these two types of snow.

For dry snow specifically, both the imposed temperature gradient and the surface free energy play a role in snow crystal growth. The surface energy of a snow flake is minimised through the alteration of the surface of the snow flake, namely, its surface area is being reduced [27]. This process is much faster in e.g. a snow cover compared to a controlled, isolated environment. Moreover, both crystal growth rate and vapour flux are almost explicitly governed by temperature gradients. Generally, the rounded crystals are formed at relatively low temperature gradients, while higher values of temperature gradients promote the creation of faceted crystals [26].

Another factor that contributes to high complexity in identification of snow crystals is the fact that the morphology of a snow crystal is time dependant and the whole process of forming the snow crystal matters [25]. As explained in [26], the dry snow below its melting temperature can be divided into two main categories: the kinetic growth form and the equilibrium form. The kinetic growth form is applicable to snow crystals subjected to high temperature gradients. It implies fast rate of growth, thus the grain shape is driven not by minimizing the free surface energy over the surface of the snow particle, but by the kinetics of growth. The resultant snow crystals can have multiple shapes and the most common one is hexagonal. When it comes to the equilibrium form, it develops at low temperature gradients, thus implying slow growth rates. The snow crystals in equilibrium form are rounded, as this shape allows for minimizing the integral of surface free energy over the snow particle. According to Colbeck, at very low temperatures a possibility of obtaining a mixture of rounded and faceted grains exists [26]. The temperature gradient that separates these two categories of dry snow metamorphism is dependant on both temperature and density of the snow.

2.1.2 Density

In a porous medium - such as snow - it is a bulk density that is of interest. The bulk density is calculated as the total mass per volume, including both ice (a solid structure) and pore space [22]. The density of different snow types encountered in practice varies considerably. The density either remains constant or increases upon metamorphic transformations [22].

The density of a fresh snow can be estimated using a statistical model derived based on e.g. the experimental results obtained in Swiss Alps [28]. This model is dependant on atmospheric conditions. A quantitative relationship for the snowfall density that allows for a more accurate estimation of this property on the basis of snow type was also proposed [29].

These snow density estimations are applicable if the ice particles and pore space are treated as an entirety. In certain applications, it is favourable if the ice particles are treated individually. In such case, the density of ice particles is several times higher compared to the bulk density of snow [22].

As proposed in [30], the density of the ice particles between $-140°C$ and $0°C$ can be approximated with the following formula:

$$\rho_{ice} = 917\left(1 - 1.17 * 10^{-4}\theta\right) \tag{2.1}$$

where θ is the temperature in $°C$.

2.1.3 Thermal conductivity

The thermal conductivity of ice was evaluated by Sakazume and Seki [30]. For the temperatures ranging from $-173°C$ to $0°C$ the suggested formula for thermal conductivity looks as follows:

$$k_{ice} = 1.66\left(1.91 - 8.66 * 10^{-3}\theta + 2.97 * 10^{-5}\theta^2\right) \tag{2.2}$$

2.1.4 Specific heat

In [30], the formula for specific heat of ice has been presented. It has been derived based on experimental data gathered for cubic and hexagonal ice. The equation that is applicable for the temperatures between $-183°C$ and $0°C$ is presented below:

$$Cp_{ice} = 0.185 + 0.689 * 10^{-2}\left(\theta + 273.15\right) \tag{2.3}$$

2.1.5 Young's modulus

The dependence of Young's modulus of ice on the temperature was studied by Dantl [31] by measuring the speed of sound in ice at various temperatures. The resultant expression, valid for the range of temperatures between $-140°C$ and the melting point looks as follows:

$$E_{ice} = \frac{100}{10.40\left(1 + 1.070 \cdot 10^{-3}\theta + 1.87 \cdot 10^{-6}\theta^3\right)} \tag{2.4}$$

This formulation was also used by Higa et al. in the work focusing on determining the changes in restitution coefficient of ice particles for various impact velocities and particle radii [17].

2.1.6 Ice/snow adhesion and friction

In this section, the theory behind adhesion and friction of snow and ice is presented.

Adhesion

Faraday [32] discovered that a liquid-like layer exists on ice, which was later confirmed by Jellinek [33]. The properties of this layer change from one side (contact with ice) to the other (contact with air) [33]. The reason that causes the formation of this liquid-like layer is still under debate [34]. For example, Makkonen attributes the formation of the layer to the decrease in equilibrium melting temperature because of excessive amount of pressure [35]. The existence of this layer affects ice adhesion to a surface. It is expected that as temperature decreases, the strength of adhesion of ice increases until the point that the layer disappears [35]. Temperature dependence is explained in [33] and depends on the existence of a liquid-like transition layer that governs adhesion. The existence and thickness of this layer is dependent on the ambient relative humidity and temperature.

An important property that affects snow adhesion is the Liquid Water Content. According to [26], Liquid Water Content is defined as the amount of liquid water that exists in the snow. It can originate from melting, rain or a combination of the two. In [36], it is found that snow exhibits maximum adhesion strength to surfaces when its Liquid Water Content is around 20%.

Another property that has an impact on snow adhesion strength is the surface roughness. In [36], it is shown that surface roughness affects snow adhesion depending on how close to the size of the particles it is. When the surface roughness is similar to the particle size, the contact area is maximized, resulting in maximum adhesion strength. Either lower or higher surface roughness results in reduced contact area and, consequently, lower adhesion strength.

Friction

Friction is an important parameter in snow (or ice) - surface contact as it can lower the threshold of the shear stress that is needed to enable and/or sustain sliding [37]. Additionally, it can affect the heat generation between the surfaces in contact [37]. In [34], the friction is categorized using the thickness of the liquid-like layer as a criterion. Four regimes are defined:

- Dry friction.
- Boundary friction.
- Mixed friction.
- Hydrodynamic friction

Mechanisms that contribute to the creation of the liquid-like layer include [34]:

- Surface melting. The liquid-like layer exists even when there is no contact with a surface [34]. Although this has been experimentally proven, the given explanations vary depending on the experimental method that was used [34].
- Pressure melting. This mechanism contributes to the formation of a liquid-like layer at temperatures close to the melting point of ice [34]. However, since the actual contact area between snow/ice and surface is smaller than the assumed area of contact, the contribution to the formation of the liquid layer is found to be quite small [38].
- Frictional heating. This is considered to be the most important mechanism that affects friction, since the heat generated during sliding causes the snow/ice parts that are in contact with the surface to reach melting point, thus lowering friction [39].

Both static and kinetic friction were studied in [40], where their influence on several winter sports was investigated. It was concluded there that the values of friction coefficients vary considerably e.g. with respect to sliding velocity and temperature.

2.1.7 Angle of repose

The definition of an angle of repose was proposed e.g. in [41], where it is described as one of the most crucial micromeritical properties of snow. It is formed when granular solid particles are injected on the surface of the cylinder (a disk) located underneath the injector (for example a nozzle). As the particles are being dropped, they create a cone which height and diameter increase over time up to the point when the rim of the cone and the cylinder's edge meet [41]. Afterwards, the particles do not accumulate on the pile any more as the excessive particles slide and roll down the slope and the height of the pile remains approximately constant on average. In this way, the angle (called the angle of repose) between the cylinder and the slope is formed [41]. An example of the angle of repose is presented in Figure 2.1.

In the experiments performed by Kuroiwa et al. the angle of repose can take the values from the range of 0 to 90° [41]. It was concluded in [41] that the angle of repose increases with an increase in surface irregularities and particles' adhesion. It was also observed that the diameter of the cylinder does not affect the resultant angle. On the other hand, the fall height seems to affect the results, as the angle is larger for the lower drop height. The temperature dependence was also observed, as the angle rises with increasing temperature. It is connected with an impact of an increased cohesive force of ice at higher temperature on the angle of repose. According to [18], the angle of repose is relatively constant up to approx. -15°C and it is increased almost exponentially when the temperature rises to the values that are closer to the melting point of ice. This research proved also that the angle formed by natural snow crystals is usually much higher compared to the results obtained with pulverized snow. This phenomenon is put down to the surface irregularities that are apparent in natural snow crystals. As observed in [18], shape of the ice particles plays an important role and it should always be considered during the development of models aiming at predicting granular behaviour of various types of snow.

2.1.8 Particle size and size distribution

The size of the ice particles can vary substantially. The grain size can be lower than 0.2 mm or greater than 5 mm [22]. Ice particles encountered in different locations on the road and around the vehicle vary considerably when it comes to the particle size distribution [2]. As mentioned earlier, it is snow smoke (or snow dust) that is the most prone to affect the performance of the vehicle, as it can get sufficiently high from the ground to contaminate e.g. an air intake, sensors, cameras, windshields, etc., while the larger and, as a consequence, heavier particles adhere to the lower sections of the car, e.g. around the insteps, rims, etc.

According to Abrahamsson et al. [2], the suspended snow dust has a particle size distribution close to log-normal. In Langlois et al. [42], a size distribution for each grain type is well represented by a logarithmic kappa (LKAP) distribution. The dataset gathered there covers several types of grains, such as facets, rounds, precipitation particles or depth hoar. The distribution functions have been generated through the image processing of the micro-photographs of snow grains taken with directional LED lighting set at an angle. The digital images of the particles' shadows are then utilized to obtain 3D reconstruction of the ice particles.

Figure 2.1: *The angle of repose formed by crushed ice particles on a metal surface.*

Utilizing the data gathered by Langlois et al., the size distribution of the ice particles can be represented by the following equation formulated in Crowe et al. [43].

$$f(x) = \frac{1}{\sqrt{2\pi}\sigma} \exp\left[-\frac{1}{2}\left(\frac{x-\mu}{\sigma}\right)^2\right] \tag{2.5}$$

where μ represents the mean diameter of the particles and σ is a standard deviation.

2.2 Snow contamination on vehicles

According to [3], the snow particle-wall impact velocity regime has a crucial effect on whether the material is susceptible to snow packing or not. Moreover, the material that is resistant to snow accumulation can be prone to this phenomenon in different impact velocity regime. It is caused by the different dependency of energy loss on the effective Young's modulus (E^*) for the two distinct regimes. In the adhesive-elastic regime (where the impact velocities are lower) the energy loss is inversely proportional to E^*, while in the collisional melting spectrum (where higher impact velocities occur) the energy loss is proportional to E^*. It implies that a material featuring low E^* should have lower tendency for snow accumulation at e.g. the front of the truck or in any other region where high particle-wall impingement velocities are anticipated. On the other hand, materials with high E^* are likely to have less snow in the regions where the impact velocities are low. As discussed in [2], snow smoke consists mostly of small particles of spherical shape (with diameters not exceeding 0.2 mm). It is formed in a cold and dry environment. These small particles are able to follow the airflow due to relatively low Stokes number. According to [10], small and dry snow particles have less tendency to adhere to each other compared to wet snow because of their low Liquid Water Content (LWC). In 2.1.8 it is mentioned that particles at higher temperature have a higher tendency to stick to a surface, which was observed in [2].

As mentioned before, there are three most common ways for snow contamination to occur on external surfaces of vehicles [7], [3]:

- primary contamination
- self-contamination
- third-party contamination

The first type of contamination is considered as the most complicated to model. First of all, the intensity of snowfall can vary substantially [3]. Moreover, there is a great spectrum of snowflakes' shapes. In [22], it was pointed out that the snowflake is an interlinked aggregate or bunch of ice crystals. Libbrecht [44] explained that the lifetime of a growing snowflake equals approx. half an hour and during this time the growth conditions can alter repeatedly. Therefore, the shape of a resultant ice crystal may be very complex. The morphological form of the ice crystals depend on both temperature and supersaturation of water vapour [44]. As depicted in Figure 2.2, the growth of snow crystals depends on the humidity and temperature of the air. It is visible there that snow crystals grow fast and into much more complex, stellar shapes when the humidity is considerably higher. If it is less humid, the shapes are much simpler and the growth is slower [45], [44]. Also the influence of temperature on the crystal's form is rather significant. Both self-contamination and third-party contamination are depicted in Figure 2.3. Here, the vehicle at the front experiences self-contamination. Self-contamination originates from the snow grains lifted from the ground by the wheels and transferred by the airflow to the surfaces of the vehicle [1]. In this scenario, the snow is mostly affecting the sides and the rear of the vehicle [3], [1]. The snow particles are generally larger and depose mostly on lower sections of the vehicle [2]. Third-party contamination due to snow takes place in the driving scenarios involving a vehicle (or vehicles) moving in front of the analysed vehicle [1]. The trailing vehicle in Figure 2.3 is susceptible to this type of contamination. In such case, the snow lifted and convected by the wake of the leading vehicle can contaminate almost all surfaces of the subsequent vehicle [3]. In this definition, the third-party contamination originates essentially in the same way as the self-contamination. The only difference is that the snow is lifted from the wheels of another vehicle rather than from its own wheels [46] and there is a difference in the contaminated regions [47]. Here, mostly small, light snow particles are involved [2], [48]. If the temperature gradients are low, the snow particles are mostly of spherical shape [2], [12].

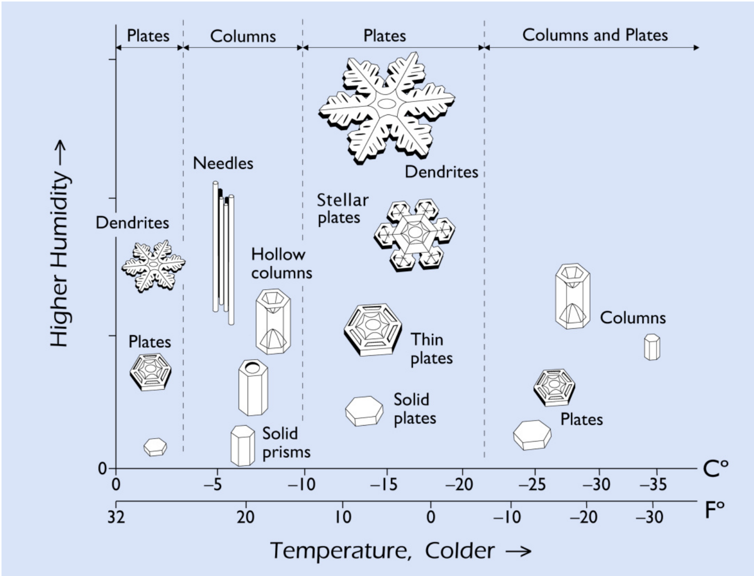

Figure 2.2: *The morphology diagram of snow crystals as a function of humidity and temperature [45].*

There are many tools that allow for predicting snow contamination of road vehicles. According to [7], the snow contamination patterns can be obtained through:

- in-field tests
- climatic wind tunnel experiments
- numerical simulations

In the following section, the details of the in-field tests are presented.

2.2.1 In-field tests

In-field tests have the longest history as an evaluation tool for predicting contamination over vehicle surfaces [1]. This test allows for replicating the snow contamination pattern in an environment that is very close to the

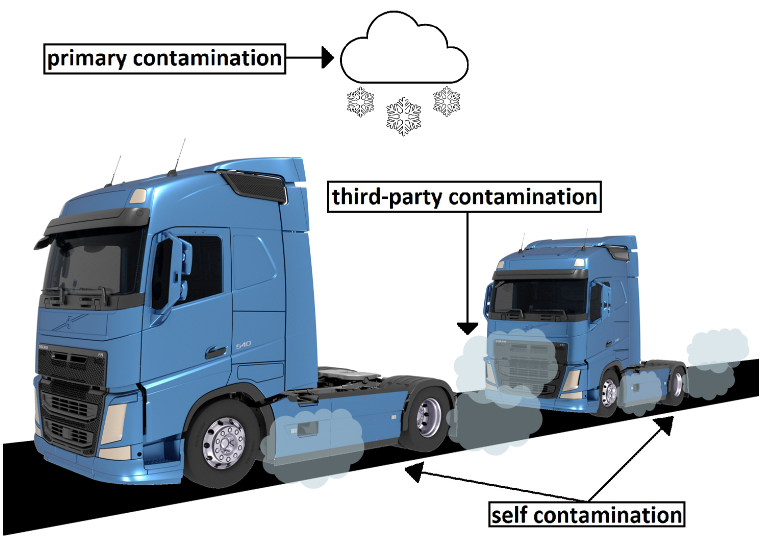

Figure 2.3: *Illustration of self-contamination and third-party contamination.*

real on-road conditions [2]. The limitations of the in-field tests include e.g. uncontrolled environment (amount of snow, temperature, humidity, etc.), a necessity of having working vehicles - which automatically increases the price of such tests, long duration, restricted number of testing tracks and measuring hardships (assessing the deposition of snow is not straightforward) [1].

2.2.2 Climatic wind tunnel experiments

Wind tunnel tests feature higher controllability over the testing procedure [1]. It is possible to perform such tests with vehicles that are not yet drivable or with prototypes, hence climatic wind tunnel testing can be performed before the design of a vehicle is finalized [7]. Moreover, the results of the test can be visualized in a more detailed way [1]. The level of repeatability of experiments is also higher compared to the in-field tests [7]. The climatic wind tunnels are usually considerably smaller than aerodynamic wind tunnels, making them infeasible for snow contamination tests of the truck [1]. In addition to that, smaller test sections affect the aerodynamic results as the test section boundaries are in a close proximity to the vehicle and interfere with the flow field around the analysed vehicle [1].

2.3 Computational Fluid Dynamics

Computational Fluid Dynamics (CFD) is a subfield of fluid dynamics concerned with performing the analyses of systems that involve fluid flow, mass and heat transfer, etc. [49]. Simulations of various contaminants - such as snow - deposing on road vehicles are currently performed using CFD tools [12]. CFD models have been constantly developed in order to capture the surface contamination as much in detail as possible given available computational resources [49]. To predict the behaviour of snow particles in a fluid domain, an external aerodynamic simulation can be coupled with particle-tracking models [50]. In this section, the theory related to a single fluid flow is presented.

The CFD framework that is the most popular and well established for the industrial applications is based on the Finite Volume Method (FVM) [49]. Within this method, the local conservation needs to be preserved. Therefore, solving the equations for local conservation numerically implies that the computational domain needs to be divided into cells [50]. According to the Gauss' theorem, at each cell the governing equations in the partial differential form are rewritten as linear algebraic expressions [49]. This process, so-called discretization, is inherently connected with an introduction of an error to the solution [50]. Nevertheless, it allows for solving the conservation equations with much lower effort. The conservation equations that are solved in here are presented in the next sections.

2.3.1 Governing equations for a single phase fluid flow

The fluid flow is governed by a set of equations which are referred to as Navier-Stokes equations [49]. In this section, these equations, along with the relevant simplifications are introduced. The Navier-Stokes equations consist of the mass conservation equation and the conservation - or, more precisely - the evolution of momentum [49]. These equations in their full form are presented below:

$$\frac{\partial \rho}{\partial t} + \frac{\partial (\rho u_i)}{\partial x_i} = 0 \tag{2.6}$$

$$\frac{\partial u_i}{\partial t} + \frac{\partial u_i u_j}{\partial x_j} = -\frac{1}{\rho}\frac{\partial p}{\partial x_i} + \frac{1}{\rho}\frac{\partial \tau_{ij}}{\partial x_j} + f_i \tag{2.7}$$

where $\tau_{ij} = 2\mu S_{ij} - \frac{2}{3}\mu S_{kk}\delta_{ij}$ is the viscous stress tensor and $S_{kk} = \partial u_k/\partial x_k$. ρ denotes the density of the fluid, u_i - velocity component, P - pressure, f_i - net volume force.

The last equation that could be included into the set of these equations is the energy equation. The mass and momentum conservation equations can be significantly simplified through certain assumptions [51]:

- The analysed fluid flow is incompressible, thus the density of the fluid is constant ($\rho = const.$).
- The gravity effect is disregarded, thus P can be now denoted as a hydrodynamic pressure p.

- The dynamic viscosity can be treated as constant ($\mu = const.$), hence it can be moved outside of the derivative.

- The new form of the mass conservation equation, which now can be referred to as the continuity equation, is now equal to $\frac{\partial u_i}{\partial x_i} = 0$, thus the second term in the viscous stress tensor is zero.

- The net volume forces can be disregarded ($f_i = 0$).

As a result, the Navier-Stokes equations for an incompressible, Newtonian fluid can be represented in the following form:

$$\frac{\partial u_i}{\partial x_i} = 0 \tag{2.8}$$

$$\frac{\partial u_i}{\partial t} + \frac{\partial u_i u_j}{\partial x_j} = -\frac{1}{\rho}\frac{\partial p}{\partial x_i} + \nu \frac{\partial^2 u_i}{\partial x_j \partial x_j} \tag{2.9}$$

where $\nu = \mu/\rho$ is the kinematic viscosity of the fluid. The viscous stress tensor can be now represented as $\tau_{ij} = 2\mu S_{ij} = \mu\left(\frac{\partial u_i}{\partial x_j} + \frac{\partial u_j}{\partial x_i}\right)$.

2.3.2 Time Averaged Navier-Stokes equations

The equations presented in the previous section can be directly solved only in very few cases, namely for the fluid flows characterised by rather small Reynolds numbers, e.g. laminar flows [49]. However, a great majority of flow types encountered in practical applications is turbulent. In most of the applications concerning turbulent flows - including industrial and research - there is no exact solution to these equations derived analytically. In such cases, flows can be determined numerically [49].

There are several ways of solving the Navier-Stokes equations at a cost of introducing certain error into the solution. The approach that allows for solving the Navier-Stokes equations directly, which means that no turbulence is modelled, is called Direct Numerical Simulation (DNS) [50]. This approach remains unattainable for a great majority of engineering problems. The reason for this is the necessity of resolving all turbulent scales directly, which is inherently connected with great computational cost that only grows with increasing Reynolds number [51]. The available computational resources allow mostly for resolving the flows characterised by low Reynolds numbers using DNS [50].

Another approach to the problem of determining the flow field is the range of methods originating from the Large Eddy Simulation (LES) concept. In this method, spatial filtering, instead of time averaging, is used in order to distinguish large and small eddies [49]. The large turbulent scales (hence the name), which have their length scale larger than a certain cut-off limit are resolved, while the scales below this threshold are modelled [51]. This approach has lower computational requirements compared to DNS, while still giving a lot of information about the flow, e.g. the turbulent structures [50]. Nonetheless, it still requires significant computational power which makes it not always the most practical option in the industrial applications [49].

The other possible method requires modelling of the entire flow field, so the turbulent scales are not resolved. Within this scope, the Navier-Stokes equations are averaged in time, which results in a set of so-called Reynolds-averaged Navier-Stokes equations [50]. This approach is very practical if one is primarily concerned about the mean quantities within the flow [51]. RANS is extensively used in a variety of engineering applications and is explained more in detail in the following sections.

RANS method originates from the so-called Reynolds decomposition in which the instantaneous properties of the flow field are decomposed into a time-averaged and fluctuating components [49]. The procedure of splitting instantaneous velocity and pressure components into their mean and fluctuating quantities is depicted below:

$$v_i = \overline{u}_i + {u_i}' \tag{2.10}$$

$$p = \overline{p} + p' \tag{2.11}$$

where Φ denotes an instantaneous quantity, $\overline{\Phi}$ represents a quantity averaged over time and Φ' - a fluctuating component.

The resultant set of time-averaged Navier-Stokes (RANS) equations that are derived under the assumptions presented before looks as follows:

$$\frac{\partial \overline{u}_i}{\partial x_i} = 0 \tag{2.12}$$

$$\frac{\partial \overline{u}_i \overline{u}_j}{\partial x_j} = -\frac{1}{\rho}\frac{\partial \overline{p}}{\partial x_i} + \frac{\partial}{\partial x_j}\left(\nu \frac{\partial \overline{u}_i}{\partial x_j} - \overline{u_i{}'u_j{}'}\right) \tag{2.13}$$

where $\rho\overline{u_i{}'u_j{}'}$ is a Reynolds stress tensor and it constitutes an additional stress term that appears as a result of turbulence. The Reynolds stress tensor depicts the correlation between fluctuating velocity components [51]. The last issue that has to be addressed is the closure problem: for now, the number of equations (four) is lower than the number of unknowns (ten, since the Reynolds stress tensor is symmetric and constitutes of six unknown components, apart from the remaining ones, namely pressure and three components of velocity vector) [51]. For this reason, the Reynolds stress tensor needs to be modelled in order to close the system of equations [49].

2.3.3 Turbulence modelling

In RANS method, the turbulence has to be modelled. Generally, it is possible to find the values of Reynolds stresses through solving their transport equations. However, since this approach is very demanding in terms of computational resources, a more common practice is to model the Reynolds stresses [51]. This is accomplished with the use of an appropriate turbulence model.

This requires solving additional transport equations for quantities that describe the turbulent properties of the flow field. It can be obtained in numerous ways, including for example eddy-viscosity models. Here, the modelled equations for turbulent kinetic energy and dissipation of turbulent kinetic energy are presented [51]. These equations constitute a popular eddy-viscosity model which is called $k - \varepsilon$.

$$\frac{\partial k}{\partial t} + \overline{u}_j\frac{\partial k}{\partial x_j} = \nu_t\left(\frac{\partial \overline{u}_i}{\partial x_j} + \frac{\partial \overline{u}_j}{\partial x_i}\right)\frac{\partial \overline{u}_i}{\partial x_j} + g_i\beta\frac{\nu_t}{\sigma_\theta}\frac{\partial \overline{\theta}}{\partial x_i} - \varepsilon + \frac{\partial}{\partial x_j}\left[\left(\nu + \frac{\nu_t}{\sigma_k}\right)\frac{\partial k}{\partial x_j}\right] \tag{2.14}$$

$$\frac{\partial \varepsilon}{\partial t} + \overline{u}_j\frac{\partial \varepsilon}{\partial x_j} = \frac{\varepsilon}{k}C_{\varepsilon 1}\nu_t\left(\frac{\partial \overline{u}_i}{\partial x_j} + \frac{\partial \overline{u}_j}{\partial x_i}\right)\frac{\partial \overline{u}_i}{\partial x_j} + C_{\varepsilon 1}g_i\frac{\varepsilon}{k}\frac{\nu_t}{\sigma_\theta}\frac{\partial \overline{\theta}}{\partial x_i} - C_{\varepsilon 2}\frac{\varepsilon^2}{k} + \frac{\partial}{\partial x_j}\left[\left(\nu + \frac{\nu_t}{\sigma_\varepsilon}\right)\frac{\partial \varepsilon}{\partial x_j}\right] \tag{2.15}$$

where $C_{\varepsilon 1} = 1.44$, $C_{\varepsilon 2} = 1.92$, $\sigma_k = 1$, $\sigma_\varepsilon = 1.3$. Here, k is the turbulent kinetic energy, ε is the dissipation rate of k and ν_t is a turbulent viscosity.

The way in which these equations are connected with each other is essential. According to Boussinesq assumption [49], to model the Reynolds stresses, the additional property - a turbulent viscosity - is applied [51]. The Boussinesq assumption has been utilized in order to derive the modelled equations for k and ε, hence the turbulent viscosity is apparent there [51]. This additional quantity has to be controlled during the modelling of turbulent fluid flows using eddy-viscosity models. In $k - \epsilon$ model, the turbulent viscosity is derived in the following way:

$$\nu_t = C_\mu\frac{k^2}{\varepsilon} \tag{2.16}$$

where $C_\mu = 0.09$.

Eddy viscosity models showcase certain advantages and disadvantages compared to more comprehensive turbulence models, such as Reynolds Stress Models (RSM) [51], which are suggested for more complex flows [50]. When it comes to the points in favour of eddy viscosity models, $k - \varepsilon$ models are relatively simple due to the usage of isotropic turbulent viscosity. The are also stable and are extensively utilized in a great number of industrial applications [50]. The shortcomings of $k - \varepsilon$ models include, again, the isotropic nature of turbulent viscosity. It is not favourable for e.g. predicting normal stresses accurately, capturing curvature effects or when determining the stagnation flow [51]. In such cases, RSM is preferable as it can account for anisotropy [50]. Moreover, the turbulent viscosity models are not good at predicting the shear stress in the flow regions where adverse pressure gradients occur, as they over-estimates the shear stresses due to insufficient dissipation [51].

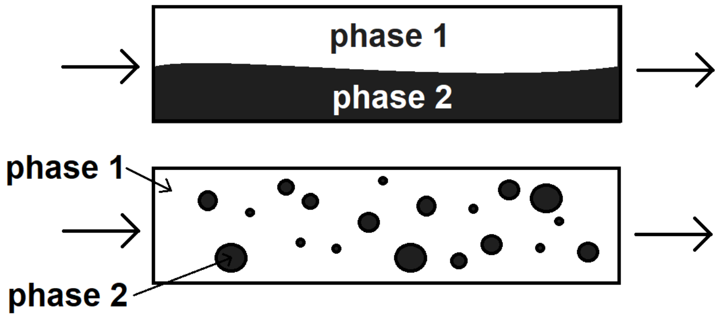

Figure 2.4: *The difference between a stratified multiphase flow (top) and a dispersed multiphase flow (bottom). In a stratified flow, there is one (or a few) interfaces between the phases, while in a dispersed flow there are multiple interfaces between the dispersed phase (phase 2) and the carrier phase (phase 1).*

2.3.4 Wall shear stress

In the vicinity of the wall, the gradient of the velocity is the highest, which is caused by the fact that - at a very short distance - the velocity decreases to zero at the wall [51]. The wall shear stress is given by the following equation:

$$\tau_w = \mu \frac{\partial u_i}{\partial x_j}\bigg|_w \tag{2.17}$$

where u_i is the fluid velocity and x_j is the distance from the wall.

2.4 Multiphase flow

In this section, the theory behind the multiphase flows is presented. The motion of ice particles in the airflow can be treated as a multiphase (gas-solid) flow. In the multiphase flow simulation, the governing equations - valid for each phase in the system - should be satisfied [43]. These equations are, again, the mass conservation and the conservation of momentum. In practical applications, these equations are rewritten under certain assumptions and the resultant formulas are more commonly encountered.

The multiphase flows can be classified in many terms. One of them aims at distinguishing whether the considered phases are dispersed or separated (also called stratified) [50]. The first group represents the flows in which one phase forms a carrier phase, while the other is represented as particles (or entities) with multiple individual interfaces [50]. The stratified flow, on the other hand, is characterised by not many interfaces between the involved phases [50]. The difference between stratified and dispersed fluid flows is depicted in Figure 2.4. In the upper image, the stratified multiphase flow is presented, while the lower one explains the concept of a dispersed flow.

2.4.1 Multiphase flow frameworks

Modelling of particle-laden clouds is currently performed by means of three distinct methods:

- Discrete Element Method (DEM)
- Discrete Parcel Method (DPM)
- Euler-Euler (E-E) or Two-Fluid (TF) Method

The first two modelling approaches are based on Lagrangian frame of reference, while the latter one uses Eulerian framework [43]. In the Lagrangian framework, the particles or parcels are tracked individually within the flow field. This approach is the only one that can treat dilute flows appropriately. In Eulerian modelling, on the other hand, in each node of the field the set of conservation equations (in algebraic form) is solved, hence the changes in the flow field are observed and calculated in each node [43]. It can be used for the analyses of dense flows, where the information passed upon interactions is spread in all directions.

The details of the listed frameworks, along with the examples of the simulations performed with them are presented more in detail in the following section.

Euler-Euler Method

The Two-Fluid Method is based on the assumption that both phases, e.g. fluid and solid are treated as two continua, thus the features of the particles are considered continuous [43]. The solid phase is thereafter treated as a fluid featuring solid properties. This approach is derived from the kinetic theory of gases and a parameter such as a granular temperature is introduced [43]. In general, this framework should be applicable to all types of multiphase flows [50]. However, as mentioned before, it cannot be used for several types of problems that e.g. require differentiation between particles' sizes [43]. Moreover, empirical closure models are required in order to capture all the inter-phase interactions [50].

Discrete Parcel Method

The Lagrangian framework has been employed under several names, such as Lagrangian Particle Tracking, Discrete Particle Method, Discrete Parcel Method, etc. [43]. Despite the smaller or larger differences between these methods, the general idea of treating the carrier phase in Eulerian manner and the dispersed phase with Lagrangian framework is common for all of them. Here, the general description of the Discrete Parcel Method is presented. The DPM approach is based on tracking a representative group of particles. This group (called parcel) consists of many particles of the same dynamic characteristics and is depicted in the form of a single computational particle [43]. This approach can be extended for non-dense or dense applications by incorporating several different phenomena and interactions, such as inter-particle collisions, particle-wall contact, etc. [43]. It can provide very satisfying results in cases when there is not many particles in the analysed system and the collisions are not taken into account [50]. This framework is applicable to different types of multiphase flows that cannot be analysed sufficiently with E-E. If particle-particle interactions are neglected, the computational time here can be feasible for industrial applications. However, the loss of information regarding the inter-particle interactions is also a major drawback of this framework. This loss is caused by introducing parcels into the computation. Since there is no detailed information regarding neither position nor velocity of individual particles, the collisions cannot be traced without e.g. stochastic methods [43], using regime maps created externally [14], etc.

Passive scalar

A passive scalar can represent a diffusive contaminant injected into a flow of a fluid [52]. The most important property of the passive scalar is that it does not have any dynamical effect on the motion of the flow due to its low concentration. The passive scalar is commonly used for the evaluation of dirt deposition on the surfaces [52]. There are two types of passive scalar that can be used [53].

1. In the Lagrangian framework, passive scalar is represented by a cloud of individually advected, massless tracer particles.
2. In the Eulerian framework, passive scalar is represented as an advection-diffusion equation of the continuum concentration field.

The convection - diffusion equation that governs the transport of the passive scalar field in the Eulerian framework can be derived in the following form:

$$\frac{\partial \phi}{\partial t} + u_j \frac{\partial \phi}{\partial x_j} = \kappa \nabla^2 \phi \tag{2.18}$$

where ϕ is the passive scalar field, κ is the diffusivity and u_j is the velocity in the j direction.

A similarity parameter that defines the ratio between the kinematic viscosity of the fluid and the diffusivity of the particles is called Schmidt number [54]. This dimensionless number represents the ratio of a transport of momentum to a transport of mass. It can be treated in an analogy to the Prandtl number, having in mind that the Prandtl number is required for characterising the diffusion of heat, whereas the Schmidt number is used to describe the diffusion of matter:

$$Sc = \frac{\nu}{D} \tag{2.19}$$

where Sc is Schmidt number, ν is a kinematic viscosity of a fluid and D denotes a diffusion coefficient of the fluid.

As stated by Camuffo [55], for low Schmidt numbers particles characterized by a great diffusivity and small size are not significantly affected by the viscosity of the fluid. In cases with moderate turbulence levels, these particles tend to cross the boundary layer and impinge with the surfaces. This behaviour is altered for high Schmidt numbers. In such cases, the particles have rather low diffusivity, they are noticeably larger and the influence of the fluid viscosity on their behaviour cannot be disregarded.

Another parameter that is of interest is the turbulent Schmidt number. It is important in order to correctly predict the mass transfer within the turbulent flow. It is defined as the ratio between the turbulent momentum diffusivity and the turbulent mass diffusivity [56]

$$Sc_t = \frac{\nu_t}{D_t} \tag{2.20}$$

where Sc_t is a turbulent Schmidt number, ν_t is a turbulent viscosity and D_t is an eddy mass diffusivity.

The value of the turbulent Schmidt number is dependant on geometry and different properties of the flow field [56]. The local flow characteristics have considerable impact on the optimal value of this quantity. As observed by Tominaga and Stathopoulos [56], the turbulent Schmidt number value that is optimal for certain application may vary extensively. His study proved that it might range between 0.2 and 1.3, unlike previously suggested spectrum from 0.7 to 0.9. Similar to the analogy between Schmidt and Prandtl number, the turbulent Schmidt number is analogous to the turbulent Prandtl number. Based on the results obtained from multiple Direct Numerical Simulations, it has been proven that the turbulent Schmidt number is a unique function of the molecular Peclet number [54].

Discrete Element Method

In this framework, each particle (called a discrete element) is treated and tracked individually. For this reason, several types of forces, e.g. aerodynamic and contact forces affect their motion [43]. Here, the equations of motion are resolved for all the particles, hence this method is deemed demanding in terms of computational cost. Nevertheless, with a sufficiently large number of DEM particles, this approach allows for a detailed representation of particle flows in which collisions and contacts between particles or particles and walls are frequent. It is extensively used for e.g. granular flow simulations [43].

2.4.2 Discrete Element Method

The motion of ice particles in the air can be considered as a granular flow. The interstitial gas is treated as a continuous phase, while the particles represent a dispersed phase [43]. The snow accumulation on the surface of the vehicle can be treated as a dense particle flow. It means that in this case the continuous contact and collisions are mostly responsible for the motion of the ice particles - unlike in the dilute flow where the fluid forces drive the motion of particles [43]. According to [50], if the spacing between the particles is lower than approx. 10 particle diameters, the flow can be treated as dense.

In dense particle flows the particle response time is greater than the collisional time scale, which represents the time between two consecutive collisions of the particles. The particle response time can be calculated in the following way [50]:

$$\tau_{xp} = \frac{\rho_p d_p^2}{18\mu_f} \tag{2.21}$$

where ρ_p is the particle density, d_p - the particle diameter and μ_f is the dynamic viscosity of the fluid. If the particle concentration is high, particle-particle collisions cannot be disregarded [43]. In such case, particles can interact with each other and lose a certain fraction of their kinetic energy upon collisions. The problem of particle-particle interactions in dense multiphase flows can be treated using two different modelling approaches:

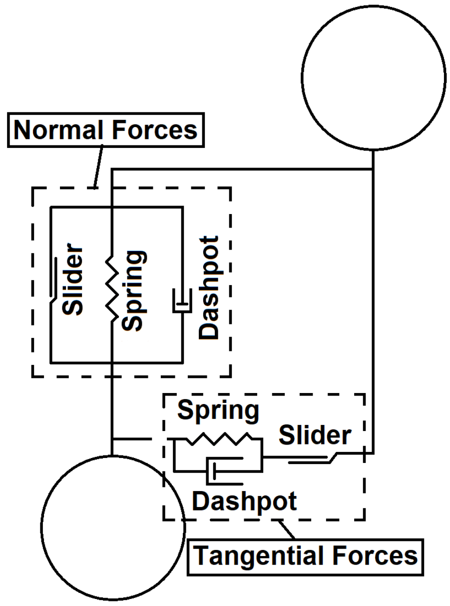

Figure 2.5: *The analogy between the DEM framework and the mechanical components. The normal force is represented by the parallel arrangement of a slider, spring and dashpot. The tangential force is imitated by the serial arrangement of a slider and a parallel connection of a spring and dashpot. The spring represents the repulsive force; the dashpot replicates viscous damping; the friction slider expresses the friction force.*

- Hard-sphere approach
- Soft-sphere approach

The hard-sphere framework is employed for the collision-dominated flows, meaning that the time between the consecutive collisions is significantly larger than the time during which the particles are in contact [43]. In this method the collisions are considered as binary, indicating that any particle collides only with one particle at a time [43]. The soft-sphere approach, commonly referred to as Discrete Element Method (DEM) [43], is utilized for contact-dominated flows. In this case, the continuous contact between particles is prominent and the number of particles that can collide with each other can be noticeably larger [43]. Here, the analogy to the mechanical system consisting of e.g. springs, dash-pots and sliders is used. Both particle-wall and particle-particle collisions can be treated by this model [50]. Although more computationally expensive in comparison to the hard-sphere model, this framework is suggested for granular flows and other flows in which the volume fraction of the dispersed phase exceeds 10% [43]. This framework was used for the simulations of ice particles carried out in [16]. Discrete Element Method was proposed by Cundall and Strack [57]. It is built on certain assumptions. Firstly, it assumes that the particles (considered rigid) can create an overlap between each other without any alterations in their shapes. This overlap represents a deformation between the particles and it is proportional to the repulsive force, which is the result of the contact between the particles [43]. The repulsive force is here replicated with a spring of certain stiffness that is compressed, while the energy loss due to deformation is modelled with e.g. a dashpot, in which the energy is dissipated. Therefore, the velocity after the impingement is lower than before the event. The analogy between the DEM and the mechanical elements is depicted in Figure 2.5.

It is presumed that only the neighbouring particles can affect (or be affected by) the particle of interest which is in direct contact with them [43]. In DEM, the particle trajectories are calculated. All forces acting on the particle are taken into consideration in the Newton's 2^{nd} law of motion, in which the accelerations of the particles are derived. The equations of motion are then integrated numerically with a proper time step in order to obtain positions and orientations [58]. The translational and rotational motion is derived using the two respective equations:

$$m_p \frac{d^2\mathbf{x}_p}{dt^2} = m_p \frac{d\mathbf{u}_p}{dt} = \sum_{k=1}^{N} \mathbf{F}_k \tag{2.22}$$

$$I_p \frac{d\mathbf{\Omega}_p}{dt} = \sum_{k=1}^{N} \mathbf{M}_k \tag{2.23}$$

where m_p is the particle mass, $\mathbf{x}_p$ is the position, $\mathbf{u}_p$ is the velocity, I_p is the inertia, $\mathbf{\Omega}_p$ is the rotational velocity and $\mathbf{F}_k$ represents all the forces and moments acting on a single particle [50].

There are several forces that can act on a particle. A few of them are listed below [50]:

- the drag force
- the pressure gradient force
- the virtual mass force
- the Basset force
- the force due to gravity
- the lift force (Saffman and Magnus forces)
- the contact force

There are more types of forces that can be taken into account, such as the thermophoretic force, the Brownian force, etc. [50]. Note that the contact force originates from collisions and cohesion forces. In the list above, these two types of forces are grouped together as the contact force. In the next sections, the drag force, the force originating from the gravitational effect and the contact force are described more in detail.

2.4.3 Contact force

In order to capture the collisional interactions of the DEM particles accurately, the relevant contact model has to be applied. This can be achieved by utilizing the contact model based on Hertz-Mindlin contact theory. The Hertz-Mindlin model is essentially a non-linear spring-dashpot contact model [59]. The resultant particle-particle or particle-wall contact force is derived in the following way:

$$\mathbf{F_c} = F_n\mathbf{n} + F_t\mathbf{t} \tag{2.24}$$

where F_n and F_t are the magnitudes of the normal and tangential force respectively, while the vectors $\mathbf{n}$ and $\mathbf{t}$ indicate the normal and tangential direction of the respective forces.

The magnitude of the normal force is obtained from the spring-dashpot equation:

$$F_n = -k_n\delta_n - \eta_n u_n \tag{2.25}$$

where k_n represents the normal spring stiffness, δ_n is an overlap in the normal direction at the point of contact, η_n denotes normal damping and u_n is a normal component of the relative velocity between either two particles or a particle and a wall.

The normal spring stiffness k_n is obtained from the formula depicted below:

$$k_n = \frac{4}{3}E^* \left(\delta_n R^*\right)^{\frac{1}{2}} \tag{2.26}$$

E^* and R^* represent the effective Young modulus and the effective radius. These parameters are derived using the following equations:

$$\frac{1}{E^*} = \frac{1-\nu_1^2}{E_1} + \frac{1-\nu_2^2}{E_2} \tag{2.27}$$

$$\frac{1}{R^*} = \frac{1}{R_1} + \frac{1}{R_2} \tag{2.28}$$

where E_i, R_i and ν_i are, respectively, the Young modulus, radius and the Poisson ratio of a particle and $i = 1, 2$ is the index of the colliding particles. If the particle collide with the wall, the radius of the wall is assumed to be infinite. Therefore, the effective radius is then equal to the radius of the particle: $R^* = R_i$.

As mentioned before, the energy dissipation is modelled with a dashpot. The formula for normal damping looks as follows:

$$\eta_n = (5k_n m^*)^{\frac{1}{2}}\, \eta_n^{damp} \tag{2.29}$$

where η_n^{damp} is the damping coefficient in a normal direction and m^* is an equivalent mass. For the particle-particle interaction, the latter one is formulated as:

$$\frac{1}{m^*} = \frac{1}{m_1} + \frac{1}{m_2} \tag{2.30}$$

where m_i is the mass of particle i and $i = 1, 2$. For the particle-wall contact, the mass of the wall is assumed to be infinite, thus the formula simplifies to $m^* = m_i$, where m_i is the mass of the particle.

According to Tsuji et al. [60], the tangential force takes different forms depending on the Coulomb-type law of friction:

$$F_t \leq \mu F_n \tag{2.31}$$

If the tangential force satisfies the formula 2.31, there is no sliding between the particles in contact. In such a case, the magnitude of the tangential force is formulated in a similar way to 2.25:

$$F_t = -k_t \delta_t - \eta_t u_t \tag{2.32}$$

where k_t is the tangential stiffness, δ_t is a tangential overlap at the point of contact, η_t is a tangential damping and u_t is a tangential component of the relative velocity.

If the tangential force is greater than this threshold, the tangential force takes the form of the friction force [43], [60].

$$F_t = -\frac{|F_n| \mu_f \delta_t}{|\delta_t|} \tag{2.33}$$

Therefore, when sliding occurs, the formulation of the tangential component of the contact force from eq. 2.33 replaces the one from eq. 2.32.

The tangential spring stiffness is derived from the equation:

$$k_t = 8G^* \left(\delta_t R^*\right)^{\frac{1}{2}} \tag{2.34}$$

where G^* is the equivalent shear modulus given by the formula:

$$\frac{1}{G^*} = \frac{2\left(2-\nu_1\right)\left(1+\nu_1\right)}{E_1} + \frac{2\left(2-\nu_2\right)\left(1+\nu_2\right)}{E_2} \tag{2.35}$$

The tangential damping is calculated as follows:

$$\eta_t = (5k_t m^*)^{\frac{1}{2}}\, \eta_t^{damp} \tag{2.36}$$

η_t^{damp} is the tangential damping coefficient. The damping coefficients in normal and tangential directions are derived from the below mentioned equations, which form a relationship between the damping coefficient and the coefficient of restitution:

$$\eta_n^{damp} = \frac{-lne_n}{\left(\pi^2 + lne_n{}^2\right)^{\frac{1}{2}}} \tag{2.37}$$

$$\eta_t^{damp} = \frac{-lne_t}{\left(\pi^2 + lne_t{}^2\right)^{\frac{1}{2}}} \tag{2.38}$$

where e_n and e_t are, respectively, the normal and tangential coefficient of restitution. These coefficients are considered as a material property of particles. The coefficient of restitution signifies how much of the impact kinetic energy is lost (dissipated) upon collision. It represents the change in the velocity component (normal or tangential) upon collision by comparing the pre- and post-collisional velocity component. The extensive research on the coefficients of restitution of ice particles impacting various surfaces of the vehicle was done e.g. by Eidevåg et al. [12].

2.4.4 Rolling resistance

The rolling resistance model allows for applying a rolling friction coefficient to the employed contact model. There are several possible rolling resistance models. In Star-CCM+, the available models are: force proportional, constant torque or displacement damping method. The first two are described below. The rolling resistance moment acting on a particle in the force proportional model is defined as follows:

$$\mathbf{M_r} = -\left(\mu_r|\mathbf{F_n}||\mathbf{r_c}|\right)\frac{\omega_p}{|\omega_p|} \tag{2.39}$$

where μ_r is the coefficient of rolling resistance, $\mathbf{r_c}$ is the position vector, which is defined from the centroid of a particle to the contact point and ω_p represents (particle) angular velocity's component that is parallel to the contact plane.

In the constant torque method, the torque that resists rolling of particle is calculated from the equation:

$$M_r = -\frac{\omega_{rel}}{|\omega_{rel}|}\mu_r R_{eq} F_n \tag{2.40}$$

where ω_{rel} is the relative rotation and F_n is the contact force magnitude.

2.4.5 Linear cohesion

According to Crowe et al. [43], inter-particle or particle-wall adhesion results from different types of forces. These forces include, e.g. van der Waals forces or forces from the liquid bridge. The latter one takes place in a humid environment when the surface of the particles is wet. The resultant force is an additive function of two forces: the cohesive force that takes the capillarity effects into account and the force originating from the negative pressure within the liquid bridge [43]. It forms a so-called Laplace-Young equation [43]. The van der Waals forces, on the other hand, originate from the interactions on the molecular level between smooth solid surfaces at contact. Hamaker [61] found the relationship between the magnitude of van der Waals forces acting between two flat surfaces of infinite size and the separation distance between them. The cohesion force, acting between two spherical particles, is expressed by:

$$F_{cohesion} = R_{min}\Gamma\pi F \tag{2.41}$$

where R_{min} represents the minimum radius of the interacting surfaces, Γ is the work of cohesion, and F is a *multiplication model blending factor* [59]. The latter parameter determines whether the cohesion model is Johnson-Kendall-Roberts (JKR) or Derjaguin-Muller-Toporov (DMT). If F takes the value of 1.5, the equation 2.41 represents the JKR model. The JKR model was proposed by Johnson et al. in [62] where the surface energy's effect on the contact between elastic solid surfaces was analysed. However, if this parameter equals 2, DMT model is employed.

The non-dimensional parameter that allows for determining whether JKR or DMT theory should be applied is the Tabor number [63], which is defined by the equation:

$$\mu = \left(\frac{R^*\Gamma^2}{E^{*2}z_0^3}\right)^{1/3} \tag{2.42}$$

where z_0 is the separation distance in the Lennard-Jones potential [63].

2.4.6 Aerodynamic force

The formula for the drag force acting on the particle looks as follows:

$$\mathbf{F_{Drag}} = \frac{1}{2}C_D A_p \rho_{air}|\mathbf{u_{air}} - \mathbf{u_p}|\left(\mathbf{u_{air}} - \mathbf{u_p}\right) \tag{2.43}$$

where A_p is the projected area of a particle, ρ_{air} is the density of air (a continuous phase) and C_D is the drag coefficient of a particle. The velocity difference is a difference between the velocity of air and the velocity of a particle. It constitutes a particle slip velocity $\mathbf{u_s}$, which is equal to $\mathbf{u_s} = \mathbf{u_{air}} - \mathbf{u_p}$.

The particles are assumed to be perfectly spherical. Therefore, the representative (projected) area can be calculated using the following formula:

$$A_p = \pi R_p^2 \tag{2.44}$$

The drag coefficient is represented by the Schiller-Naumann correlation evaluated by Schiller and Naumann [64]. This correlation is suitable for solid particles of spherical shape:

$$C_D = \begin{cases} \frac{24}{Re_p}\left(1 + 0.15 Re_p^{0.687}\right) & Re_p \leq 10^3 \\ 0.44 & Re_p > 10^3 \end{cases} \tag{2.45}$$

where Re_p denotes the particle Reynolds number. It is defined as follows:

$$Re_p = \frac{\rho_p |v_s| D_p}{\mu_{air}} = \frac{\rho_p |v_{air} - v_p| D_p}{\mu_{air}} \tag{2.46}$$

The μ_{air} is the dynamic viscosity of air, which constitutes the continuous phase, and $D_p = 2R_p$ is a diameter of an ice particle.

For the particle Reynolds number lower than 10^3 the drag coefficient decreases with Re_p. According to Crowe et al. [43], the drag coefficient estimated with this correlation deviates by less than 5% from the standard formulation of this parameter. Then, after $Re_p = 10^3$, it stabilizes at the value of 0.44. This spectrum of Re_p numbers is referred to as the inertial range [65], [43].

2.4.7 Gravity force

The gravitational effect is taken into account as a body force. The buoyancy force, which is a result of the density difference between the particle and the fluid, is formulated in the following way [50]:

$$\mathbf{F_{Bouyancy}} = V_p \left(\rho_p - \rho_f\right) \mathbf{g} \tag{2.47}$$

where V_p is the volume of the particle, ρ_p and ρ_f are the densities of the dispersed phase and the carrier phase respectively and $\mathbf{g}$ denotes the constant gravitational acceleration equal to approx. 9.81 m/s^2.

2.4.8 Time step

In the simulations of the DEM particles, it is crucial to ensure that the time step which the calculations are performed with is appropriate. There are three time scales that can be evaluated in order to guarantee that the computations lead to physical results. The first time scale is a Rayleigh wave propagation time, which is defined as follows:

$$\tau_{Rayleigh} = \pi \frac{R}{u_{Rayleigh}} \tag{2.48}$$

where R represents a half of the characteristic minimum dimension of the analysed particle determined for its moment of inertia [59]. If the particles have a spherical shape, the radius of the particle can be considered as a characteristic dimension. $u_{Rayleigh}$ is the Rayleigh wave speed that is dependant on material properties. This speed is obtained as a solution to the secular equation. However, due to an excessive computational cost involved, it is common to utilize approximations of this solution. The classical estimate of the Rayleigh wave speed was presented in the work of Pichugin [66] and looks as follows:

$$u_{Rayleigh} = \frac{0.87 + 1.12\nu}{1 + \nu} \tag{2.49}$$

Another way of deriving this property is to fit an interpolation polynomial at Chebyshev nodes. This results in a more detailed approximation [66]:

$$u_{Rayleigh} = \frac{256}{293} + \nu\left(\frac{60}{307} - \nu\left(\frac{4}{125} + \nu\left(\frac{5}{84} + \nu\frac{4}{237}\right)\right)\right) \tag{2.50}$$

An alternative way of calculating the Rayleigh wave speed was proposed by Thornton [63]:

$$u_{Rayleigh} = \lambda \left(\frac{\rho}{G}\right)^{-0.5} \tag{2.51}$$

where $\lambda = 0.8766 + 0.1631\nu$. This formulation of the Rayleigh wave speed was used in [16]. The maximum time step of the simulation should not exceed a fraction of the Rayleigh wave propagation time. Typically this fraction equals to 10 or 20% of τ_1 [59].

The next time scale associated with the DEM particle is the impact duration time. This limiting criterion can be based on the duration of impact of two perfectly elastic particles. If both of the analysed particles have a spherical shape, according to the Hertz contact theory the impact duration can be derived as follows:

$$\tau_{impact} = 2.94 \left(\frac{5\sqrt{2}\pi\rho}{4} \frac{1-\nu^2}{E} \right)^{\frac{2}{5}} \frac{R}{\sqrt[5]{u_{impact}}} \tag{2.52}$$

The last time scale that should be considered is the particle transit time. This time scale can be derived from the equation below:

$$\tau_{transit} = \frac{R}{u_{particle}} \tag{2.53}$$

where R is equal to the minimum radius of a spherical particle, which constitutes a characteristic dimension of a particle.

In Star-CCM+, the particle time step for the DEM simulations is updated dynamically. This is performed in order to assure that the calculated value of the time step has the lowest value among the three aforementioned ones. The impact duration time step and transit time step cannot be larger than 10% of the above mentioned time scales. The resultant formula for the time step takes the following form:

$$\tau_{final} = \min\left(t_{scale}\tau_{Rayleigh}, 0.1\tau_{impact}, 0.1\tau_{transit}\right) \tag{2.54}$$

2.5 Humidity of air

Relative humidity can have significant effect on snow properties. Therefore, it is important to calculate the amount of water vapor in the air. Commonly, this is done by calculating the mass fractions of water vapor and air respectively [67]. In order to proceed with the calculation, the following properties are needed:

- Molecular Weight of water: $MW_{H_2O} = 18.016$
- Molecular Weight of air: $MW_{air} = 29$
- Relative Humidity (RH)
- Saturation pressure of ice at given temperatures: this can be found in relevant tables [67]. Alternatively, it can be calculated using a formula proposed by Huang [68]:

$$P^*_{H_2O} = \frac{exp(43.494 - \frac{6545.8}{\theta+278})}{(\theta+868)^2} \tag{2.55}$$

  where θ is the temperature in °C.

The partial pressure of water is calculated with the use of the following equation:

$$P_p = RH \cdot P^*_{H_2O} \tag{2.56}$$

Then, the mole fractions of air and water are calculated as follows:

$$y_{H_2O} = \frac{P_p}{P_{atm}} \tag{2.57}$$

$$y_{air} = 1 - y_{H_2O} \tag{2.58}$$

where P_{atm} is the atmospheric pressure in Pa. The next step is to calculate the molecular weight of the mixture:

$$MW_{gas} = y_{air}MW_{air} + y_{H_2O}MW_{H_2O} \tag{2.59}$$

Finally, the mass fractions of air and water are given by the following equations:

$$mf_{air} = y_{air}\frac{MW_{air}}{MW_{gas}} \tag{2.60}$$

$$mf_{H_2O} = y_{air}\frac{MW_{H_2O}}{MW_{gas}} \tag{2.61}$$

3 Method

In this chapter, the methodologies used in this project are presented and analysed. The first part contains the detailed description of the methods used to develop the post-processing tool that predicts snow accumulation on the truck's surface. The usage of either only aerodynamic properties or the combination of these properties with the simple multiphase framework is evaluated. The results obtained using this tool are validated against data gathered during field tests. In the second part, the experimental method followed in order to investigate the effect of adhesion on ice-surface friction is introduced. The experiments are carried out for different materials at various temperatures. Finally, the third part describes the methods used for the development of a multiphase simulation that allows the detailed study of snow accumulation. In this method, more complex phenomena such as particle-particle and particle-wall interactions are taken into account. The CFD software that is utilized throughout the project is Siemens Star-CCM+.

3.1 Predicting snow accumulation of a complete vehicle

The following section contains a description of a proposed method which can be used to evaluate snow packing on a complete commercial vehicle. This method is aiming at predicting the snow contamination pattern, as well as the magnitude of accumulation, over the truck by utilizing results obtained from aerodynamic CFD simulations without the need of employing complex multiphase phenomena. The main idea is to capture the regions of the truck where snow is likely to accumulate.

The development of the method requires evaluation of relevant aerodynamic properties that can adequately approximate snow. The need for added complexity in the form of simplified multiphase method, is also evaluated. Furthermore, other properties, such as temperature, can be used to improve the performance of the method. Selected properties can be combined in user-defined field functions with the aim to obtain a quantitative estimation of the visual patterns and the amount of snow that accumulates on the surfaces of the truck. The process that is followed while developing the proposed method consists of four stages: geometry selection, meshing, performing the simulation and post-processing of the results.

3.1.1 Simulation setup

In this section, the simulation setup consisting of four consecutive steps is described. The preparation of the geometry model is performed using ANSA software, while the remaining steps are carried out in Star-CCM+.

Geometry

The first step is to choose the geometry to be simulated. In this project, two types of geometries are used, simplified and real truck models. The simplified truck represents a 4x2 tractor and a trailer, presented in Figure 3.1(c). The simplified tractor includes door and chassis steps, which are important areas for the investigation. The main reason for using this truck is that it allows to experiment with different post-processing strategies, while keeping the computational cost and memory usage as low as possible. However, it is not possible to validate the obtained results using the simplified model. For this reason, two detailed models of real Volvo trucks, such as the FH, model year 2019, shown in Figure 3.1(a) and FMX, model year 2021, (Figure 3.1(b)), are used for correlation. These trucks have been tested for snow accumulation and the data gathered is utilized in the project.

The strategy followed throughout the project is to run initial simulations of the real FH truck in order to evaluate relevant properties and determine the values for various constants and thresholds used later in custom field functions. This truck model is therefore used for benchmarking of the method. Afterwards, the simplified truck is used with the aim to develop and refine the custom field functions. Finally, the detailed models are utilized in order to evaluate the finalized field functions and compare the results against the in-field test data for both FH and FMX trucks.

(a) Geometry of the FH truck used both for benchmarking and validation of the method.

(b) Geometry of the FMX truck used for validation of the method.

(c) Geometry of the simplified truck used during method development.

Figure 3.1: *CAD geometries of the trucks used during the development and validation of the method.*

Mesh

The meshing procedure for both of the analysed trucks is the same and is conducted using standardized settings. The mesh parameters remain the same for single phase simulations as for the simplified multiphase simulations performed.

Simulation

The simulations are performed using steady-state RANS model with a turbulence model selected for the closure of the RANS equations. The energy equation is not resolved. At the beginning, the detailed truck models are simulated with the same average velocity as during the snow field test. Afterwards, the simulation at a higher speed is performed. The simplified truck is also simulated at these velocities in order to evaluate faster if there is a reasonable tendency in the snow accumulation at the surfaces of the truck.

The calculation of passive scalar is performed for both simplified and detailed truck simulations. Passive scalar is injected from the specified surfaces and its concentration varies depending on the injection surface. The values of Schmidt number and turbulent Schmidt number (which have to be specified) are selected experimentally.

Post-processing

Post-processing is a semi-automatic process. Initially, a standard post-processing tool is used in order to obtain all relevant plots, since it saves significant amount of time. Afterwards, custom field functions and plots are created manually, as it is easier to adjust values when using the software interface. After the post-processing method is finalized, a macro is created which allows the snow accumulation evaluation to be done automatically.

3.1.2 Evaluation of aerodynamic properties

In this section, the aerodynamic properties which are evaluated in order to develop the post-processing tool are described in detail. The choice of relevant properties is based on the observations carried out in Section 2.2. The parameters that are analysed include the wall-shear stress and the velocity components (both normal and tangential).

Wall shear stress

The research in predicting the snow accumulation on the external surfaces of the vehicles proves that the wall-shear stress is considered as an important parameter. As observed in [13], it can be successfully utilized as a rip-off condition for snow. This means that in areas where low wall shear stress values are observed, snow accumulation is expected. On the contrary, in areas with high wall shear stress values snow should be removed. Since this property can be considered as a snow removal potential, it can be evaluated both as a standalone property and as a part of a more complex field function.

Normal velocity component

In [3], it was found that the impact velocity is an important factor in determining if a particle will adhere to a surface or bounce. Since the developed CFD simulation does not contain Lagrangian particles, it is impossible to acquire the impact velocities of the particles that would allow the implementation of a stick-or-bounce criterion. However, assuming that the particles follow the airflow and ignoring the wall effects, the impact velocity could be approximated by the airflow velocity component normal to the truck's surfaces. In such case, it is essential to find an appropriate distance from the surface, where the velocity of a potential snow particle will be assumed equal to the velocity of the airflow.

The normal component of the velocity vector is calculated using the Gram–Schmidt process, which specifies how the set of vectors can be orthonormalised [59]. The velocity component normal to the surface can be obtained with the following equation:

$$\vec{u}_{\perp} = (\vec{u} \cdot \hat{n})\, \hat{n} \tag{3.1}$$

where $\vec{u}_{\perp}$ is the normal velocity component, $\vec{u}$ is a velocity vector and $\hat{n}$ is a unit vector normal to the surface. In order to obtain the surface normal vector in Star-CCM+, the gradient of the wall distance needs to be calculated.

Tangential velocity component

Similarly to the normal velocity component, the tangential velocity component can be used as a criterion to predict if snow particles will stick to a surface or not. In [13], it was implemented as a criterion along with the normal velocity component. Tangential part can show a tendency of the particles to deviate from the truck's surface. The same problems and limitations that are encountered when trying to evaluate the normal velocity component apply also in this case. The tangential velocity component can be obtained by simply subtracting the normal velocity vector from the velocity vector:

$$\vec{u}_{\parallel} = \vec{u} - \vec{u}_{\perp} \tag{3.2}$$

where $\vec{u}_{\parallel}$ represents the tangential component of a velocity vector.

3.1.3 Simplified multiphase method

An alternative method to approximate the particle impingement on the surfaces of the truck is to use a simple multiphase method, for example a passive scalar. The passive scalar is injected into the domain and acts as a snow particle tracer. The usage of this method eliminates the need to evaluate the velocities at certain distances from the truck. In addition to that, the need to motivate the choice of a certain distance is also excluded.

Passive scalar

As discussed in Section 2.4.1, the passive scalar can be used as a tracer in order to indicate potential areas for snow accumulation. A convective - diffusive passive scalar is injected into the domain from the inlet, ground and wheels of the truck. Since the main focus is snow smoke, the amount of passive scalar injected from the inlet is lower than the amount injected from wheels and ground respectively. An investigation of different values of Schmidt and turbulent Schmidt numbers is performed in order to evaluate their effect on the results. The passive scalar cannot be evaluated as a standalone property. It needs to be combined with other properties, such as the wall shear stress and certain axillary quantities, in order to find the amount of passive scalar (imitating snow) that remains on the truck.

3.1.4 Additional properties

Several properties other than aerodynamic were evaluated in order to assess their usefulness for the developed method. These properties include a surface orientation and surface temperature. The description of them is provided in the following sections.

Surface orientation

Surface orientation is used with the aim of replicating the effect of gravity. The idea is that on horizontal surfaces with the surface normal vector pointing upwards the potential for snow accumulation should be higher compared to inclined surfaces. In Star-CCM+, this condition is calculated by dividing the z-component of the surface normal vector by its magnitude:

$$S_{orient} = \frac{A_z}{|\vec{A}|} \tag{3.3}$$

where S_{orient} denotes the surface orientation parameter, A_z is the z-component of the vector normal to the surface and $|\vec{A}|$ is the magnitude of the vector normal to the surface. Note that $\vec{A}$ does not need to be a unit vector. S_{orient} is a scalar parameter that takes the values from the range of -1 and 1.

Temperature data

An additional property that can be evaluated is surface temperature. Surfaces of the truck can be divided into separate categories based on their temperature. The most simple division is to organize them into two groups: ”hot” and ”cold”. The hot surfaces are the ones on which snow melts entirely and, as a result, no accumulation occurs. Since the energy equation is not solved, temperature data has to be acquired in a different way, i.e. through field tests. With the use of an infrared camera, images of the various regions of the FH truck are taken after the truck has completed a predetermined field test. Images showcasing important areas of the truck can be seen in Figure 3.2. The sections that are captured are the front, the side of the tractor, the side of the trailer and the rear of the truck.

After examining the images, the decision is made which parts (or surfaces) of the truck should be considered as hot or cold. It is visible that there are surfaces that have considerably higher temperature compared to the remaining parts, e.g. the wheels' tires, the rims, the axles, the engine, the backside of the cab and certain parts of the chassis. Note that the parts that can be considered as hot are likely to vary depending on the model of the truck. In Star-CCM+, a tag is assigned to the chosen parts, i.e. ”hot” for high temperature parts. This tag is used when creating displayers in scenes. For hot parts, a surface displayer is created, meaning that only the surface is displayed and nothing is plotted on it. For the remaining parts, a scalar displayer is created and a chosen field function is plotted on it.

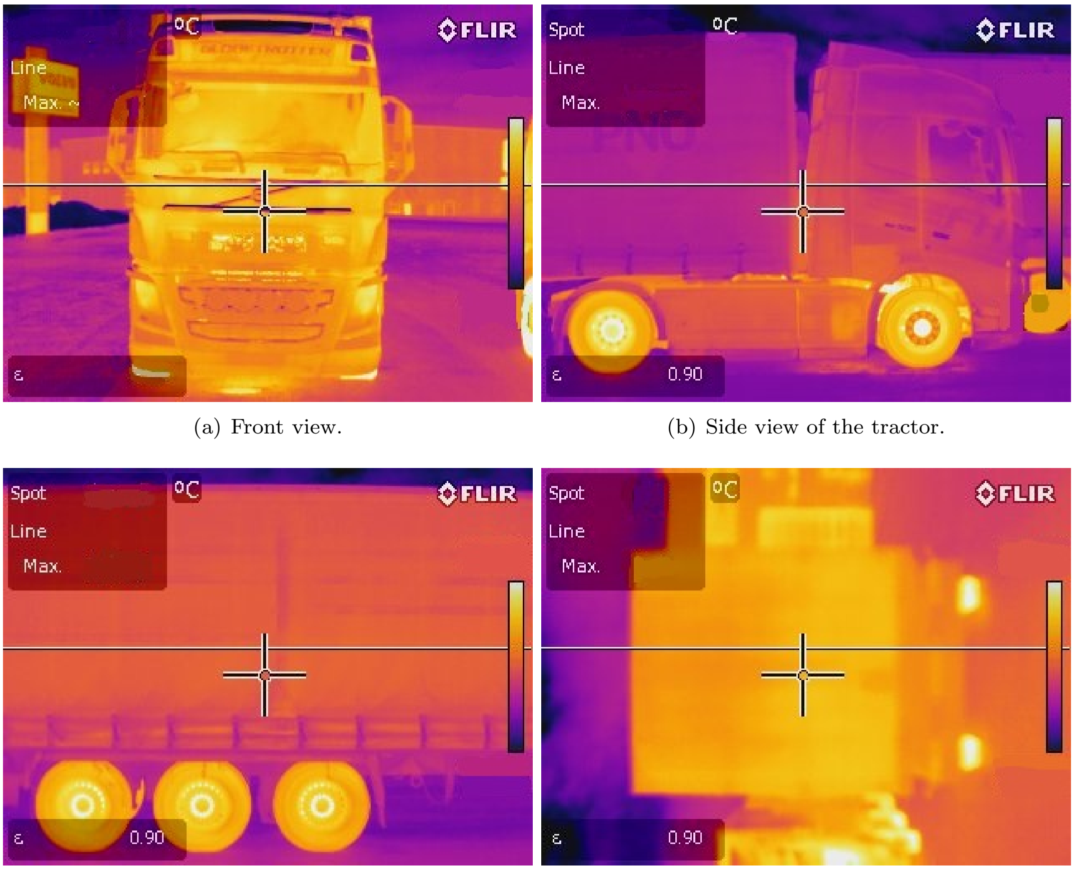

(a) Front view. (b) Side view of the tractor.

(c) Side view of the trailer. (d) Rear view.

Figure 3.2: *Thermal camera images of the FH truck. Note that the color bar temperature range is different between the images.*

3.1.5 Proposed methods

Several approaches to predict snow accumulation of a complete vehicle are investigated during the project:

- At first, the idea of utilizing only wall-shear stress as a tool for predicting the snow accumulation is evaluated. This is the simplest method and does not require the development of a custom field function.
- Next, the idea to use a combination of velocity components (as snow accumulation potential), and wall shear stress (as snow removal potential) is investigated. This method requires the creation of a custom field function.
- Finally, the snow contamination pattern obtained with a custom field function that combines passive scalar and several different properties (aerodynamic and non-aerodynamic) is assessed.

3.1.6 Field functions

After evaluating different properties separately, a user-defined field function combining different properties is created with the intention to depict snow accumulation more accurately. The main approach for the development of the field function is to combine passive scalar, surface orientation, temperature data and wall shear stress. The aim is to develop a function that checks the snow accumulation potential based on the concentration of passive scalar on the surface of the truck and the orientation of the truck surfaces (to account for gravity). The snow removal potential is checked by the wall shear stress and the temperature is taken into account as discussed in the Temperature data segment of Section 3.1.2. The field function is developed through an iterative process: the results obtained with a particular iteration of a function are compared against the available in-field test data; if the outcome is not satisfying, the definition of a function is adjusted and the procedure is repeated;

when the function is perceived to give sufficiently satisfying results, the process is ended.

The following symbols are used in the field functions' definitions:

- s is the symbol used for the passive scalar.
- n is the symbol used for the surface orientation.
- $\mid t_w \mid$ is the symbol used for the magnitude of the wall shear stress.
- a is a coefficient for the passive scalar. Its value can be iterated in order to define the influence of the passive scalar on the function.
- b and c are coefficients for the surface orientation. Their values can be chosen appropriately in order to adjust the effect of the surface orientation on the field function.
- d is a coefficient used to define the influence of the magnitude of wall shear stress on the field function.
- t_1, t_2, t_3 and t_4 are thresholds used in the field functions. Similarly to the coefficients, they can be adjusted in order to achieve better correlation. Note that the threshold values are not the same for all field functions. However, when a certain threshold is used in a field function, its value remains the same throughout the usage of this function.

The first field function is an indicator function, which means that it can only be equal to zero or one. Below a certain limit for the passive scalar no snow accumulation occurs. Above that limit, the presence of snow is determined by the wall shear stress magnitude and the surface orientation. Since this is an indicator function, it can only predict if snow ends up on a surface. It is, however, unable to determine the amount of accumulated snow. The function is presented below in pseudocode form:

```
If (s < t_1)
   udf = 0
else
   if (s >= t_1) and (|t_w| < t_2) and (n > t_3)
      udf = 1
   else
      udf = 0
```

As discussed above, an indicator function is unable to predict the amount of snow accumulation. In order to achieve this, a field function that takes continuous values is developed. The first attempt combines the passive scalar with the surface orientation. A certain value of the wall shear stress magnitude is used as a threshold above which snow is removed entirely from the surface. The pseudocode of this field function looks as follows:

```
If (|t_w| < t_2)
   udf = s + b*(n+c)
else
   udf = 0
```

The aforementioned function has its limitations. It predicts snow accumulation in regions where wall shear stress is below the threshold and for the remaining regions it assumes that snow is removed completely. In this way, the wall shear stress is not considered as an element of a continuous function, but rather as a criterion that enables the continuous function if a certain condition is met. In the next attempt, the wall shear stress is also included in the field function. The function presented below combines the passive scalar, wall shear stress and surface orientation in order to give a more accurate prediction of the amount of snow that accumulates on the truck's surfaces. In this field function, the passive scalar concentration is used as a threshold instead of the wall shear stress magnitude.

```
If (s <= t_1)
   udf = 0
else
   if (a*s + b*(n+c) - d*|t_w| > t_2)
      udf = a*s + b*(n+c) - d*|t_w|
   else
      udf = 0
```

This function tackles the shortcomings of the previous field function. Nevertheless, it still has certain limitations, as it does not take into consideration situations when the wall shear stress is unable to remove snow from the surface. This is likely to occur in the lower sections of the truck where larger - thus heavier - snow particles are packing on the truck's surfaces. A more refined version of the custom field function that addresses this issue is presented below. The main difference compared to the previous field function is the addition of an extra threshold value (t_3), above which the effect of the wall shear stress magnitude is eliminated. This means that above a certain concentration of passive scalar the wall shear stress is not able to remove snow from the surface of the truck.

```
If (s <= t_1)
   udf = 0
else
   if (s >= t_3)
      udf = a*s + b*(n + c)
   else
      if (a*s + b*(n + c) - d*|t_w| > t_2)
         udf = a*s + b*(n + c) - d*|t_w|
      else
         udf = 0
```

This function is the last one that is defined through the iterative process.

3.2 Climate chamber experiments

In this section the methods used to conduct the experimental work in this project are described. More details about the exact procedures and the equipment needed are provided in Appendix A. Three main experiments are performed:

1. An ice-surface friction test with the aim to investigate the effect of temperature and material on the friction coefficient.

2. An ice-surface friction/adhesion test which aims to investigate the effect of adhesion on the friction coefficient.

3. A snow accumulation test with the aim to investigate the effect of temperature on the angle of repose of snow.

Ice-surface adhesion is an important field of investigation, especially for the development of anti-icing surfaces, such as the ones evaluated in [69]. As discussed in [70], there are four methods widely used in research for testing of ice-surface adhesion: Vertical Shear Test, Horizontal Shear Test, Tensile Test and Centrifuge Adhesion Test. In this project, a simpler testing method is evaluated. With this method, the friction coefficient is measured, but the adhesion force is introduced as an additional input alongside material and temperature. Adhesion is evaluated based on the residence time of the ice cubes on the test surface.

3.2.1 Experimental setup

In this section the experimental set up used for the tests is described in detail.

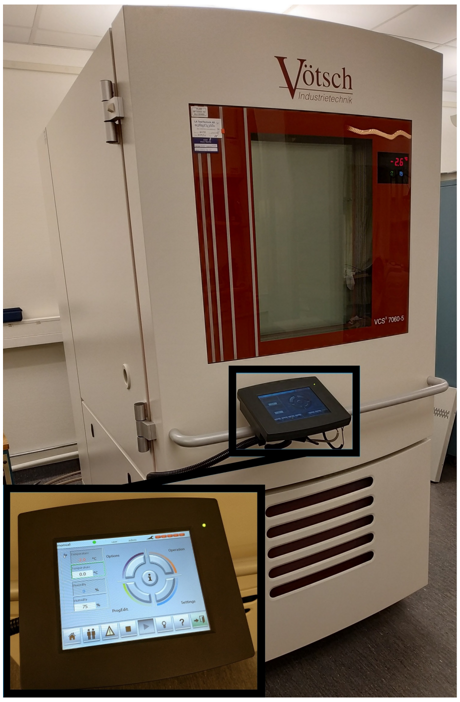

Figure 3.3: *Image of the climate chamber and its control panel.*

Climate chamber

The climate chamber used for the experiments has a test section with dimensions of 0.75 m x 0.75 m x 0.9 m. Temperature is controlled and can be set as low as -60° C. Additionally, relative humidity can be adjusted for temperatures above 0° C. Below 0° C, relative humidity is assumed to be 100%. The test section can be accessed through a side hole, in order to affect the interior conditions as little as possible. There is also a second hole, which is smaller compared to the former one and allows for placement of sensors connected to external equipment. The climate chamber and its control panel are presented in Figure 3.3.

Test rig

The test rig, shown in Figure 3.4, consists of two plates and a hinge that allows the top surface to be tilted. The base plate is made of wood and metal. Metal is used to ensure that the rig has a substantial weight which prevents it from moving. The top plate is smaller in size and features a frame on two of its edges. The frame ensures that the test samples stay in place when positioned on the plate. Additionally, double-sided tape can be used to provide extra security. The angle of the top plate is controlled with a hinge. It can be locked at the desired angle with the use of a bolt. The addition of a protractor to the lower part and a marker on the upper part of the hinge makes the process of changing angle faster and more accurate. Finally, a wrench is attached to the top part of the hinge in order to achieve a smooth rotation of the plate since lower torque is needed.

Materials

A number of materials are tested to investigate the effect of material on ice-surface adhesion and snow accumulation. The materials tested for ice-surface friction/adhesion are presented in Table 3.1. The materials tested for snow accumulations are presented in Table 3.2.

Ice cube creation

Ice cubes are created using silicone molds to facilitate their removal without damaging them. It is essential that all the ice cubes in use are of the same shape and size in order to have repeatability of the tests and directly comparable results. A usage of cubical ice cubes is considered to be more convenient. The dimensions of the ice cubes are 1 cm x 1 cm x 1 cm and their mass is approx. 0.001 kg each.

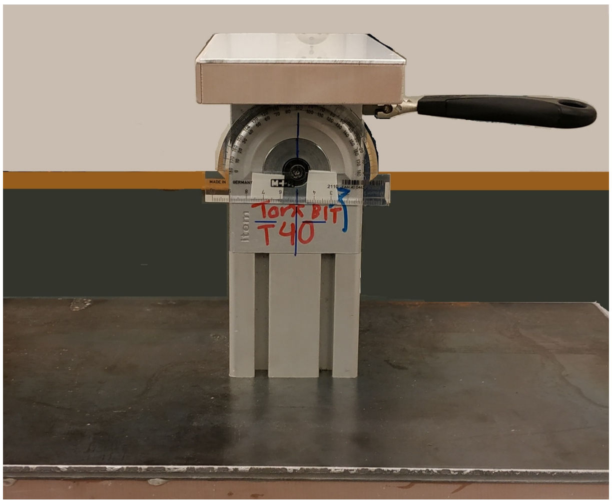

Figure 3.4: *Image of the test rig used for the experiments.*

Material
ABS plastic with smooth surface
ABS plastic with rough surface
Coated aluminum
Non-coated aluminum
Glass

Table 3.1: Materials used in the ice-surface friction/adhesion experiments.

Snow creation

For the snow accumulation experiments, it is always preferable to use natural snow. However, real snow can be difficult to acquire, store and handle. For the experiments conducted during this project, an electric ice shaver is used to replicate snow by shaving ice cubes. The ice cubes are crushed before they are placed inside the ice shaver in order to produce as fine snow as possible. It is essential to create the snow in a low temperature environment in order to prevent it from melting and/or becoming adherent.

3.2.2 Ice-surface friction test

Since adhesion is expected to significantly affect the behaviour of the ice cubes, different tests need to be performed in order to investigate friction and friction/adhesion respectively. The first test aims to investigate the effect of temperature and material on the static friction coefficient. To achieve this, without having to take adhesion into account, the surface is positioned at different angles and an ice cube is placed on it. This process is repeated five times and the behaviour of the ice cubes is recorded, i.e. if they stay on the surface or slide. The angle at which 50% of the ice cubes slide is used to calculate the static friction coefficient at a specific temperature, using equation 3.4. The experiment is repeated at different temperatures (0° C, -10° C, -20° C).

$$\mu = tan\alpha \tag{3.4}$$

Test setup and snapshots of the test are depicted in Figure 3.5. Applying a force in the direction normal to the surface in a controlled manner is very challenging. In order to ensure that the force can be applied in an accurate and repeatable way, the complexity of the experiment setup would have to be increased. Unsuccessful attempts to apply the force by using weights resulted in the investigation of ice-surface adhesion in a different, simpler way. More specifically, a number of ice cubes are placed on the flat surface with a time gap of thirty seconds between each placement. Afterwards, the surface is rotated and the angles at which each ice cube slides are recorded. By analysing the results, the effect of the residence time of the ice cubes on the surface on the friction coefficient can be evaluated.

Material	Diameter, [mm]
Metal	35
Silicone rubber	90

Table 3.2: Materials used in the angle of repose experiments. Both materials used are of cylindrical shape. The dimensions are included in the table.

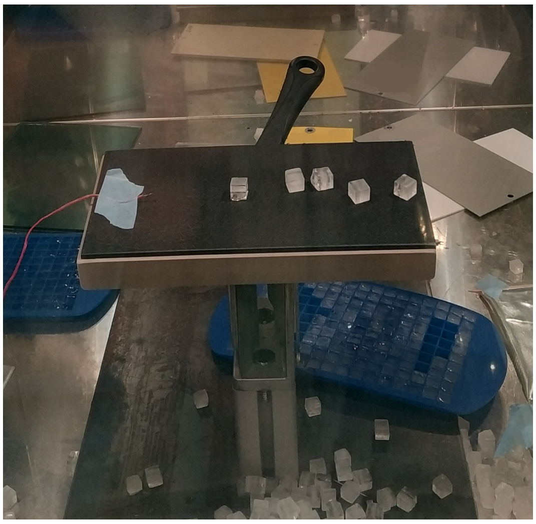

(a) Snapshot of static test on the rough ABS plastic surface. Apart from the ice cubes, the surface temperature sensor can be seen at the left edge of the surface.

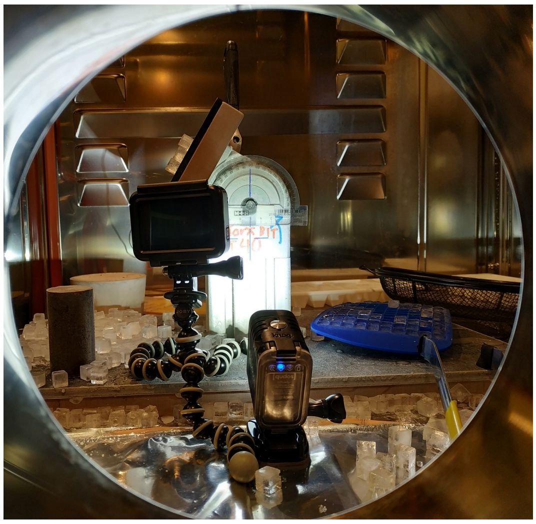

(b) Test setup for the static and rotation tests. A number of adhered ice cubes can be seen on the test surface after the rotation test is completed.

Figure 3.5: *Snapshots of the different tests performed to investigate friction and adhesion. In both cases ice cube samples can be seen on the surface.*

3.2.3 Angle of repose test

The angle of repose experiment is performed to investigate the effect of temperature and material on the angle of repose of the accumulated snow. Results from this test can be used to validate the DEM model results. Snow is created as described in Section 3.2.1. The created snow is placed inside a measuring cup. Measuring the volume and mass of snow gives its density. Snowfall is created by pouring the crushed ice over a grid and then shaking the grid at a specified height above the test surface. The length of snow injection is determined by observing the size and shape of the pile. When it has reached the point where it remains effectively unchanged, the process is stopped.

3.2.4 Tests with substitute materials

There is a possibility of using substitute materials in order to replicate the contamination pattern created by snow. An interesting idea has been described in [19], where the numerical results of the discrete phase were validated through the wind tunnel testing of the two-phase flow. In this test, the snow particles were replaced with saw dust featuring the same density as the snow particles. Saw dust was filtered by means of two separate grids in order to ensure appropriate size range of the particles. This approach stands for a cheaper and less problematic validation method, since it does not require extreme temperatures. In this project, four materials are tested in order to evaluate their potential to be used as substitutes for snow. The materials are presented in Table 3.3 along with a qualitative description.

3.3 Postprocessing of experimental results

This section contains the description of the methods that are used in order to analyze the experiment data. First, the process of analyzing the static test results is presented, followed by the postprocessing method for

Material	Description
Material 1	Superabsorbent polymer
Material 2	Granular material characterized by irregular shaped grains
Material 3	Similar to Material 2 but with grains of larger size/thickness
Material 4	Polymer consisting of soft rounded grains

Table 3.3: Materials tested as potential substitutes for snow. A qualitative description is provided.

the rotation test. Finally, the methods used to estimate the angle of repose are described.

Analysis of static test results

The static test allows the extraction of the following data:

- temperature
- material on which the ice cube is tested
- angle at which the ice cube is tested
- percentage of ice cubes that slide at a particular angle

The main result of the experiment is the percentage of ice cubes that slide at a particular angle. Using this data, the friction coefficient can be estimated. The angle that is used for the calculation is defined as the angle at which 50% of the ice cubes slide. The reasoning behind this decision is that the static friction coefficient is defined by the angle at which the ice cube is about to slide. Therefore, if half of the ice cubes is sliding and the rest remain still this can be a satisfactory approximation.

Analysis of continuous rotation test results

The continuous rotation test allows the extraction of the following data for each ice cube:

- temperature
- surface material on which the ice cube is tested
- residence time of the ice cube on the surface
- angle at which the ice cube slides

In order to analyze the effect of adhesion, the ice cubes can be grouped together using one or more of the available data. Residence time should always be taken into account since this is the parameter that defines adhesion in the proposed method. The following groups are created:

1. Data grouped by residence time. Using this grouping, a general trend for the effect of adhesion can be obtained, regardless of temperature and/or material.

2. Data grouped by residence time and temperature. Using this grouping, a trend for the effect of adhesion at different temperatures can be obtained, while the effect of material is ignored.

3. Data grouped by residence time and material. Using this grouping, a trend for the effect of adhesion for different materials can be established, while the effect of temperature is ignored.

Note that by disregarding certain parameters it is not implied that they have not significant effect on adhesion. By creating groups with the same attributes, an attempt to isolate certain properties and study their effect on adhesion is made. An additional remark is that the sample population is reduced as the number of groupping criteria increases. This makes any conclusions less trustworthy and is the main reason for not groupping data by residence time, temperature and material. Curve fitting methods are used in order to capture trends related to adhesion. The curve that is found to best fit the data is a quadratic polynomial curve.

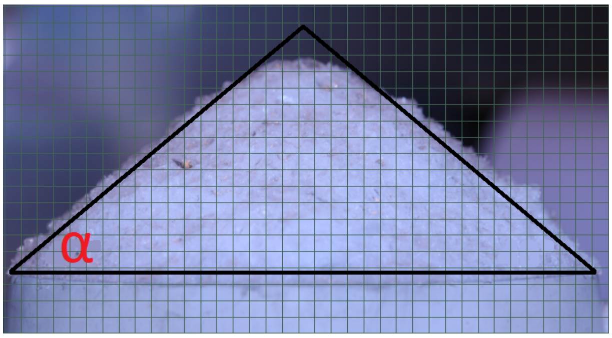

(a) Visual estimation of the angle of repose.

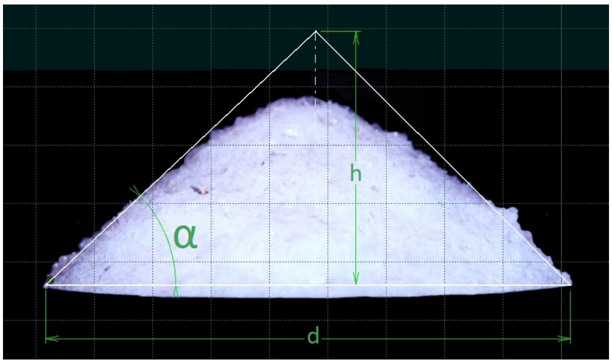

(b) Angle of repose estimation by using the equivalent triangle method.

Figure 3.6: *Example of angle of repose estimation using different methods. The height of the triangle in the equivalent triangle in the second method is larger, indicating a higher angle of repose compared to the first method.*

Methods for estimating the angle of repose

In this section, two methods used to estimate the angle of repose of accumulated snow are described. When performing snow accumulation tests in the climate chamber, both methods are evaluated. Later, in the substitute materials experiments, as well as the DEM simulations, the one considered more consistent is chosen.

Method 1 - Visual estimation

The first method used to estimate the angle of repose is relatively simple. First, the image of the snow pile is analysed to see if there is a need to rotate it in order to ensure that the base of the pile is horizontal. Afterwards, the image is imported into a CAD software. The aim is to enclose the pile in an isosceles triangle that has a base length equal to the base of the snow pack. This method has the advantage of being simple and fairly quick. On the other hand, it can lead to biased estimation of the angle of repose, especially since the snow pile is often non-symmetrical and its top can be flat. As a result, the margin of error for this method is around $\pm 5°$. An example of angle estimation using this method is presented in Figure 3.6(a).

Method 2 - Equivalent triangle method

The second method is used in [18]. The aim is to calculate the projected area of the snow pile and then construct the equivalent isosceles triangle of equal area. The angle of repose can then be obtained. The projected area can be calculated using an image processing software. To simplify the process, the surrounding area of the snow pile should be of different colour with a high contrast to the colour of the pile. Otherwise, the background needs to be removed in order to clearly define the snow pile boundaries. After the area has been calculated, the equivalent isosceles triangle is constructed using CAD software. The margin of error is around $\pm 2°$. The main contributor to the total error is the distortion from the camera. The CAD and image processing software contributions are deemed as very small. The main advantage of this method is that it gives an unbiased and consistent estimation by disregarding potential non-symmetry of the pile. On the other hand, it is more time consuming since it requires additional processing of the image. An example of angle estimation using this method is presented in Figure 3.6(b). Note that this method will never give an angle of repose equal or greater than $90°$ since above this angle a triangle cannot be defined.

3.4 Multiphase method for snow accumulation

The multiphase simulation is created using DEM framework which has been described in 2.4.2. Similar to the simplified method for predicting snow accumulation, the computational software used in this part of the project is Siemens Star-CCM+. The details of the DEM simulation method are presented in the following sections.

3.4.1 Simulation setup

In this section, the details of the domain, geometry, injection of the ice particles, mesh and physics are provided.

Computational domain

The computational domain needs to resemble the experimental test setup explained in 3.2. The climate chamber is replicated with the domain depicted in Figure 3.7. The geometry of the entire domain is a cuboid with a square base 40 mm x 40 mm and a height of 50 mm. The cylinder is located in the centre of the domain and its diameter is equal to 35 mm. The surfaces within the domain have different types of boundaries. All boundaries - apart from the upper surface of the cylinder - have an escape condition, meaning that every particle that passes through such boundary is disregarded and deleted from the simulation. This condition allows for reducing the computational cost of the simulation. On the upper wall of the cylinder, the particle-wall interactions are specified. At a distance of 1 mm from the top of the domain, the particle injection grid is defined.

Injection

The ice particles are injected from an injection grid. The grid has a quadratic shape and consists of 1225 (35 x 35) injection points. In order to introduce a randomness of injection, the randomization of injection is enabled. The randomness level is set to 2.5%. The particles are injected with a certain particle flow rate. In order to replicate the experiment in a more realistic way, the flow rate is specified with a user-defined field function. As a result, the particles are created at a flow rate of 200 particles per second and the injection lasts for 3.5 seconds. After that, during the remaining time of the simulation, the particles either exit the domain or form the pile on the cylinder. In addition to this, the number of particles present in the domain is tracked. Therefore, in case the number of particles does not stabilize throughout the simulation (when the injection is enabled), there is a possibility of prolonging the injection time in order to achieve this state.

Mesh

The computational mesh is created using polyhedral elements. According to the DEM guidelines [59], the mesh cells need to be relatively large in order to avoid the risk of having particles larger than cells. Additionally, since there is no airflow in the domain, there is no real need to refine the quality of the mesh. The base size of the mesh elements is set to 15 mm. The resultant mesh consists of 2340 cells and is presented in Figure 3.8.

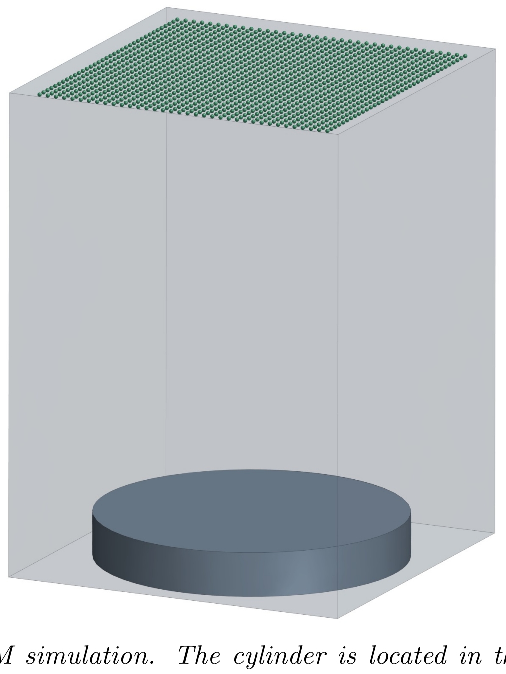

Figure 3.7: *Domain in the DEM simulation. The cylinder is located in the center. The injection grid is positioned 1 mm below the top surface of the domain.*

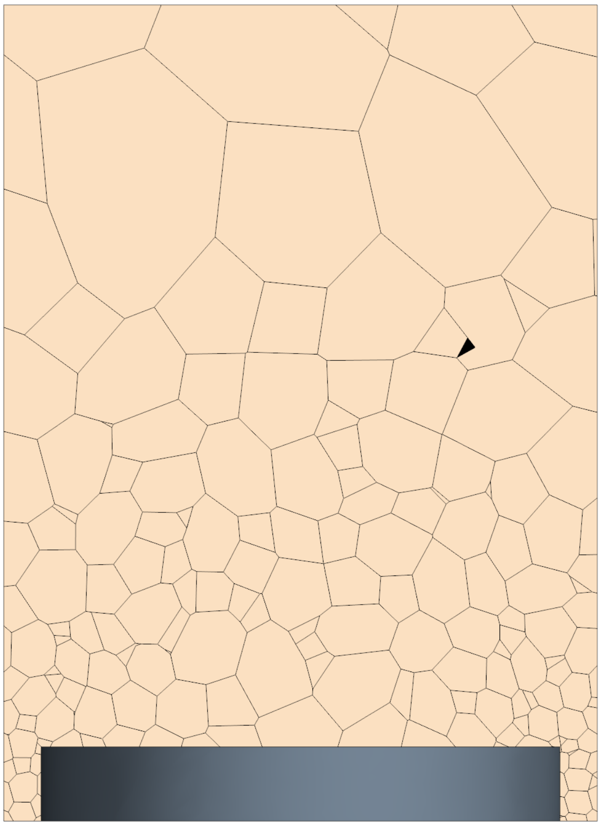

Figure 3.8: *Section of the generated mesh. In the abscence of air flow in the domain, a base size of 15 mm is deemed as sufficient. Mesh consists of polyhedral elements.*

Physics

In Star-CCM+, the dispersed phase is modelled using Lagrangian Particle Tracking option. The particles are specified as DEM particles, which signifies that they have mass, volume and can collide both with each other and with relevant boundaries [59]. The material properties of both ice particles and the upper cylinder wall are specified. Some of the properties of ice particles are different with respect to temperature, which is described more in detail in the following sections. As suggested in [19], the only non-contact forces acting on the DEM particles are the drag force and the gravitational force. The time of the simulation is decided as 4.5 s, which has been proven to be sufficient for most of the analysed cases so that not to see any further changes in a formation of an angle of repose. If this time is not sufficient in order to establish the angle, the simulation can be prolonged based on the particle count monitor, which is described before. The parameters and physical properties that require more thorough explanation are presented in the next sections.

Table 3.4: The properties of materials.

Parameter	Aluminium	Polymer	Ice ($0°C$)	Ice ($-10°C$)	Ice ($-20°C$)
Density $\left[kg/m^3\right]$	2702	2300	917	918.07	919.15
Young's modulus $[GPa]$	68	0.05	9.62	9.74	9.98
Poisson's ratio $[-]$	0.33	0.49	0.31	0.31	0.31
Work of adhesion $\left[J/m^2\right]$	0.117	0.200	0.218	0.218	0.218
$Cp\ [J/(kg \cdot K)]$	-	-	2067	1998	1929
$k\ [W/(m \cdot K)]$	-	-	2.22	2.32	2.43

Table 3.5: Mass fraction of air and water vapour at different temperatures. Relative Humidity of 95%.

Parameter	Ice ($0°C$)	Ice ($-10°C$)	Ice ($-20°C$)
Air [%]	99.85	99.85	99.94
Water vapour [%]	0.15	0.15	0.06

3.4.2 Material properties

The DEM simulation requires the properties of both ice particles and the material of the wall. The properties of the ice particles that depend on the temperature are calculated based on the formulas introduced in Section 2.1. The value of Poisson's ratio for the ice particles is taken as constant and is equal to 0.31 [71]. The values of work of adhesion for ice-ice and ice-aluminium interactions are taken from [12]. The properties of aluminium and polymer are extracted from [59] and [72]. Note that the values of specific heat capacity and thermal conductivity for aluminium and polymer are not necessary for the simulation. All the relevant properties are gathered in the Table 3.4.

In the experiment carried out in the climate chamber, the friction and adhesion of several materials that are encountered in the automotive industry were evaluated. The findings of these experiments serve as an input to the DEM simulation.

3.4.3 Properties of air

Certain properties of air, such as the density or the dynamic viscosity, vary with the temperature. In addition to this, the mass fractions of air and water vapour in the surrounding air vary depending on the relative humidity (RH). In the DEM simulations, it is assumed that the Relative Humidity is equal to 95%. For this value, the mass fractions of air and water vapour at three analysed temperatures are presented in Table 3.5.

3.4.4 Phase coupling

The DEM simulations are carried out without the presence of airflow. Here, the particles are injected with a certain velocity into the stagnant air. One-way coupling between phases is enabled, which means that the carrier phase can affect the motion of the dispersed phase with no reverse effect [43]. Since the mass and size of the ice particles is considered constant throughout the simulation, there is no mass transfer between the phases, which means that the fluid phase can neither add nor subtract mass from the dispersed phase. On the other hand, the momentum coupling is present since the continuous phase affects the ice particles through the aerodynamic forces [43]. Energy coupling is insignificant, since the temperatures of the airflow, the cylinder and the ice particles are the same, hence no energy in the form of heat is transferred between them.

3.4.5 Size distribution

As described in Section 2.2, in the third-party contamination and self-contamination the particles are mostly spheroids. For this reason, these types of contamination are considered as much easier to replicate in the simulations. As mentioned in Section 2.1.8, the size distribution of the spherical particles can be considered log-normal, hence this distribution is used in the DEM simulations. The values gathered in Langlois et al. [42] are selected for specifying the details of this distribution. The mean particle diameter is therefore equal to the equivalent sphere diameter for rounded particles. The maximum particle diameter is restricted to the size of the grid that is used in the experiment carried out in the climate chamber. The smallest diameter is assumed to be 0.01 mm. The standard deviation is set to 1. Using the equation 2.5 with the selected values, the size distribution of the ice particles in the DEM simulation looks as in the Figure 3.9.

3.4.6 Tabor number

In order to ensure that the JKR model (introduced in Section 2.4.5) is appropriate for calculation of inter-particle cohesion and adhesion between the particles and the wall, the Tabor number needs to be estimated. This parameter is calculated from the equation 2.42. For the calculations, the equilibrium separation distance of 0.4 nm is selected. As stated in Crowe et al. [43], this is the smallest separation distance required for obtaining van der Waals force between two plates (in air at standard conditions). The results of the estimations are gathered

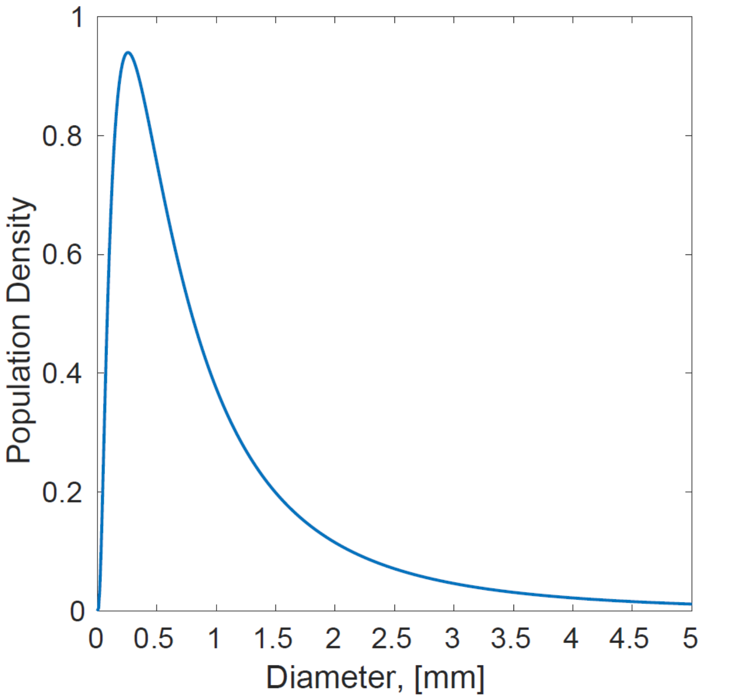

Figure 3.9: *Size distribution of the ice particles.*

Table 3.6: The estimations of Tabor number for particle-particle and particle-wall interactions for different effective radii.

Effective radius	μ (particle-particle)	μ (particle-wall)
R^*_{min}	4.01	2.29
R^*_{avg}	16.53	9.46
R^*_{max}	31.83	18.21

in Table 3.6.

In the Table 3.6, R^*_{min}, R^*_{avg} and R^*_{max} denote the values of the effective radius calculated from the eq. 2.28 for the particles of different size. Therefore, for the calculation of Tabor number for particle-particle interactions, R^*_{min} denotes the effective radius of the two smallest particles interacting with each other, R^*_{avg} - two particles of the average size and R^*_{max} - two largest particles. For the particle-wall interactions, the effective radius is equal to the radius of the particle (as the radius of the wall is assumed to be infinite). It is hence visible that the Tabor number for the interaction between similar particles and such particles and the wall takes different values. According to Thornton [63], the JKR model should be employed if the Tabor number is larger than 5, while the DMT model is suggested when the Tabor number is lower than 0.1. From the Table 3.6 it is clear that the Tabor number lies between 2.29 and 31.83 and the majority of contacts occurs in the spectrum of Tabor numbers larger than 5. For this reason, the choice of JKR model is justified.

3.4.7 Contact model

As stated in Section 2.4.3, Hertz-Mindlin is selected to model the contact. In Star-CCM+, this model is available among the default contact models [59]. The parameters that have to be specified along with this model are:

- normal coefficient of restitution
- tangential coefficient of restitution
- coefficient of rolling resistance

It was mentioned before that the coefficient of restitution allows for assessing the loss of kinetic energy upon collision, either between particles or between a particle and a wall. However, the default Hertz-Mindlin model does not allow for a coefficient of restitution that may vary in space. Therefore, in the default model, the coefficients of restitution have to be constant and have equal values for all the impinging particles. This is a significant simplification of the real behaviour of ice particles. For this reason, the implementation of user-defined contact model is also evaluated. The user-defined contact model is, again, the Hertz-Mindlin model. In the model implemented in such a way there is a possibility of utilizing the variable coefficients of restitution. However, it has to be noted that such model is not as optimised as the default model [59]. As a result, the computations take much longer time compared with the usage of an in-build Hertz-Mindlin model.

Normal coefficient of restitution

The custom model is based on the equations presented in Section 2.4.3. It is recreated in the same way as a default model in Star-CCM+. The only difference is the formulation of the normal coefficient of restitution. At the beginning, the usage of the coefficient of restitution for normal impacts suggested by Eidevåg et al. is evaluated [12]. This formulation is suggested for the quasi-elastic regime of the ice-surface collisions:

$$e_n = \begin{cases} 0 & V_i \leq V_c \\ \left(1 - \left(\frac{V_c}{V_i}\right)^2\right)^{1/2} & V_i > V_c \end{cases} \tag{3.5}$$

where V_i is the impact velocity and V_c is the critical velocity. As described in [63], V_c is the impact velocity below which the particle sticks to the surface. For this reason, if V_i is lower than or equal to V_c, the coefficient of restitution is equal to 0, meaning that the whole impact kinetic energy is dissipated. If V_i exceeds the value of V_c, the bouncing occurs. It is, however, hard to implement this formulation in Star-CCM+ due to its complexity and the fact that the evaluation of V_i and V_c for particle-particle collisions is not straightforward in the software.

Therefore, an alternative approach, successfully implemented by [16] is explored. The author extrapolated the results of the experiments performed by Higa et al. [17] on the smaller ice particles (for the quasi-elastic regime). The resultant extrapolation curve is described by the following formula:

$$e_n = 0.0744 \log\left(\frac{R^*}{10}\right) + 0.8611 \tag{3.6}$$

This formulation for the normal coefficient of restitution is used in the following project in order to compare the results between the simulation where e_n is constant and formulated as in 3.6.

Tangential coefficient of restitution

The formulation of the tangential coefficient of restitution for ice is not straightforward [3]. Therefore, the sensitivity analysis of this coefficient is performed. The angles of repose for different values of e_t for particle-particle and particle-wall interactions are analysed.

Sliding friction coefficient

The sliding friction coefficient is needed in order to fully describe the Hertz-Mindlin contact model in Star-CCM+. As mentioned before, the values of this coefficient for ice-surface interactions are taken from the experiments described in 3.2. As observed in [73], the expected values of ice-ice friction coefficient vary from approx. 0.01 to ca. 0.1.

3.4.8 Rolling resistance coefficient

The rolling resistance is an optional model that can be enabled in Star-CCM+ for phase interactions. When selected together with the Hertz-Mindlin contact model, this model applies a rolling friction coefficient (μ_r) to the contact model [59]. In Star-CCM+, there are three rolling resistance models that can be selected: constant torque, force proportional and displacement damping. The impact of the first two of these methods on the angle of repose is evaluated in this work.

4 Results and discussions

In this chapter, the results of the performed work are presented and discussed. At the beginning, the outcome of the CFD simulations aiming at predicting the snow pattern over the entire vehicle is shown. In the subsequent sections, the results obtained from the experiments are depicted. These findings are divided into the results gathered in the climate chamber experiments and the outcome of the tests with substitute materials. Finally, the findings from the multiphase simulation performed using DEM framework are presented. Each of the aforementioned parts is followed by a section, in which the results are discussed.

4.1 Snow accumulation based on aerodynamic properties

In this section, the results of the simple post-processing tool utilized for predicting snow accumulation on the surface of the truck are presented. First, the outcome of utilizing only aerodynamic properties, such as wall shear stress and velocity components is shown. Then, the results obtained with the simplified multiphase method are presented and compared against wall shear stress data.

4.1.1 Aerodynamic properties

This section contains results from the evaluation of relevant aerodynamic properties.

Velocity components

Line integral convolution (LIC) plot of the velocity component that is normal to the simplified truck's surfaces, is presented in Figure 4.1(a). Close to the surface the velocity component is very small. Additionally, in some regions where differente surfaces are located in close proximity, the software attempts to satisfy the normal velocity criterion for every surface simultaneously. The tangential velocity component, shown in Figure 4.1(b), behaves in a similar way.

Wall shear stress

Wall Shear Stress is evaluated in two ways:

- As a property representing the snow removing potential. Low wall shear stress values indicate that snow is not removed from a surface. Large wall shear stress values indicate that snow is removed entirely from a surface. Therefore, wall shear stress can be used as a rip-off condition for snow.

(a) Velocity component in the direction which is normal to the surfaces of the truck.

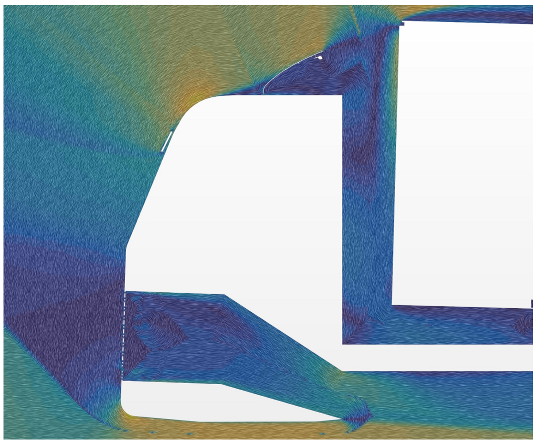

(b) Velocity component in the direction which is tangential to the surfaces of the truck

Figure 4.1: *Line integral convolution (LIC) plots of the velocity components around the simplified truck. Abnormal behavior is noticed in regions with differenly angled surfaces.*

- As a standalone method for snow accumulation. In this case, the result is interpreted directly in terms of snow accumulation.

In the current study, it can be observed that the higher the value of the wall shear-stresses on the surface, the lower the chance of snow accumulation. Results from evaluating this property are presented in Section 4.1.3 in order to allow for a comparison between this method and the simple multiphase method. Note that the wall shear stress is normalized with a value chosen after benchmarking against test data.

4.1.2 Simple multiphase method

In the following section, results obtained from implementation of the proposed method for predicting snow accumulation are presented. As mentioned before, the method consists mainly of a combination of convective-diffusive tracer (which is the passive scalar) and aerodynamic properties (in the form of wall shear stress). The final result is refined by including temperature data and the effect of gravity, represented by using the surface orientation. The results presented in this section are obtained using the final field function, referred to as UDF4. It has to be noted that the results are normalized with the maximum value reached by the created field function. To make it easier for the reader to understand the results the colorbar can be interpreted as follows:

- Dark grey represents the non-contaminated regions of the truck.
- Dark blue indicates little to no accumulation.
- Light blue indicates moderate amount of snow packing.
- White indicates maximum amount of snow packing.

Note that this is a qualitative description as it is quite hard to distinguish between different levels of contamination in some cases.

4.1.3 Comparison between different methods

The following section contains a comparison between results obtained by utilizing different methods, more specifically the simple wall shear stress method and the final proposed user defined function (called UDF4 from now on). While the two methods are normalized with different values, the same colour bar applies to both of them, as the results of both methods are qualitative.

Front of the truck

The wall shear stress, plotted on the surface of the truck, is presented in Figure 4.2(a). Observation of the plot shows lower values of wall shear stress at the center of the truck (around the stagnation region). This indicates a potential for snow accumulation in these regions. While the general pattern correlates fairly well with experimental data, the predicted amount of snow is much higher than expected, especially in the area between the emblem and the grille. Other regions where the results do not agree with experimental data include the grab handles, which are situated below the windscreen. Only the outer corner of the cavity is covered with snow, although a more uniform distribution is expected in that case. Figure 4.2(b) shows the predicted snow accumulation at the front of the truck, obtained using UDF4. The snow contamination pattern correlates well with experimental data. Furthermore, the amount of snow packing is lower compared to what the wall shear stress method predicts (Figure 4.2(a)), which agrees with the field test results. The improved capabilities of the proposed method are showcased by checking the grab handle cavity. Observation shows a more uniform distribution of snow on the entire cavity surface in contrast to the result obtained from the wall shear stress method.

Instep

The instep is a crucial region, since it allows the driver to access the truck. Results obtained from the wall shear stress method for the door instep are presented in Figure 4.3(a). It is observed that the wall shear stress values are lower at the edges and the vertical surfaces of the step, while the main surface of the step is dominated by high wall shear stress. This indicates that there is less snow accumulated on the main step and a lot of snow at the edges and vertical surfaces. This result does not agree well with the field test data. Predicted snow

(a) Wall Shear Stress

(b) UDF4

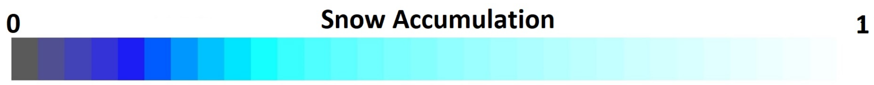

Figure 4.2: *Snow accumulation predicted by different methods, plotted at the front of a Volvo FH truck.*

accumulation given by UDF4 at the door instep region, presented in Figure 4.3(b), shows a mostly uniform distribution of snow on the main step area. Additionally, smaller amount of snow packing is predicted for the vertical surfaces. These results are largely in agreement with results obtained from in-field tests. Comparison with the wall shear stress results, shows the improved performance of the proposed method both on the main step surface and on the vertical surfaces around it.

Mudflaps

Other regions include the undersides of the mudflaps. Apart from snow smoke, these areas are exposed to heavier and wetter snow which tends to be stickier. Therefore, it is interesting to check if the different type of snow can be captured by evaluating the wall shear stress values. Figure 4.4(a) shows the lower part of the

(a) Wall Shear Stress

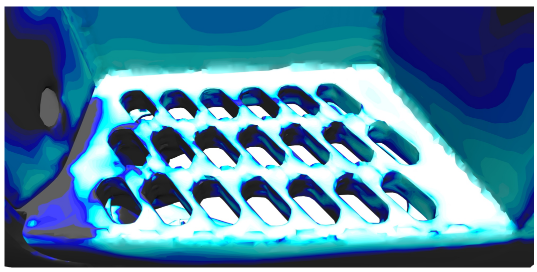

(b) UDF4

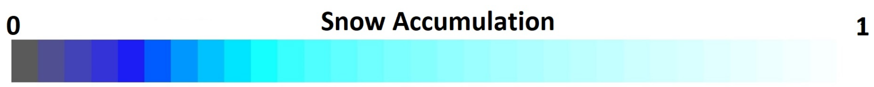

Figure 4.3: *Snow accumulation predicted by different methods, plotted at the door instep of a Volvo FH truck.*

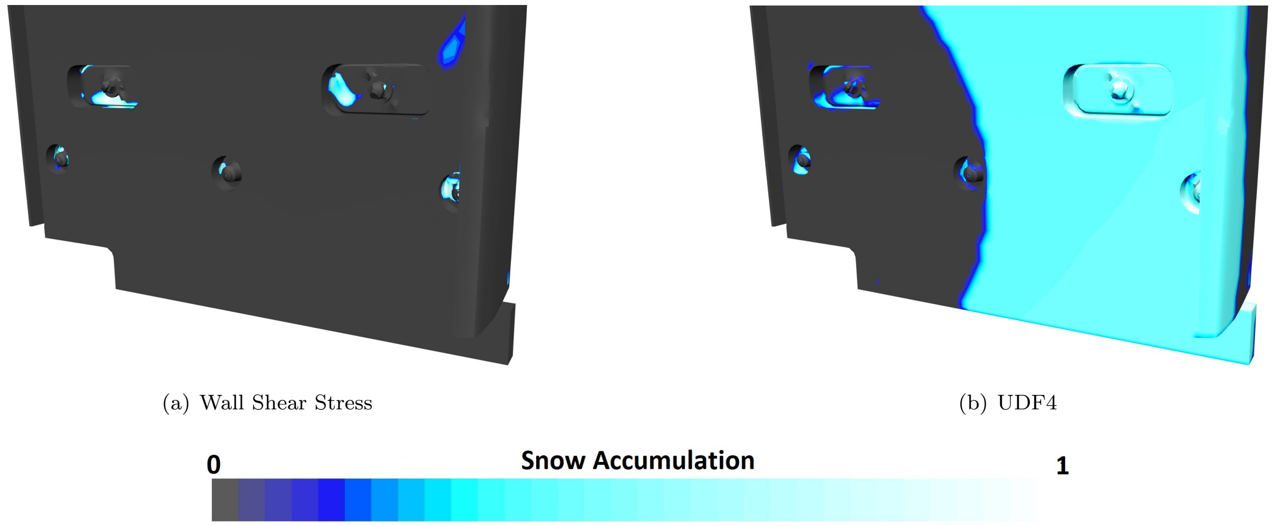

Figure 4.4: *Snow accumulation predicted by different methods, plotted at the front mudflap of a Volvo FH truck.*

front mudflap. It is observed that the entire region is dominated by high wall shear stress which indicates that there is no snow accumulation there. However, this does not agree with data obtained from field tests. Figure 4.4(b) depicts the snow accumulation, predicted with UDF4, on the lower portion of the front mudflap. It is observed that more than half of the surface is covered with a moderate amount of snow, while the inner part shows no signs of contamination. Compared to the test data, this is an improved prediction although the method still does not capture the accumulation at the inner part of the wheelhouse. Nevertheless, the results are improved compared to the outcome of the wall shear stress method shown in Figure 4.4(a). Figure 4.5(a) shows wall shear stress plotted at the lower part of the rear mudflap. In this case, the result differs a lot compared to the front mudflap. The majority of the surface is dominated by low wall shear stress, with the exception of the bottom right corner (bottom left in Figure 4.5(a)) and upper left (top right in Figure 4.5(a)), where higher values are observed. This indicates that most of the wheelhouse is covered with snow. While this result is more in agreement with experimental data, the amount of snow accumulation that is predicted through evaluating the wall shear stress is significantly different compared to field test results. In the case of the rear chassis mudflap, presented in Figure 4.5(b), UDF4 predicts a uniform distribution of snow accumulation on the surface while capturing the amount of snow with good accuracy. This result is a vast improvement over

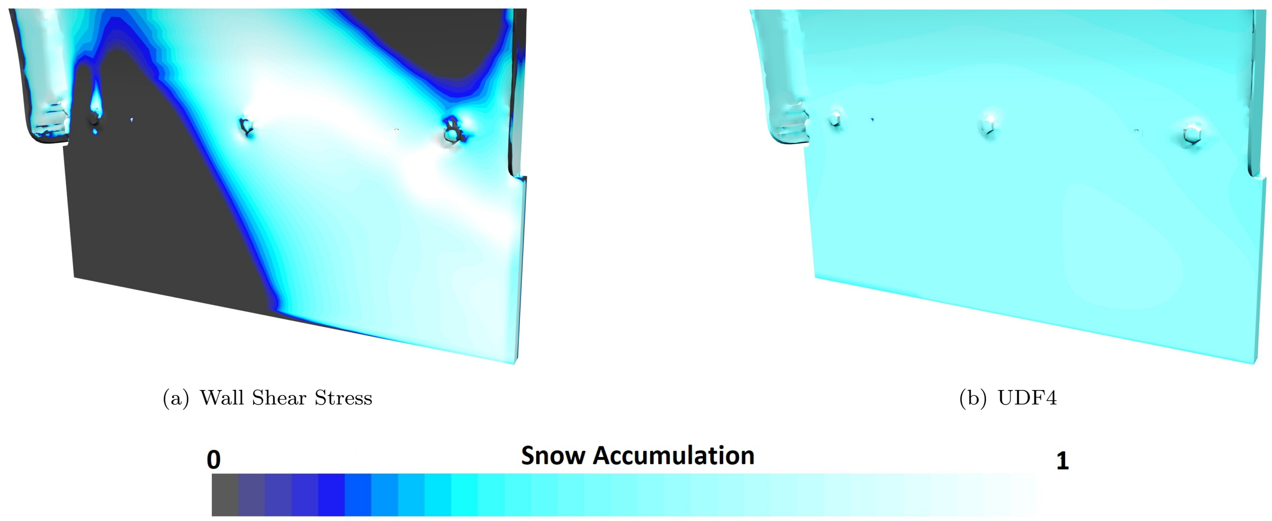

Figure 4.5: *Snow accumulation predicted by different methods, plotted at the rear mudflap of a Volvo FH truck.*

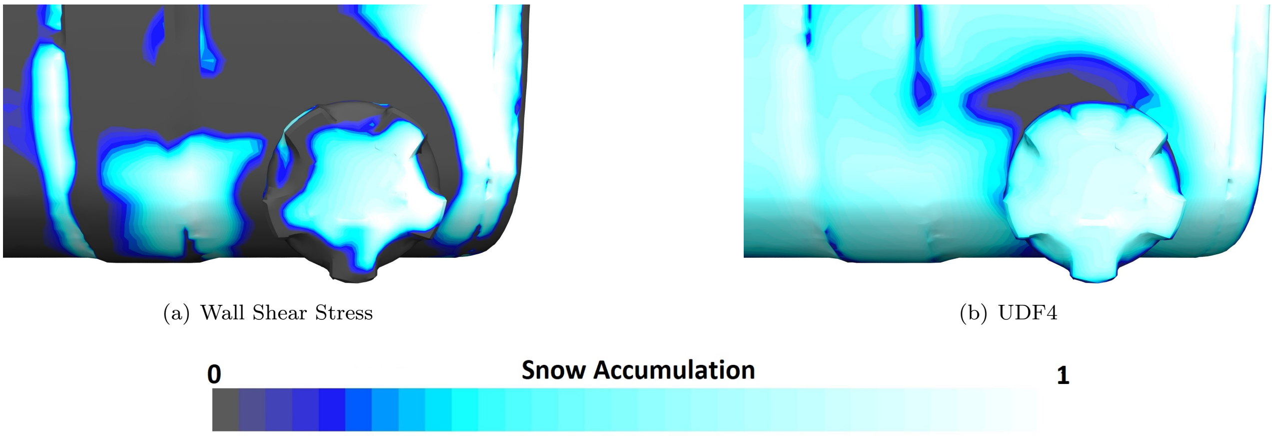

(a) Wall Shear Stress (b) UDF4

Figure 4.6: *Snow accumulation predicted by different methods, plotted at the top of the fuel tank of a Volvo FH truck.*

the one obtained using only wall shear stress values (Figure 4.5(a)), which exhibits a non-uniform distribution ranging from no accumulation to very large amounts of snow packed on the mudflap surface.

Top of chassis

Another region of importance is the top of the truck's chassis. Figure 4.6(a) shows part of the top of the truck's fuel tank. Low wall shear stresses are observed on the largest portion of the surface, with only small areas showcasing higher values. This indicates significant amount of snow accumulation on top of the tank, which is in agreement with experimental results. The snow distribution is not uniform. The rear portion of the tank has high levels of snow accumulation. Additionally, snow is observed on top of the fuel tank cap as well as the outer section of the tank. The inner parts of the tank showcase little to no contamination. This results differs significantly from the field test data with the exception of the tank cap which has a similar pattern. Figure 4.6(b) shows the predicted snow packing on a portion of the top surface of the fuel tank, when UDF4 is used. The obtained snow distribution is more uniform compared to the one predicted by the wall shear stress method, shown in Figure 4.6(a). The only non-contaminated area is located next to the tank cap. The amount of snow accumulation is predicted quite accurately by the proposed method when validated against the test results, with the exception of the tank cap, where higher level of snow accumulation is predicted. For this specific area, the results obtained from the wall shear stress method are more accurate.

Additionally, Figure 4.7(a) shows part of the top of the rear chassis wheelhouse. Wall shear stress dis-

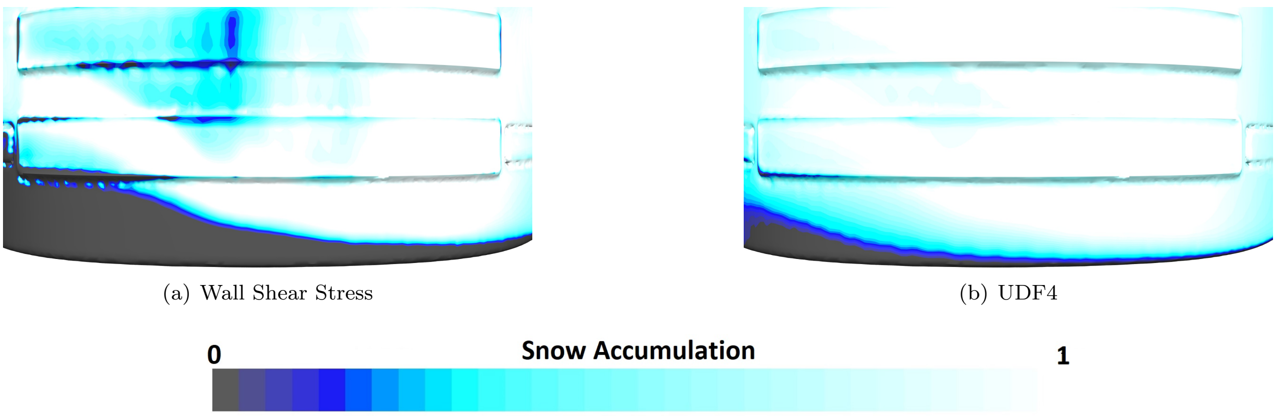

(a) Wall Shear Stress (b) UDF4

Figure 4.7: *Snow accumulation predicted by different methods, plotted at the top of the wheel cover of a Volvo FH truck.*

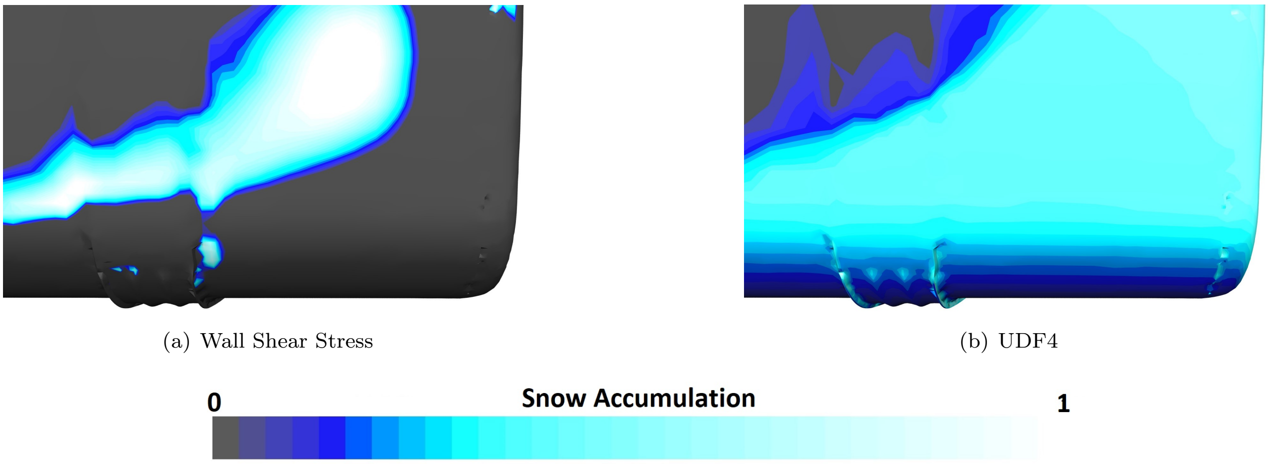

Figure 4.8: *Snow accumulation predicted by different methods, plotted at the lower side of the chassis of a Volvo FH truck.*

tribution indicates snow accumulation on most of the surface. The outer edge, however, shows no signs of contamination. Additionally, the snow distibution on the remaining surface is not uniform. The inner front section of the wheelhouse has smaller amount of snow compared to the rest of the contaminated area. UDF4 results for the rear chassis wheelhouse are shown in Figure 4.7(b). The proposed method predicts a fairly uniform snow distribution on the surface. Snow is removed only from a small portion of the outer front part of the wheelhouse. Compared to the wall shear stress method, the distribution of snow accumulation is better and the non-contaminated region is smaller which is in agreement with the test data.

Side of chassis

Finally, the two methods are compared in the lower side region of the truck's chassis, more specifically the side of the tank. Figure 4.8(a) shows the snow accumulation predicted by the wall shear stress method. A pattern can be seen at the lower part of the tank. The amount of snow is not uniform as it ranges from very low amount to very high amount of snow. The result obtained from implementation of UDF4 is presented in 4.8(b). The pattern at the lower part of the tank is also present in this case, but compared to the wall shear stress method it covers a larger area and is more uniform. A moderate amount of snow is predicted. This correlates better with data obtained from field tests.

4.1.4 Discussion

Velocity components

Utilization of normal velocity in order to approximate the particle impact velocity proves to be problematic. The criteria for normal and tangential velocity need to be satisfied for every surface and this results in the velocity exhibiting unphysical behavior in some regions. The quality degrades more when the number of surfaces that sit in close proximity increases. Note that Figure 4.1 depicts the simplified truck (the commercial truck model is not depicted for confidentiality reasons). One can expect that the situation will be worse in the commercial truck model which has a more complicated geometry. The chosen method for calculating the velocity components does not provide results of sufficient quality. It is hard to motivate the choice of an appropriate distance. An attempt to associate it with particle diameter is made but even very small distances e.g. 2 mm away from the truck are very big compared to the typical diameter of 0.2 mm that is encountered in snow smoke [2]. Additionally, the distance at which velocity components are evaluated is, most likely, different for the various regions of the truck, e.g. front, insteps etc. This would result in the creation of more complicated field functions and would make the method more sensitive to different vehicle geometries.

Wall shear stress

This method does not require any field function, hence it can be utilized for predicting the snow accumulation with no changes in a typical CFD workflow. As predicted, the comparison of the results from the steady-state CFD simulation and field testing prove that it is applicable to some of the surfaces of the truck that are considered relevant from the designer's perspective. The method manages to capture the snow accumulation patterns in some cases, e.g. at the front of the car, but not very well in other regions, such as the mudflaps and wheelhouses. Generally, it is not able to predict the correct amount of snow accumulation even in regions where the pattern matches the field test data. This is because of the fact that in this approach a set of important properties is not taken into consideration. Apart from the obvious constraints resulting from the usage of single phase flow properties only, this disagreement originates also due to disregarding the temperatures of the surfaces.

Proposed Method (UDF4)

The introduction of passive scalar and its combination with the wall shear stress produces results that are significantly improved compared to the wall shear stress method. The general patterns of snow accumulation are sufficiently predicted in most areas of the truck. Additionally, the amount of snow predicted correlates well with the field test results in most cases. Even in the case of the mudflaps, where different types of snow are involved, the proposed method manages to predict the snow packing on a large portion of the surface. This happens because of the extra conditions included in the field function to improve this specific area by accounting for the effect of wet snow which is more adhesive. The other properties that are included, especially the effect of surface orientation, help the method to achieve a more uniform distribution of snow in areas such as the top of the chassis. However, there are still limitations, when it comes to the accurate prediction of snow packing, especially in areas where other types of snow, except for snow smoke, are involved. At the front mudflaps for example, the method cannot fully match the field test data. The reason is that the region is dominated by high wall shear stress. Even when the effect of the wall shear stress is reduced above a certain threshold for passive scalar concentration, the inner part (left side in Figure 4.4(b)) cannot be covered in snow. The most probable explanation for this is that the front wheelhouse is a closed section, as it sits next to the engine and interior of the truck. Therefore, the airflow directs the injected passive scalar towards the outer section of the mudflap and does not allow for a high concentration at the inner portion of it. In contrast, the rear mudflaps that are situated in a more open space showcase a uniform accumulation because the airflow is directed both innerwards and outwards of the mudflap.

General observations

Snow accumulation differs depending on the regions of a vehicle. As mentioned in [2], large snow particles usually end up in the lower sections of a truck, i.e. in the rims, on the insteps and on the lower parts of the chassis. These particles are characterized by relatively high Stokes number and do not follow the airflow closely. On the other hand, smaller snow particles - featuring low values of Stokes number - are lifted by the airflow higher and can accumulate e.g. on the windscreen, the grille, the lights and the doors of a truck. The snow accumulation at the front of the truck is concentrated at the central region. This happens mainly because of the stagnation region at the center of the truck. An additional factor are the cavities that exist both in the grille and at the grab handles. This means that snow that impacts those regions is trapped and cannot be removed. The same applies to various other cavities that exist around the vehicle, such as the insteps. The topology of a truck influences the snow packing significantly. From the performed analysis, it occurs that the accumulation of the snow is dependandt on the surface orientation. The surfaces which are horizontal and facing upwards are more prone to snow packing that the tilted surfaces. It is caused by the direction of the gravitational force acting on every snow particle, which can be favourable for snow accumulation if the direction of force is acting towards the surface. The surface orientation is especially important in the lower regions of a vehicle where the larger (thus heavier) particles are encountered, as the gravity effect is more significant for such particles. The snow tends to end up also in the splitlines, where it is trapped and the magnitude of wall shear stress is insufficient to remove it.

4.2 Experiment results

In this section, the results of the experimental part of the thesis are presented and discussed. At first, findings from the friction and adhesion tests are described and discussed, followed by the angle of repose experiment results. Note that all data presented in this chapter are normalized.

4.2.1 Ice-surface friction/adhesion tests

Results from the friction/adhesion tests are presented and discussed in this section. Note that both sliding angles and static friction coefficient values are normalized with the maximum value, obtained from the experiments. Figure 4.9(a) shows results obtained from static and continuous rotation tests for the smooth ABS plastic surface. At low temperatures, it is evident that the two tests follow the same trends although there is a difference in the measured angles, with static test angles being around 40% higher compared to rotation angles. However, at 0° C the obtained results differ a lot. In the case of the static test there is a large decrease in a sliding angle while for the continuous rotation test a small increase is observed. This different behaviour results in the largest angle difference between the two tests (at a specific temperature), with rotation angles being 150% higher compared to static angles.

Results obtained from both tests for rough ABS plastic are presented in Figure 4.9(b). The sliding angles measured in both cases showcase similar trends with fairly consistent differences between the respective measurements. At -20° C and -10° C, the sliding angles remain stable, while higher values are recorded at 0° C. At every temperature, continuous rotation test gives around 35% higher angles compared to the static test.

Results obtained from both tests for coated aluminum surface are depicted in Figure 4.10(a). At -20° C, the recorded angles for both tests are very similar, with differences in respective measurements increasing as temperature rises. The trends are somewhat similar, with a decrease in sliding angles from -20° C to -10° C and an increase afterwards. The main difference is the rate of increase. With the exception of -20° C, continuous rotation test gives higher angles compared to the static tests. At -10° C the difference in the sliding angle is around 200% while at 0° C, it is more than 500%.

Results obtained from both tests for non-coated aluminum are presented in Figure 4.10(b). Similar behaviour to the coated aluminum tests is visible, with similar angles at -20° C and bigger differences as the temperature increases. However, the main difference is that the two tests showcase different trends between

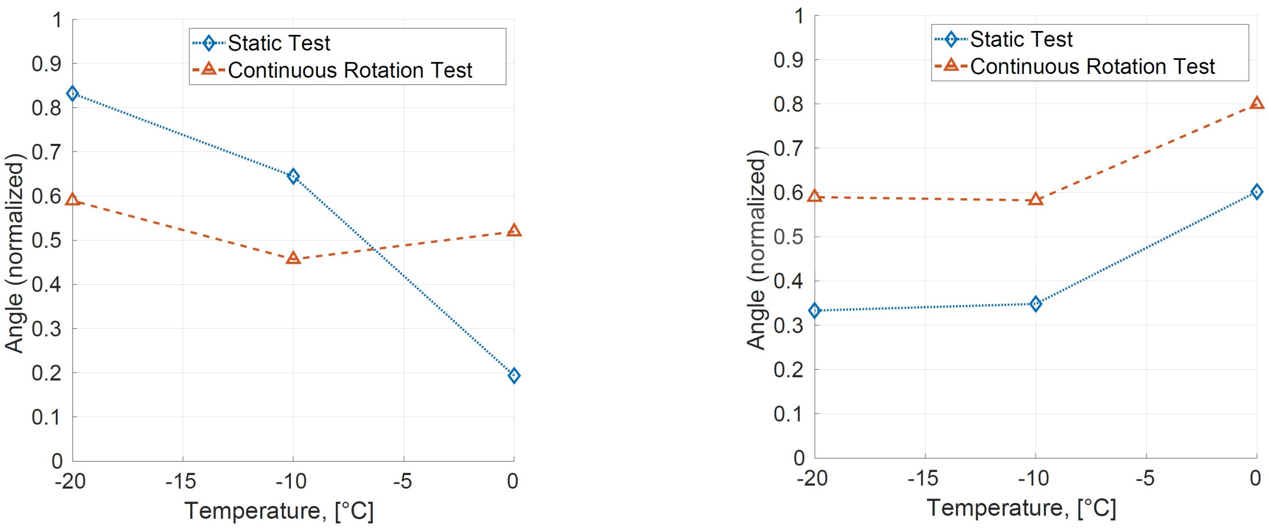

(a) Smooth surface ABS plastic.

(b) Rough surface ABS plastic

Figure 4.9: *Friction/adhesion test results obtained from the static and the continuous rotation tests for two ABS plastic surfaces with different surface quality.*

-10° C and 0° C. For static test, the sliding angles decrease further at 0° C, while for the continuous rotation test there is a significant increase in angle. Another difference is that the rotation test gives lower angles compared to the static test - except for the test at 0° C. At -10° C, the difference is around 20% while at 0° C, the rotation test achieves around 75% higher angle compared to the static test.

Figure 4.10(c) depicts results obtained from the different tests on a glass surface. Static test gives the highest sliding angle at -20° C followed by a large drop at -10° C. The angle remains almost unchanged at 0° C. For the continuous rotation test, the drop in angle from -20° C to -10° C is much smaller and is followed by an increase at 0° C, reaching a similar angle to the one at -20° C. In general, differences between the angles obtained from the test have significant differences. Static test achieves higher angles at -20° C but lower angles at -10° C and 0° C.

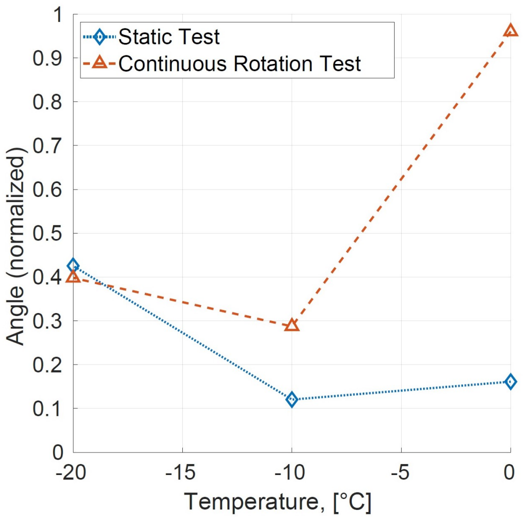

(a) Coated aluminum surface.

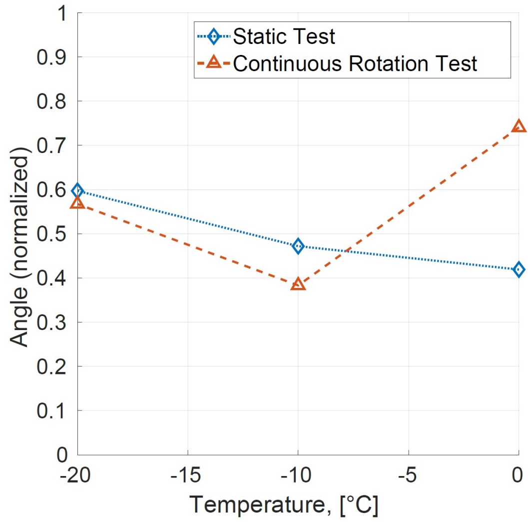

(b) Non-coated aluminum surface

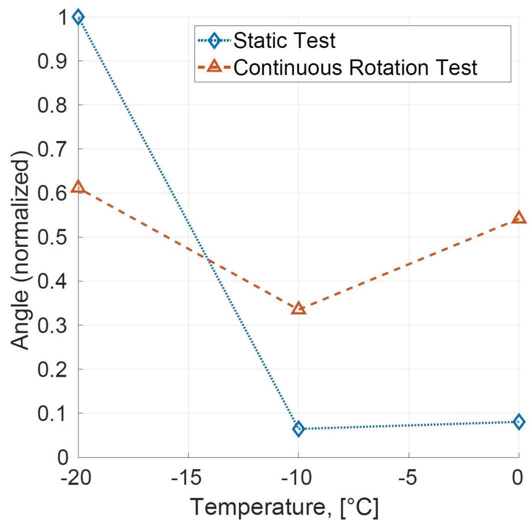

(c) Glass surface

Figure 4.10: *Friction/adhesion test results obtained from the static and the continuous rotation tests for two aluminum surfaces with different surface finish as well as a glass surface.*

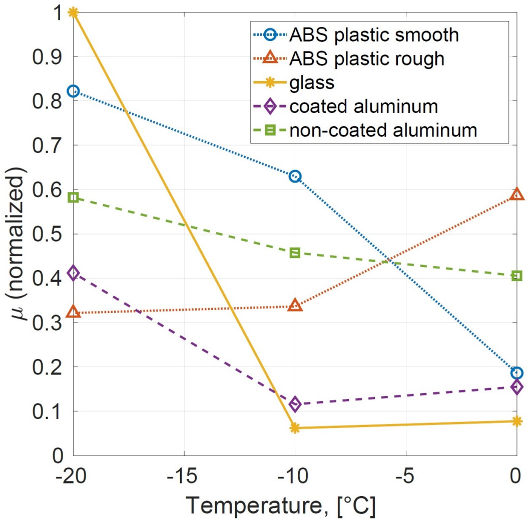

(a) Comparison of static friction coefficient results between different materials, obtained from the static test.

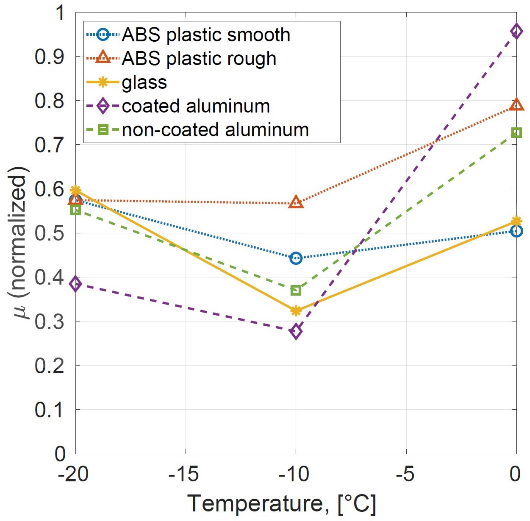

(b) Comparison of static friction coefficient results between different materials, obtained from the continuous rotation test.

Figure 4.11: *Snow accumulation predicted by different methods, plotted at the top of the wheel cover of a Volvo FH truck.*

4.2.2 Comparison of different materials

Static test results for all materials are presented in Figure 4.11(a). In most cases, significant differences are observed between the tested materials at the same temperature. There is a general trend of decrease in static friction coefficient from -20° C to -10° C for all materials, apart from the ABS plastic with rough surface for which a slight increase is observed. Between -10° C and 0° C there is a bigger spread in the behaviour of materials. For smooth ABS plastic and non-coated aluminum the decreasing trend continues. For glass and coated aluminum there is a minimal increase in static friction coefficient. Finally, for rough ABS plastic there is a significant increase in static friction coefficient. Glass showcases the biggest decrease, being the material with the highest static friction coefficient at -20° C and the lowest at the remaining temperatures. Smooth ABS plastic has the second biggest decrease, from -10° C to 0° C. Rough ABS plastic behaves differently, featuring an increase in static friction coefficient in the same temperature range.

Continuous rotation test results for all materials are showcased in Figure 4.11(b). Similar static friction coefficient values at -20° C are observed for all materials, with the exception for coated aluminum, for which a lower value is calculated. At -10° C a general trend of decrease in static friction coefficient is observed for all materials, except for the rough ABS plastic. Larger differences between the different materials are visible at this temperature compared to -20° C. At 0° C, an increasing trend in static friction coefficient is observed for all materials. Coated aluminum showcases the biggest increase in sliding angle. This material is characterized by the lowest value at -10° C and the highest at 0° C.

4.2.3 Effect of adhesion

The results of the continuous rotation tests are analysed further in order to determine if adhesion affects the ice-surface friction. The ice cubes are grouped by certain criteria which include residence time, temperature and material. At first, the ice cubes are grouped only by residence time and the average sliding angles are calculated. The results are presented in Figure 4.12(a). It is observed that there is a small increase in sliding angle when the residence time increases, although the difference in angles is very small.
Figure 4.12(b) shows results for data grouped by residence time and temperature. At 0° C, the trend line indicates that an increase in residence time results in an increased sliding angle. At -20° C, it is visible that residence time does not affect adhesion. Finally, at -10° C the shape of the trend line indicates that there is no clear tendency when it comes to the influence of residence time on the sliding angle.

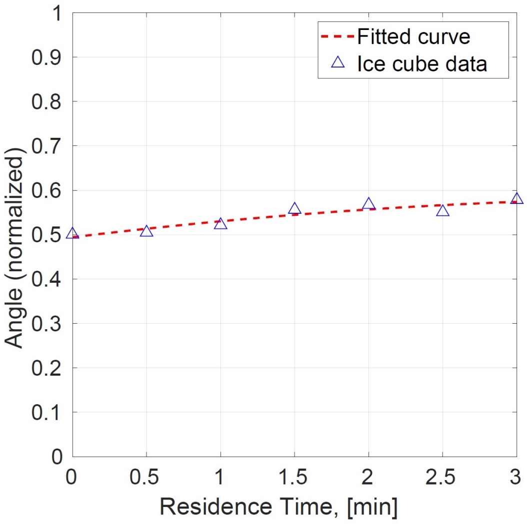

(a) Average sliding angles for data grouped by residence time.

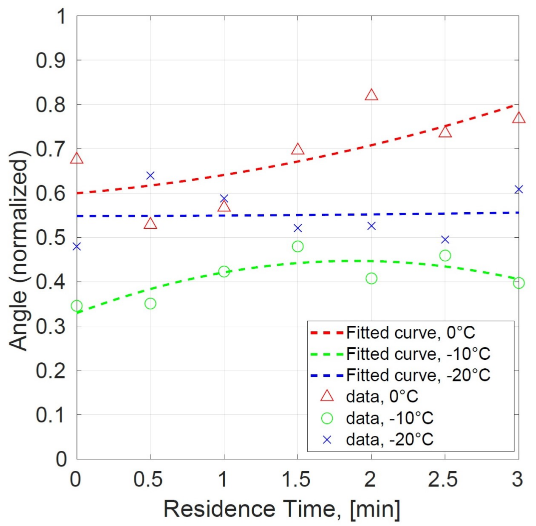

(b) [Average sliding angles for data grouped by residence time and temperature.

Figure 4.12: *Analysis of the adhesion effect, performed for different groupping criteria of the results.*

4.2.4 Angle of repose test

In this section, results from the angle of repose tests are presented. Results from experiments with crushed ice are presented first, followed by results for the substitute materials. Note that all results are normalized with the maximum angle of repose obtained from tests with crushed ice.

Rubber

Results obtained for the rubber surface are presented in Figure 4.13(a). Generally, estimation using the equivalent triangle method gives consistently higher angles for the angle of repose compared to visual estimation. In most cases, except for the tests performed on rubber at -5° C, the difference between methods is around 0.15 angle counts. In both cases, the angle of repose follows the same trend. It is observed that an increase in

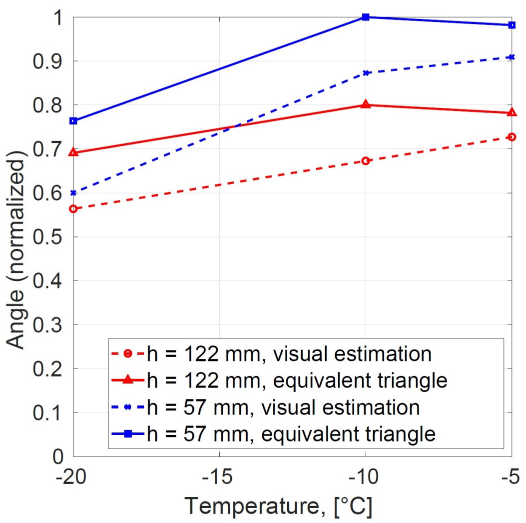

(a) Rubber surface

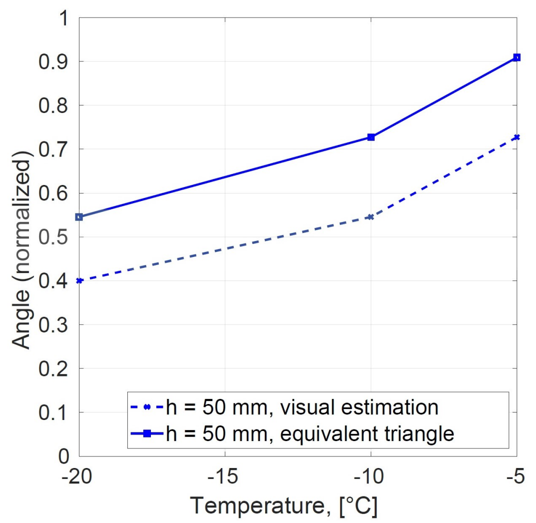

(b) Metal surface

Figure 4.13: *Angle of repose of sbow with respect to fall height. The angle is estimated with two methods: by eye and by calculating the projected area of the pile.*

falling height results in a decrease in the angle of repose. However, at -20° C, the difference between the results is relatively small. Another interesting observation is that the difference in angles between -10° C and -5° C when using Method 2 is very small, with the angle of repose at -10° C being higher than at -5° C.

Metal

Results for the metal surface are presented in Figure 4.13(b). The difference between the two angle estimation methods is consistent for the entire range of temperatures and is around 0.15 - 0.2 angle counts. For both methods, the lowest angle is observed at -20° C, while the highest angle is observed at -5° C. The difference between the angles at -20° C and -10° C is the same as the one between -10° C and -5° C. It indicates that as temperature increases greater changes occur in snow properties. A slightly larger fall height (67 mm) was tested only at -10° C, with the angle of repose being around 6% higher, compared to the standard fall height of 50 mm.

4.2.5 Substitute Materials for Snow

This section contains the results from angle of repose tests performed using substitute materials to replicate snow. Four different materials are evaluated. For every material, different levels of wetness are tested in order to investigate its effect on the angle of repose. Additionally, the effect of the falling height was evaluated - this experiment was performed only for the rubber surface. As mentioned previously, the angle of repose is normalized with the maximum angle obtained for crushed ice experiments. In some cases, the axes limits differ between graphs in order to allow for better evaluation of the trends.

Rubber

Results obtained from Material 1 tests on a rubber surface are presented in Figure 4.14(a). Three levels of wetness are tested in this case. It is observed that the least wet mixture behaves differently compared to the other two mixtures, which showcase the same trend and very similar angle values. Nevertheless, all the measured angles for Material 1 are very close to each other.

Figure 4.14(b) shows results obtained from Material 2 tests on a rubber surface. Four levels of wetness are evaluated for this material. Observation of the graphs indicates that the two mixtures with the least amount of water behave similarly, showcasing an increase in angle for larger fall height. On the contrary, the remaining two mixtures which contain larger amount of water exhibit a different trend, with the recorded angles decreasing when fall height increases. Similarly to the Material 1 test, all measurements are again very close to each other. Results obtained from tests using Material 3 on a rubber surface are presented in Figure 4.15(a). Three levels of wetness are tested in this case. For the mixture containing the largest amount of water the measured angles are the same regardless of fall height. The remaining two mixtures showcase the same behaviour, with smaller angles measured when fall height is increased. Again, all measurements are very close to each other.

Figure 4.15(b) depicts results obtained from tests performed using Material 4. It is observed that dry Material 4 behaves in a different way compared to wet Material 4. More specifically, angles measured for dry Material 4 decrease with increasing fall height. On the other hand, recorded angles for wet Material 4 increase with increasing height. An additional observation is that there is a big difference between angles measured for the two different tests.

Effect of wetness

The test data are analyzed further in order to determine whether different levels of wetness affect the behaviour of the material. Note that the axes of the graphs are different in order to allow for a better observation of the trends. A general observation is that for all materials, with the exception of Material 4, the results obtained for different levels of wetness are very similar.

The effect of wetness level on the angle of repose for the experiments performed with Material 1 is presented in Figure 4.14(a). In the case of the metal surface, the wetness level does not affect the angle of repose. For the rubber surface results depend on fall height. At a small fall height of 50 mm, there is a small increase in angle when the amount of water in the mixture is increased from a 2:3 to a 1:1 ratio. Further increase in the

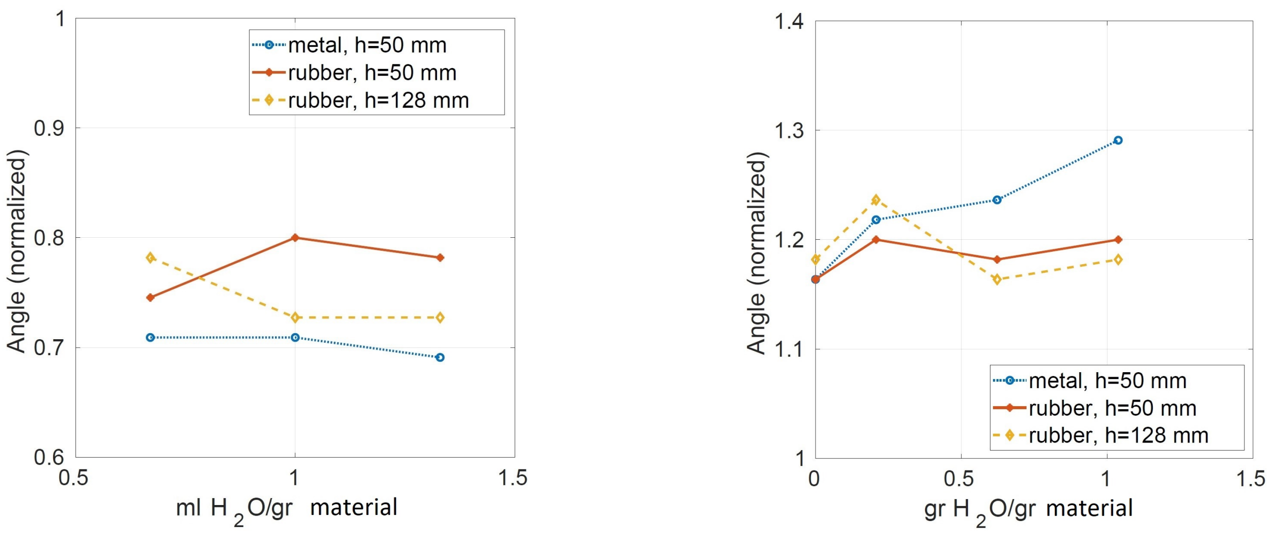

(a) Material 1

(b) Material 2

Figure 4.14: *Angle of repose of substitute materials with respect to level of wetness.*

amount of water results in a small decrease in the angle of repose. Increasing the fall height to 128 mm results in a different behaviour. When the ratio of water is increased from 2:3 to 1:1, the angle of repose decreases and maintains the same value for the 4:3 ratio.

Figure 4.14(b) shows the effect of moisture level on the angle of repose for the experiments performed with Material 2. For the metal surface it is observed that the angle of repose grows steadily as the amount of water in the mixture is increased. In the case of the rubber surface, the results follow similar trends with the highest angles recorded for a ratio of 1:5. An increase of water amount to a ratio of 2:5 results in a small decrease of angle. Further increase in the amount of water added to the mixture results in a small increase of angle. The effect of wetness on angle of repose for Material 3 is showcased in Figure 4.15(a). There is no effect of wetness on the results obtained for the metal surface; the same angle was recorded in every test. Results of experiments performed on a rubber surface with a fall height of 50 mm show an slight increase in angle when the wetness level grows from dry to a ratio of 4.3:5. Further increase in amount of water added contributes to a small decrease in angle. Changing to a larger height of 128 mm results in a small, yet steady increase in angle as the amount of water in the mixture rises.

Figure 4.15(b) shows the effect of wetness level on the angle of repose for the Material 4 tests. In general, for all materials and falling heights, there is an increase in angle as the amount of water increases. Metal surface experiences the biggest change, around 0.85 angle counts, with the lowest and highest angles recorded in this case. Nevertheless, for the two fall heights tested for rubber surface the increase in angle is also significant.

Comparison between substitute materials

For all materials tested, except for Material 4, it is observed that the angle of repose does not change significantly with level of wetness. Therefore, it is sufficient to plot one level of wetness for every material and see how they compare both with each other and with snow. For every material, apart from Material 1, the dry cases are chosen. Material 1 is always wet so the 1:1 ratio is chosen. Results are presented in Figure 4.16. Two distinct groups of materials can be seen on the figure. Materials 2 and 3 showcase very big angles of repose, much higher than those recorded for snow. Materials 1 and 4 showcase lower angles which fall between the results obtained for snow at -10° C and -20° C.

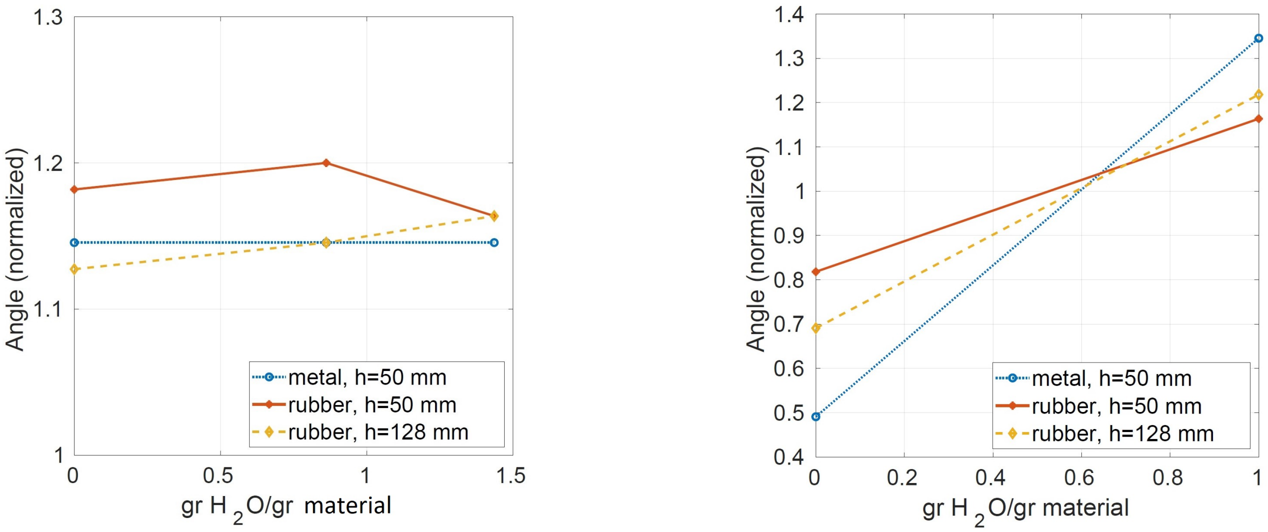

(a) Material 3 (b) Material 4

Figure 4.15: *Angle of repose of substitute materials with respect to level of wetness.*

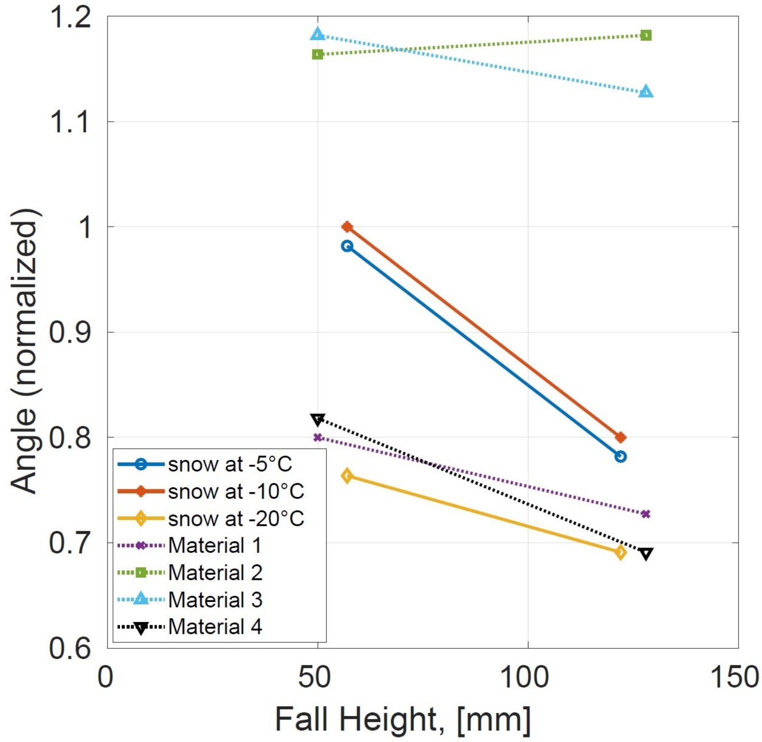

Figure 4.16: *Comparison of angles of repose for all tested substitute materials. Snow results are included. Note that there is only one level of wetness for every material (0 for all materials except for Material 1 where 1:1 ratio of water to material volume is used).*

4.2.6 Discussion

Friction and adhesion experiments

Adhesion affects the static friction coefficient, with the effect of it being more pronounced at 0°C. All materials are affected by adhesion as showcased by the increase in static friction coefficient values. This is contradictory to initial expectations that friction should decrease when temperature increases. The presence of a thicker liquid-like layer at higher temperatures should reduce friction and help the ice cubes to slide easier. The main explanation for this behaviour is that the temperature instabilities close to the melting point result in a melt-freeze cycle that causes increased adhesion to the surface. Indeed it was observed that when decreasing the temperature from around 0°C, it was harder to remove ice cubes from the tested surfaces, but also from the test section surfaces. At lower temperatures the effect of adhesion is less significant and this could indicate that the residence time is not the best option when it comes to accounting for adhesion.

When it comes to materials, the two aluminum surfaces showcase similar trends although sliding angles are generally lower for the coated aluminum surface. It seems that non-coated aluminum is less affected by adhesion compared to the coated aluminum. This is indicated by the smaller differences at every tested temperature and especially at 0° C. At temperatures lower than 0° C, the differences between the two tests for non-coated aluminum could be within the margin of error. Coated aluminum is probably the material that is most affected by adhesion, especially at 0° C. The ABS plastic surfaces behave differently when compared to each other. Smooth ABS plastic showcases trends that are similar to the expected ones, especially in the static test. Adhesion seems to affect it only at 0° C, while at lower temperatures the sliding angles are actually reduced when adhesion is taken into account. Rough ABS plastic exhibits the same behaviour for both tests. Its behaviour can be attributed to its surface finish. This is the material with the roughest surface and features a lot of grooves. Therefore the contact area between the ice cube and the surface can vary significantly. Additionally, in the case that the grooves are filled with water, which then freezes (this is possible close to the melting point) the surface behaviour could be affected significantly. The glass surface is the hardest material to test, especially when it comes to the static test, because of the very low sliding angles. However after analyzing the results, it could be said that the glass behaves generally as expected but is significantly affected by adhesion at higher temperatures. In general it is quite hard to evaluate which of the materials is the least affected by adhesion. Overall rough ABS plastic showcases the most stable behaviour for both tests while the coated aluminum is the material that is affected most when adhesion is taken into account.

The significant differences between materials for the static test could indicate that, when adhesion is not taken into account, material properties significantly affect friction. On the other hand, when adhesion is taken into account material behaviour changes; especially at lower temperatures, sliding angles have similar values. This could indicate reduced dependence on material properties at these temperatures. It is important to mention that a lot of factors could affect the results. Most importantly, the temperature was almost never stable since the test section has an opening to allow for the operation of the rig. Additionally, the fan used to adjust the temperature inside the test section, produced strong vibrations that clearly affected the ice cubes, which could be seen moving or rotating. This made it harder to evaluate sliding angles and increased the margin of error. Furthermore, the fan produced some airflow which could also affect the results. Human intervention also has a potential impact. Since the angle of the test surface was changed manually, any excessive application of force could cause the ice cubes to slide. A significantly higher amount of experiments would definitely make the results more trustworthy.

Angle of repose of snow

In general, the results of the angle of repose test follow the expected trends. Angle of repose decreases when height is increased, which is expected since more particles bounce off the surface. Additionally it depends on temperature, i.e. it increases when temperature increases. This happens because snow becomes more adhesive at higher temperatures, especially close to its melting point. In the case of the metal surface, results are clearer and the same trend is established with both methods of angle estimation, although there is a significant difference in the predicted values. In the case of the rubber surface however the angle of repose obtained at -5°C is smaller than expected. This could be attributed to many factors, the most important one being that temperature instabilities at temperatures close to the melting point of ice can significantly affect the results. Comparison of the angle of repose between the two materials shows a significant difference at every temperature, for similar fall height. Angles are higher for the rubber surface. One reason for this could be that the dimensions of the two surfaces are different. Rubber surface is much larger, with a diameter of 90 mm, compared to the metal surface which has a diameter of only 35 mm. Another contributing factor could be the difference in grids used for the different surfaces. For the metal surface a smaller grid with hole dimensions of 4mm x 4mm is used, while for the rubber surface the grid dimensions are 10mm x 7mm. In both cases larger particles/agglomerates could pass through the grid, for example long thin spikes. An interesting observation is that the snow pile showcases stronger adhesion to the metal surface compared to the rubber one. This can be explained both by differences in material and by differences in surface quality. The metal surface is significantly rougher than the rubber one.

Substitute materials

A general observation for all tested materials is that their behavior depends more on the shape of the grains than on the level of wetness. More specifically, materials with round shaped grains can approximate the behaviour of crushed ice. On the other hand, materials with irregular shapes and large contact area fail to approximate the desired behaviour. Contrary to expectations, no significant changes are recorded for different levels of wetness, with the exception of Material 4.

Qualitatively, the Material 1 properties did not seem to change when increasing the amount of water added to it. Therefore, the main change caused by addition of water is that the volume of the particles increases along with their mass. Adhesion is generally not affected since the angles of repose are generally close for both materials that are tested. The only abnormal results are those obtained for the least wet Material 1, where the angle of repose obtained from the large height is larger compared to the one obtained from the small height. This doesn't agree with expectations and also with the remaining levels of wetness that are tested. It could possibly be the result of flawed testing method since it was the first set of experiments performed. Therefore, it could be considered an outlier. Generally, Material 1 approximates the behaviour of crushed ice at -20° C.

Both Material 2 and Material 3 give very high angles, even in the abscence of water. One possible explanation is obtained when looking at the shape and morphology of the materials. Both types tested contain a large amount of spikes and wavy flakes of various sizes and shapes. The relatively large area of these flakes makes it easier to adhere to each other. Once the materials have been wetted they become stickier. Especially in the case of the small fall height the pile easily reaches the grid and expands in every possible direction, forming a shape that resembles a square. This can explain the small differences in the angle of repose between the different tests, as the limits are reached in most cases. A side effect of the pile being bounded, in some cases, by the grid is that removing the grid could cause a part of the pile to fall off as it lost support, thus altering the angle of repose. In general, the angles obtained using Material 2 and Material 3 are not comparable to any of the tests performed with crushed ice.

The results obtained for the metal surface, using dry Material 4, should probably be disregarded. The small area of the test surface combined with the large size of the Material 4 particles made it hard for the material to accumulate on the surface. This explains the very small angle of repose. In the case of rubber surfac,e the larger area allowed the material to accumulate and form a proper pile. An important observation is that Material 4 becomes very adhesive when water is added to it. This is easily observed by comparing the angles between dry and wet Material 4. In the case of metal surface, the difference is very big since the material could adhere easily, even on the small surface, and expand upwards. In general, Material 4, when dry, showcases similar behaviour to crushed ice at -20° C despite the fact that its particles are, on average, larger.

4.3 Multi-phase method for Snow Accumulation

In this section, results obtained from the simulations performed using the DEM framework are presented and discussed. At the beginning the in-built and user-defined Hertz-Mindlin contact force models are evaluated. Afterwards, the baseline simulation is performed and compared to the test data. Additionally, a sensitivity analysis is performed in order to investigate the influence of various parameters on the angle of repose. The final part of the section contains a discussion of the results.

4.3.1 Comparison between standard and custom contact force model

The coefficients of restitution, both for particle-particle and for particle wall interactions, need to be constant in space in the implementation of the Hertz-Mindlin model that is used by Star-CCM+. This is one of the main limitations when it comes to modelling the snow behaviour, as the coefficient of restitution is not a single, constant value in reality. The implementation of a custom contact force in order to model the normal coefficient of restitution better, is investigated as an alternative to the in-built contact force model. Although the computational cost of the custom model is significantly higher, making it an unviable option, it is interesting to compare the behaviour of the particles during the simulation. Figure 4.17(a) shows the particle behaviour after 0.46 s in the simulation, where the in-built contact model is used. It is observed that particles do not maintain the injection velocity but accelerate. Additionally, they bounce higher maintaining large velocities after the collision with the test surface. Figure 4.17(b) shows the behaviour of particles at the same point in time, but using the custom contact force model. The particles maintain the injection velocity and the collisions with the test surface result in the particles having lower velocities and reaching a lower height compared to the in-built model.

4.3.2 Baseline simulation

After evaluating different parameters, such as the contact force model, the injection velocity, the number of injectors and the particle flow rate, a baseline simulation is performed at the temperature of -10°C in order to compare the result to the angle of repose obtained from experiments. The experimental result is presented in Figure 4.18(a). Figure 4.18(b) depicts the snow pile created by the DEM simulation. In this case, the angle of repose is significantly higher (around 41% larger angle).

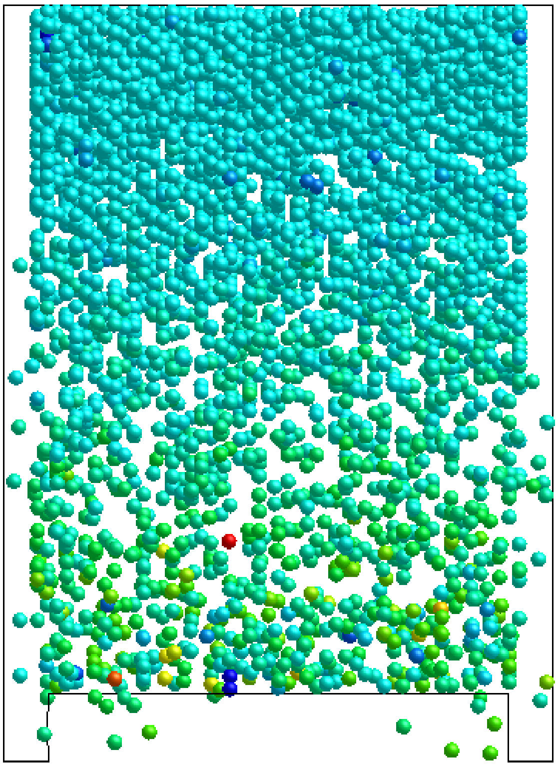

(a) In-built Hertz-Mindlin model.

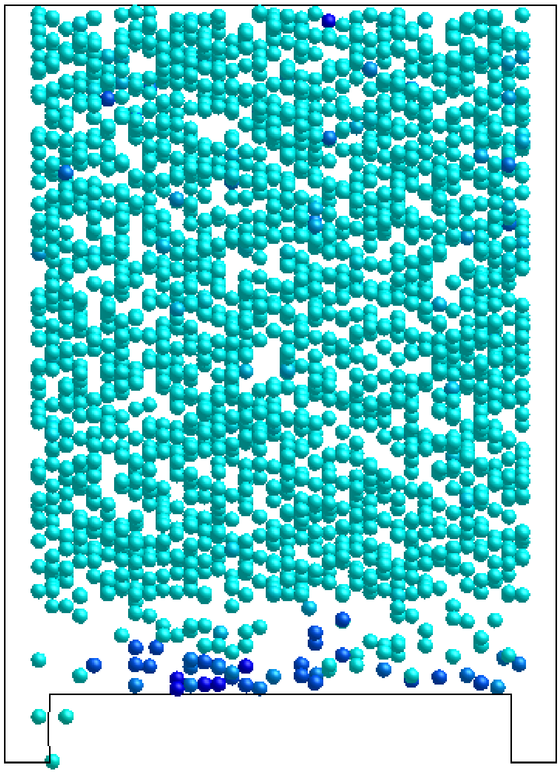

(b) Custom Hertz-Mindlin model.

Figure 4.17: *Comparison between the behaviour of particles in different contact models. Both screenshots are taken at 0.46 seconds of simulation time.*

(a) Experimental angle of repose

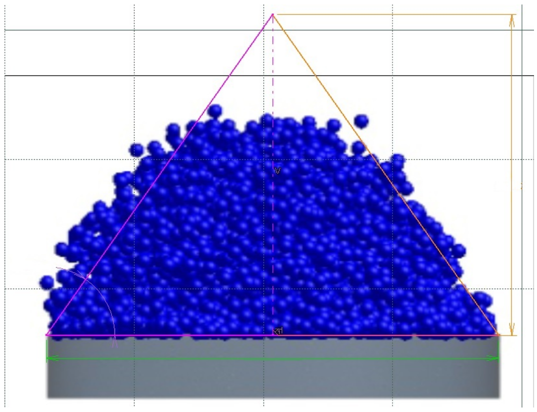

(b) DEM simulation angle of repose

Figure 4.18: *Comparison between the angle of repose obtained from experiments and the result of the DEM baseline simulation.*

4.3.3 Sensitivity analysis

This section contains the results of the sensitivity analysis performed for various parameters. These include:

- tangential coefficient of restitution for particle-wall interaction.
- tangential coefficient of restitution for particle-particle interaction.
- static friction coefficient for particle-particle interaction.
- Comparison between force proportional and contstant torque method for rolling resistance coefficient.

Tangential coefficient of restitution for particle-wall interaction

Two additional simulations are performed in order to evaluate the impact of the particle-wall tangential coefficient of restitution on the angle of repose of snow. The results, presented in Figure 4.19(a) are compared to the baseline simulation. As the tangential coefficient increases from 0.1 to 0.5 the angle of repose also increases. However, further increase of the tangential coefficient does not result in a big change in angle of repose. Instead, the obtained angle is slightly smaller

Tangential coefficient of restitution for particle-particle interaction

A similar analysis is performed to determine the effect of the particle-particle tangential coefficient of restitution on the angle of repose. Figure 4.19(b) shows the results of the simulations which are compared to the baseline simulation. As the values of the coefficient increase from 0.1 to 0.5 an increase in angle of repose is observed. However, further increase to 0.9 results in the lowest value obtained from this analysis

Static friction coefficient for particle-particle interaction.

The static friction coefficient for particle-wall interactions is taken from the experimental results. However, the inter-particle static friction coefficient needs to be determined from the literature[40], which suggests a range from 0.01 to 0.1 for this particular property. The sensitivity analysis therefore, aims to investigate the effect of this parameter on the angle of repose by checking values within this range. A comparison between the different simulations, presented in Figure 4.19(c), shows a linear increase in angle of repose as the static friction coefficient increases.

Comparison between force proportional and constant torque models for rolling resistance coefficient.

The final part of the sensitivity analysis consists of an investigation of the effect of rolling resistance coefficient method on the angle of repose. For both force proportional and constant torque methods the value of the

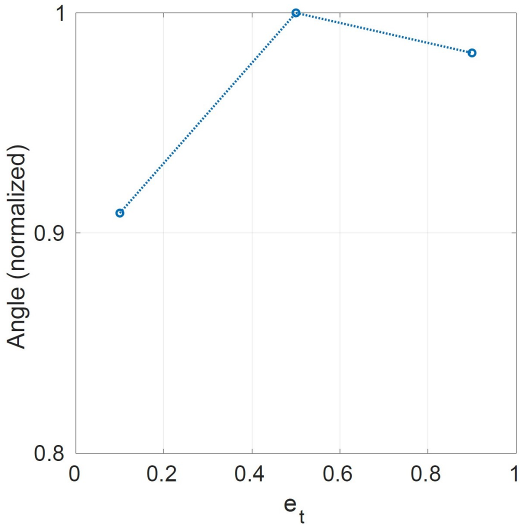

(a) Tangential coefficient of restitution for particle-wall interaction. Angle of repose obtained from DEM simulations.

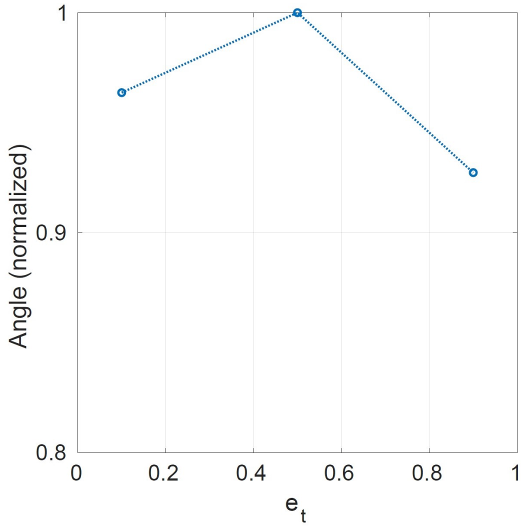

(b) Tangential coefficient of restitution for particle-particle interaction. Angle of repose obtained from DEM simulations.

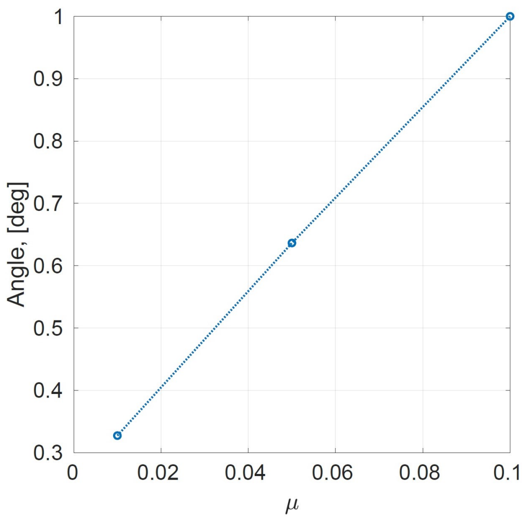

(c) Static friction coefficient for particle-particle interaction. Angle of repose obtained from DEM simulations.

Figure 4.19: *The sensitivity analysis is performed to investigate the effect of various parameters on the angle of repose of snow at -10° C.*

rolling resistance coefficient is the same. Results obtained from the simulations show that the choice of rolling resistance model affects the angle of repose; the force proportional model gives an angle of repose that is around 17% higher compared to the constant torque model.

4.3.4 Discussion

One of the main limitations of the in-built contact force model is that the coefficients of restitution need to be constant in space. This allows only for a single value to be used regardless of the particle size and the impact velocity. As expected, this can lead to a somewhat unphysical behaviour of the particles, both in particle-particle and in particle-wall interactions. The custom contact model replicates the particle behaviour better but is at least four (or even five) times slower. This is reasonable because it is not nearly as optimized as the in-built contact model. Additionally, it is prone to errors, since the development time is relatively small. Many simulations need to be performed in order to ensure that all the potential causes of errors have been predicted and eliminated, using appropriate conditions. The simplification of the parameters could be one of the factors that affect the result of the baseline simulation, which overpredicts the angle of repose compared to the experimental result.

The trends established for the tangential coefficient of restitution are different than expected, when it comes to the largest values tested. The main reason for this is that the angle of repose that is reached when the simulation ends is not the final one. Indeed, the particle count monitor in these cases shows that the number of particles still increases in the domain. The expected behaviour would be to have oscillations around a certain number of particles, which would indicate that the pile has reached its final size and is destroyed and rebuilt periodically. The creation of a stopping criterion based on the particle count in the domain eliminate that problem. However, there is a risk that this criterion would result in some simulations taking much more time, which is undesired given the time limits of the project. This is the main reason for limiting all simulations to a maximum of five seconds of simulation physical time.

5 Conclusions

The objective of this project was to provide Volvo Group with a viable tool for predicting snow accumulation over external surfaces of commercial vehicles. This goal required more in-depth understanding of snow and ice characteristics and the most severe scenarios of surface contamination due to snow. The tools used for development of the method involved both single and multiphase CFD simulations, as well as experimental methods. In this chapter, the conclusions drawn from the obtained results are presented. The discussion on the results is followed by the suggestions of possible future work on the analysed topic.

5.1 Discussions

The velocity components, obtained from the implemented method, behave in a non-physical way in many regions close to the truck's surfaces. The original idea was to approximate the impact velocity of snow particles by evaluating the normal velocity at a certain distance from the truck. It was concluded that this is not possible, using the implemented method. Even in the case that this approximation is possible, it would be hard to motivate the chosen distance and associate it with a certain parameter, e.g. particle diameter. Furthermore, it is expected that distance varies depending on the location around the truck. For example, in a vicinity of regions where the airflow approaches stagnation this distance should be different compared to e.g. regions around the wheels. There, the approximation of snow velocity with the velocity of the airflow (motivated from low values of Stokes number) is not valid. Therefore, the reasons why this approach was not successful are the complexity of the involved physics and the limitations of the software.

The introduction of a passive scalar could eliminate the problems associated with the use of only velocity components to predict the behaviour of snow particles. The developed method does not require any custom input from the user and was successfully validated for two truck models. For these reasons, this approach is perceived as a very useful and accurate method for predicting the accumulation of snow over the entire truck without a need for more advanced simulation tools. Therefore, it can be used for a quick evaluation of possible snow packing patterns during the design of a truck. This is a big improvement compared to the use of only aerodynamic properties, e.g. wall shear stress, which have limited capabilities in correctly predicting both patterns and amount of snow accumulation. The drawback of this method is that it requires the calculation of passive scalar, which is increasing the computational cost of the method. Moreover, although successfully validated, the method is based mostly on empirical observations and might lose its accuracy when the simulated case differs much from the evaluated ones.

In the climate chamber test, the sliding static friction coefficient between ice cubes and various materials in contact was measured. The tests were performed at three different temperatures. Then, the test was repeated with different residence time of the ice cubes on the surfaces. This was performed in order to assess what is the impact of residence time on ice-surface adhesion and what is the implication of this phenomenon on the static friction coefficient for sliding. The general trend that was observed is that the adhesion effect is more pronounced at temperatures closer to the melting point. This could be attributed to the melt-freeze cycles that happened due to temperature instabilities. Materials generally showcase different behaviour at -10° C and 0 ° C, whereas at -20° C differences are smaller.

The next experiment was the angle of repose test. In this case, the dependence of the temperature and surface material on the angle formed by the accumulating ice particles was analysed. During the tests the access to the testing specimen was restricted due to the geometry and specifications of the climate chamber, hence any human intervention inevitably entailed additional human error. Moreover, there were a few sources of environmental error. It was apparent that the vibrations within a chamber were significant and that the cooling fan generated certain airflow inside the chamber. Although the effect of the latter one was deemed less substantial, the former phenomenon could have affected the results vastly. Since this error can be treated as a random error, more tests could mitigate its effect on the results.

The angle of repose tests were repeated with the substitute materials. The temperature was not controlled during these tests and all of them were carried out at room temperature. Material 1 behaved very similarly to crushed ice. More specifically, Material 1 on the metal surface approximated crushed ice at -10° C. On the rubber surface, the results were similar to crushed ice at -20° C (the trend was almost identical). Angles obtained for the large height were also close to crushed ice at -5° C and -10° C. Dry Material 4 on the rubber surface achieved good correlation with crushed ice at -20° C. On the other hand, it could not form a realistic pile on the small cylinder due to the relatively large size of its particles. When wetted, the adhesion between this material and other surfaces was so strong that it did not resemble snow behaviour in any aspect. It is, however, possible that a lower level of wetness of Material 4 particles would make it more applicable for the desired usage. Material 2 and Material 3 tend to pile up to much larger angles than any other tested material, with the exception of wet Material 4. According to the observations, Material 2 and Material 3 could be used to resemble the fresh snow rather than crushed ice in its nature, as the fresh snow is more adhesive and has the same tendency to accumulate. Wetness of Material 2 and Material 3 does not seem to affect the angle of repose values significantly.

During the preparation of the multiphase CFD method, several attempts to reduce the computational burden were undertaken. They involved e.g. restriction of the domain to the cuboid that encloses the cylinder, imposing an escape condition on every surface (except for the upper surface of the cylinder), allowing for a dynamically adaptive DEM time step, selecting one-way coupling between the phases and limiting the number of forces to the crucial minimum. All these decisions are deemed logical and their possibly negative influence on the results is considered insignificant, compared to the benefits from reducing the simulation time. The choice of contact and linear cohesion models were based on the literature study and are considered reasonable for this application. One of the most intriguing problems was the definition of the coefficients of restitution (both normal and tangential) for particle-particle and particle-wall interactions. The final choice of selecting constant values for normal and tangential coefficients of restitution is rational from the perspective of the software, as the in-built Hertz-Mindlin contact model has been optimized. The simulations with this model employed are considerably faster compared with the simulations in which the contact model was customized. Nevertheless, constant coefficients of restitution do not allow for replicating the realistic behaviour of ice particles upon impingement with the wall or ice-ice particle collisions. This simplification is considered as a major drawback of the developed simulation tool. The choice of constant values was, however, justified given the time constraints of the project.

5.2 Conclusions

In this section, the conclusions of the performed work are gathered. First, the conclusions related to the literature study are presented. They are followed by the conclusions from the development of the simplified simulation method for snow packing, the conducted experiments and the preparation of the multiphase model.

5.2.1 Literature study

At the beginning of the project, an extensive literature study took place. Several research questions can be answered based on the information gathered during this part of the project:

- Snow smoke, which consists of small spherical particles that can end up very high on the surface of the vehicle, is formed in dry and cold environment.
- The particles at higher temperature have a higher tendency to stick to a surface.
- If the vehicle is driving in the snow environment without the presence of other vehicles, the snow is expected to depose mostly on the sides and in the lower sections.
- If the vehicle is following other vehicle (or vehicles), the snow particles are lifted from the ground and convected by the wake of a leading vehicle. These particles contaminate almost every external surface of the analysed vehicle. This type of snow-surface contamination comprises of primarily light and small snow particles (snow smoke).
- The surfaces where the values of wall shear stress are larger are expected to have lower snow accumulation. In this way, snow is expected to end up in cavities, grooves and wakes, hence in the regions where wall shear stresses are unable to remove snow.
- The surface roughness affects adhesion strength between snow and a surface. If the roughness of a surface is similar to the particle size, the adhesion strength reaches its maximum. Both greater and smaller roughness causes lower strength of adhesion.

- The highest adhesion strength between snow and other surfaces is expected when its Liquid Water Content is approx. 20%.

- The adhesion strength of ice increases with a decrease in temperature. It happens until the point when the liquid-like layer on ice disappears.

- Small particles accumulate on external surfaces which are higher above the ground compared to larger snow grains, which tend to accumulate on the lower surfaces, e.g. around the wheel rims or on the mudflaps.

- The material is susceptible to snow accumulation based on the snow particle-wall impact velocity regime. The material that showcases resistance to snow packing in a certain impact velocity regime might be vulnerable to snow accumulation in the other.

- The material with low E^* is supposed to be resistant to snow accumulation at the front of the vehicle and in other sections where high particle-wall impact velocity is expected.

- The material with high E^* is perceived to have low snow packing if the impact velocity is rather low. Such materials are therefore favourable in stagnation regions (e.g. cavities, etc.)

5.2.2 Simplified simulation method for snow accumulation

The purpose of the first part of the project was to develop a method that allows for predicting snow packing over an entire commercial vehicle without a need for utilizing computationally expensive multiphase frameworks. The following conclusions have been established:

- It occurred that using solely aerodynamic properties in order to assess snow accumulation properly is insufficient.

- A field function combining the passive scalar with aerodynamic properties and other selected properties achieved good correlation with field test data.

- The proposed method allows the designer to obtain information both about the patterns and the magnitude of snow accumulation on the vehicle.

5.2.3 Testing

The experimental part of the project was performed at Volvo Group premises. The research questions related to ice/snow testing are answered as follows:

- The proposed method of using the residence time in order to study adhesion is relatively simple while allowing the establishment of reasonable trends, given all the limitations and the additional factors that could affect the results.

- The friction-adhesion and angle of repose experiments proved that snow and ice are very complex material and testing of them requires a lot of preparation and effort.

- It occurred that both surface material and a temperature influence the ice-surface adhesion.

- The angle of repose tests showed the expected trends, which is that the angle of repose increases with increased temperature and that the angle increases with decreasing falling height.

- It occurred that testing the angle of repose with the substitute materials is much faster and way less sensitive to ambient conditions.

5.2.4 Multiphase simulation method

The final part of the project was the development of a multiphase CFD simulation tool that can replicate the angle of repose experiments.

- The DEM framework was selected for this purpose, as it was expected to model the physics in the most realistic way given the available resources. This modelling framework allows for studying both particle-particle and particle-wall interactions.
- The number of forces that act on the DEM particles was reduced to the crucial minimum. According to the literature study, incorporating only the drag force, the gravitational force and the forces resulting from the contact model was deemed sufficient.
- The Hertz-Mindlin contact model was used extensively for modelling the interactions of ice particles (both between each other and with other surfaces). The default model, however, did not allow for varying the coefficients of restitution in space, thus the ice physics was simplified substantially.
- Custom constant model was able to capture the physics more accurately, but the cost of the simulation increased significantly.
- The complexity of the contact model was insufficient to capture the behaviour of ice properly. The choice of forces, cohesion model and the formulation of thermomechanical properties (e.g. density, thermal conductivity, specific heat capacity, etc.) were deemed appropriate for this application.
- The choice of tangential coefficient of restitution for particle-particle and particle-wall interactions affected the results. For higher values of this parameter the time needed in order to obtain a final angle of repose was much larger.
- The sliding friction coefficient for particle-particle interactions had an impact on the angle of repose . It showcased a linear trend within the range of analyzed values.
- The choice of the rolling resistance model (with the same value of the rolling resistance coefficient) influenced the results. Higher angle of repose was obtained by using the force proportional model.

5.3 Future work

It occurred that aerodynamic properties of the airflow around the truck are insufficient for determining snow packing using the approach presented in this thesis. One of the mentioned reasons for this are the limitations of the software used for the development of this method. Nevertheless, is is believed that this field should be explored further as a single phase CFD simulations are generally less expensive in terms of computational resources and such methods would facilitate the design development of trucks (and other vehicles) considerably. The idea of a snow removing potential (SRP) metric presented in [10] should be investigated further. Such tool could then be applicable not only to snow contamination but also other types of contamination, such as soiling, etc. In the developed method, the only single phase aerodynamic property that was utilized in the final field function was the wall shear stress. The pattern obtained from visualising this property over the truck surfaces matches the in-field test data in many regions of the truck. This gives promising results and should be evaluated further, possibly combined with other aerodynamic properties, temperature data, surface orientation function, etc. Although the method was validated against two different truck models, more validation work needs to be performed in order to ensure that it is a generalized tool. This can be achieved by validating against various different vehicle geometries and configurations and, if possible, other, entirely different, vehicle types.

The sliding test for ice-surface friction had significant variation when it comes to the obtained results. As mentioned earlier, there are relatively many sources of errors that are involved in the performed testing. It would be therefore beneficial to repeat the tests in a more controlled environment where some of the before mentioned errors could be mitigated. It is suggested that the sample size should be increased in all the tests in order to assure statistical significance of the obtained results. Lastly, it might be interesting to compare the results obtained using different testing methods. When it comes to the angle of repose tests, it is definitely interesting to investigate the influence of the freezing path of ice cubes on the angle of repose. It is suggested that the test could be repeated with the ice cubes being frozen to the exact testing temperature, without so broad temperature changes that were encountered in the climate chamber tests that were performed during this project. It is also considered beneficial to repeat the tests in a more controlled environment where e.g. the temperature variations are reduced. For the substitute materials, it might be interesting to see the behaviour of a material much finer than Material 2 and Material 3 (but having similar properties). From a practical point of view, it would be ideal to conduct snow testing without the actual need for natural snow, as this could vastly reduce the costs of experiments. Therefore easily accessible materials (such as Material 2 and Material 3) should be investigated more as they do not require so controlled environment as in e.g. climatic wind tunnels. It might be also interesting to see the results of experiments performed with Material 4 with significantly lower wetness compared to the one that was evaluated in this project. Very promising results of the tests carried out with Material 1 lead to the conclusion that similar materials should also be considered. They could allow for performing the tests regardless of the temperature, which is generally a crucial parameter for snow and ice characteristics, but controlling this parameter in any large scale test is usually connected with significant costs.

The angle of repose tests were replicated using DEM multiphase framework. Given the time constraints of the project it was not possible to explore the utilization of the user-defined contact model more. Although the computation took more time, the initial results obtained with the custom contact force model were very promising. Therefore, the investigation of user-defined contact model in Star-CCM+ could be continued. In addition to this, it is of exceptional interest to investigate other multiphase frameworks that could allow for predicting snow packing over more complex geometries than the one used in the DEM part of the project. The literature study for this project proved that there have been successful attempts of using Unsteady RANS coupled with Discrete Phase Model or Lagrangian Particle Tracking with DEM-based regime maps for predicting snow patterns on various geometries. An interesting idea was presented in [20], where the coupling of steady-state RANS with DPM was used for predicting snow accumulation. It is advised to evaluate what is the cost and accuracy of this method compared to the one proposed in this work. These and other frameworks should be utilized for predicting the snow accumulation further, as it all contributes to creating a clearer picture of possible advantages and disadvantages of using any of these methods.

References

[1] Adrian P. Gaylard, Kerry Kirwan, and Duncan A. Lockerby. Surface contamination of cars: A review. *Proceedings of the Institution of Mechanical Engineers, Part D: Journal of Automobile Engineering* **231**.9 (2017), pp. 1160–1176.

[2] Per Abrahamsson, Matthias Eng, and Anders Rasmuson. An infield study of road snow properties related to snow-car adhesion and snow smoke. *Cold regions science and technology* **145** (2018), pp. 32–39.

[3] Tobias Eidevåg. "Snow Contamination of Cars: Collisions of Ice Particles with Surfaces". Licentiate Thesis. Chalmers University of Technology, 2020.

[4] U.S. Department of Transportation. *FHWA Road Weather Management*. 2021. URL: `https://ops.fhwa.dot.gov/weather/weather_events/snow_ice.htm` (visited on 03/28/2021).

[5] Hyuk-Jae Roh, Sandeep Datla, and Satish Sharma. Effect of snow, temperature and their interaction on highway truck traffic. *Journal of Transportation Technologies* (2013), pp. 24–38.

[6] Jonathan Jilesena, Ales Alajbegovic, and Brad Duncan. "Soiling and rain simulation for ground transportation vehicles". *7th European-Japanese Two-Phase Flow Group Meeting*. 2015, pp. 11–15.

[7] Adrian P. Gaylard et al. Insights into rear surface contamination using simulation of road spray and aerodynamics. *SAE International Journal of Passenger Cars-Mechanical Systems* **7**.2014-01-0610 (2014), pp. 673–681.

[8] Steven A. Lottes and Cezary Bojanowski. *Computer Modeling and Analysis of Truck Generated Salt-Spray Transport Near Bridges*. Tech. rep. Argonne National Lab.(ANL), Argonne, IL (United States), 2013.

[9] Behrouz Mohammadian et al. Experimental and theoretical studies of wet snow accumulation on inclined cylindrical surfaces. *Modelling and Simulation in Engineering* **2020** (2020), Article ID 9594685.

[10] Haiping Hong et al. "Numerical Investigation of Snow Accumulation on a Sensor Surface of Autonomous Vehicle". Apr. 2020. DOI: `10.4271/2020-01-0953`.

[11] Christoph Huber et al. Modeling and numerical calculation of snow particles entering the air intake of an automobile. *SAE International Journal of Passenger Cars-Mechanical Systems* **8**.2015-01-1342 (2015), pp. 538–545.

[12] Tobias Eidevåg et al. Modeling of dry snow adhesion during normal impact with surfaces. *Powder Technology* **361** (2020), pp. 1081–1092.

[13] Markus Enmark. "CFD Modeling of Snow Contamination on Cars. Implementation of a Snow Adhesion Regime Map by User Defined Functions". MA thesis. 2016.

[14] Anders Lind. "DEM Modeling of Snow-Wall Adhesion". MA thesis. 2016.

[15] Y.C. Zhou et al. Numerical investigation of the angle of repose of monosized spheres. *Physical Review E* **64**.2 (2001), pp. 021301-1–021301-8.

[16] Yeswanth Sai Tanneru. A DEM Study to investigate the influence of ice particle adhesion on the angle of repose (2020).

[17] Michiya Higa, Masahiko Arakawa, and Norikazu Maeno. Size dependence of restitution coefficients of ice in relation to collision strength. *Icarus* **133**.2 (1998), pp. 310–320.

[18] Carolin Willibald et al. Angle of repose experiments with snow: role of grain shape and cohesion. *Journal of Glaciology* **66**.258 (2020), pp. 658–666.

[19] Jiabin Wang et al. Numerical study of snow accumulation on the bogies of a high-speed train using URANS coupled with discrete phase model. *Journal of Wind Engineering and Industrial Aerodynamics* **183** (2018), pp. 295–314.

[20] E. Allain et al. "Experimental and numerical study of snow accumulation on a high-speed train". *49th International Symposium of Applied Aerodynamics*. 2014, pp. 24–25.

[21] Luyang Kang et al. CFD simulation of snow transport over flat, uniformly rough, open terrain: Impact of physical and computational parameters. *Journal of Wind Engineering and Industrial Aerodynamics* **177** (2018), pp. 213–226.

[22] Charles Fierz et al. *The international classification for seasonal snow on the ground*. UNESCO, Jan. 2009.

[23] Samuel C. Colbeck. Sintering in a dry snow cover. *Journal of Applied Physics* **84**.8 (1998), pp. 4585–4589.

[24] Jane R. Blackford. Sintering and microstructure of ice: a review. *Journal of Physics D: Applied Physics* **40**.21 (2007), pp. R355–R385.

[25] Daniel A. Miller, Edward E. Adams, and Robert L. Brown. A microstructural approach to predict dry snow metamorphism in generalized thermal conditions. *Cold regions science and technology* **37**.3 (2003), pp. 213–226.

[26] Samuel C. Colbeck. Classification of seasonal snow cover crystals. *Water Resources Research* **22**.9S (1986), pp. 59S–70S.
[27] Henri Bader. Minerological and structural characterization of snow and its metamorphism. *Snow and its Metamorphism* (1954), pp. 1–57.
[28] Michael Lehning et al. A physical snowpack model for the Swiss avalanche warning: Part III: Meteorological forcing, thin layer formation and evaluation. *Cold Regions Science and Technology* **35**.3 (2002), pp. 169–184.
[29] Masaaki Ishizaka et al. Relationships between snowfall density and solid hydrometeors, based on measured size and fall speed, for snowpack modeling applications. *The Cryosphere* **10**.6 (2016), pp. 2831–2845.
[30] Shoichiro Fukusako. Thermophysical properties of ice, snow, and sea ice. *International Journal of Thermophysics* **11**.2 (1990), pp. 353–372.
[31] G Dantl. Die elastischen moduln von eis-einkristallen. *Physik der kondensierten Materie* **7**.5 (1968), pp. 390–397.
[32] Michael Faraday. PHILOS MAG. *Philos Mag* **17**.113 (1859), pp. 162–169.
[33] Hans Helmut Gunter Jellinek. Liquid-like (transition) layer on ice. *Journal of colloid and interface science* **25**.2 (1967), pp. 192–205.
[34] Anne-Marie Kietzig, Savvas G. Hatzikiriakos, and Peter Englezos. Physics of ice friction. *Journal of Applied Physics* **107**.8 (2010), pp. 081101-1–081101-15.
[35] Lasse Makkonen. Ice adhesion—theory, measurements and countermeasures. *Journal of Adhesion Science and Technology* **26**.4-5 (2012), pp. 413–445.
[36] Jamie Heil et al. Relationships between Surface Properties and Snow Adhesion and Its Shedding Mechanisms. *Applied Sciences* **10**.16 (2020), 5407.
[37] Erland M. Schulson and Andrew L. Fortt. Friction of ice on ice. *Journal of Geophysical Research: Solid Earth* **117**.B12204 (2012).
[38] Samuel C. Colbeck. Pressure melting and ice skating. *American Journal of Physics* **63**.10 (1995), pp. 888–890.
[39] Frank Philip Bowden and T.P. Hughes. The mechanism of sliding on ice and snow. *Proceedings of the Royal Society of London. Series A. Mathematical and Physical Sciences* **172**.949 (1939), pp. 280–298.
[40] Francesco Braghin et al. *The engineering approach to winter sports.* Springer, 2016.
[41] Daisuke Kuroiwa, Yukiko Mizuno, and Masao Takeuchi. Micromeritical properties of snow. *Physics of Snow and Ice: proceedings* **1**.2 (1967), pp. 751–772.
[42] Alexandre Langlois et al. Presenting snow grain size and shape distributions in northern Canada using a new photographic device allowing 2D and 3D representation of snow grains. *Frontiers in Earth Science* **7** (2020), Article 347.
[43] Clayton Crowe, Martin Sommerfeld, Yutaka Tsuji, et al. *Multiphase flows with droplets and particles.* Ž, 1998.
[44] Kenneth G. Libbrecht. Physical dynamics of ice crystal growth. *Annual Review of Materials Research* **47** (2017), pp. 271–295.
[45] Kenneth G. Libbrecht. *Snow Crystal Morphology Diagram.* 2016. URL: `http://www.snowcrystals.com/morphology/morphology.html` (visited on 05/27/2021).
[46] Anton Kabanovs et al. *Experimental and computational study of vehicle surface contamination on a generic bluff body.* Tech. rep. SAE Technical Paper, 2016.
[47] Thomas Hagemeier, Michael Hartmann, and Dominique Thévenin. Practice of vehicle soiling investigations: A review. *International Journal of Multiphase Flow* **37**.8 (2011), pp. 860–875.
[48] Akio Takamura and Isao Saito. Prediction Snow Ingress into Air Intake System. *SAE International Journal of Passenger Cars-Mechanical Systems* **1**.2008-01-0249 (2008), pp. 200–207.
[49] Henk Kaarle Versteeg and Weeratunge Malalasekera. *An introduction to computational fluid dynamics: the finite volume method.* Pearson education, 2007.
[50] Bengt Andersson et al. *Computational fluid dynamics for engineers.* Cambridge university press, 2011.
[51] Lars Davidson. Fluid mechanics, turbulent flow and turbulence modeling. *Chalmers University of Technology, Goteborg, Sweden* (2017).
[52] Zellman Warhaft. Passive scalars in turbulent flows. *Annual Review of Fluid Mechanics* **32**.1 (2000), pp. 203–240.
[53] Paul Götzfried et al. Comparison of Lagrangian and Eulerian frames of passive scalar turbulent mixing. *Physical Review Fluids* **4**.4 (2019), pp. 044607-1–044607-21.

[54] Diego Donzis et al. The Turbulent Schmidt Number. *Journal of Fluids Engineering* **136** (June 2014), pp. 060912-1–060912-5. DOI: 10.1115/1.4026619.
[55] Dario Camuffo. Dry Deposition of Airborne Particulate Matter: Mechanisms and Effects. *Microclimate for Cultural Heritage* (1998), pp. 197–234.
[56] Yoshihide Tominaga and Ted Stathopoulos. Turbulent Schmidt numbers for CFD analysis with various types of flowfield. *Atmospheric Environment* **41**.37 (2007), pp. 8091–8099.
[57] Peter A. Cundall and Otto D.L. Strack. A discrete numerical model for granular assemblies. *Geotechnique* **29**.1 (1979), pp. 47–65.
[58] Alberto Di Renzo and Francesco Paolo Di Maio. Comparison of contact-force models for the simulation of collisions in DEM-based granular flow codes. *Chemical engineering science* **59**.3 (2004), pp. 525–541.
[59] S CD-adapco. STAR CCM+ user guide version 15.06. *CD-Adapco: New York, NY, USA* (2020).
[60] Yutaka Tsuji, Toshitsugu Tanaka, and T Ishida. Lagrangian numerical simulation of plug flow of cohesionless particles in a horizontal pipe. *Powder technology* **71**.3 (1992), pp. 239–250.
[61] Hugo C. Hamaker. The London—van der Waals attraction between spherical particles. *physica* **4**.10 (1937), pp. 1058–1072.
[62] Kenneth Langstreth Johnson, Kevin Kendall, and aAD Roberts. Surface energy and the contact of elastic solids. *Proceedings of the royal society of London. A. mathematical and physical sciences* **324**.1558 (1971), pp. 301–313.
[63] Colin Thornton. Granular dynamics, contact mechanics and particle system simulations. *A DEM study. Particle Technology Series* **24** (2015).
[64] L Schiller. Über die grundlegenden Berechnungen bei der Schwerkraftaufbereitung. *Z. Vereines Deutscher Inge.* **77** (1933), pp. 318–321.
[65] Roland Clift, John R. Grace, and Martin E. Weber. Bubbles, drops, and particles (2005).
[66] Aleksey V. Pichugin. Approximation of the Rayleigh wave speed. *Preprinted submitted to Elsevier Science. http://people. brunel. ac. uk/˜ mastaap/draft06rayleigh. pdf* (2008).
[67] William B. Baratuci. Learn Thermodynamics Workbook. *age* **8** (2003).
[68] Jianhua Huang. A simple accurate formula for calculating saturation vapor pressure of water and ice. *Journal of Applied Meteorology and Climatology* **57**.6 (2018), pp. 1265–1272.
[69] Shahram Farhadi, Masoud Farzaneh, and Sergei A. Kulinich. Anti-icing performance of superhydrophobic surfaces. *Applied Surface Science* **257**.14 (2011), pp. 6264–6269.
[70] Sigrid Rønneberg, Jianying He, and Zhiliang Zhang. "Standardizing the testing of low ice adhesion surfaces". *Proceedings of the International Workshops on Atmospheric Icing of Structures (IWAIS)*. 2019.
[71] Lorne W. Gold. Some observations on the dependence of strain on stress for ice. *Canadian Journal of Physics* **36**.10 (1958), pp. 1265–1275.
[72] CES Granta's. EduPack. *Teaching resources for materials and process education. Available online: http://www. grantadesign. com/education* (2007).
[73] Maria Tikanmäki and Panu Sainio. Experiments on friction of dry and wet ice. *Cold Regions Science and Technology* **172** (2020), 102990.
[74] Tobias Eidevåg et al. Collisional damping of spherical ice particles. *Powder Technology* **383** (2021), pp. 318–327.
[75] Yoshihide Tominaga et al. Computational fluid dynamics simulations of snow accumulation on infrared detection sensors using discrete phase model. *Cold Regions Science and Technology* **180** (2020), pp. 103–167.
[76] Yoshihide Tominaga. Computational fluid dynamics simulation of snowdrift around buildings: Past achievements and future perspectives. *Cold Regions Science and Technology* **150** (2018), pp. 2–14.
[77] Jiabin Wang et al. Impact of bogie cavity shapes and operational environment on snow accumulating on the bogies of high-speed trains. *Journal of Wind Engineering and Industrial Aerodynamics* **176** (2018), pp. 211–224.
[78] Brian R. McAuliffe. *Potential for the accumulation of ice and snow for a boat-tail equipped heavy-duty vehicle*. Tech. rep. SAE Technical Paper, 2016.
[79] Jeffrey S. Marshall. Discrete-element modeling of particulate aerosol flows. *Journal of Computational Physics* **228**.5 (2009), pp. 1541–1561.
[80] Bjørn Egil Kringlebotn Nygaard, Hálfdán Ágústsson, and Katalin Somfalvi-Tóth. Modeling wet snow accretion on power lines: improvements to previous methods using 50 years of observations. *Journal of Applied Meteorology and Climatology* **52**.10 (2013), pp. 2189–2203.

[81] Roberto Moreno-Atanasio. Energy dissipation in agglomerates during normal impact. *Powder technology* **223** (2012), pp. 12–18.

A Appendix 1

Introduction

The aim of the experiments performed during this project is to gain more understanding of the phenomena that affect ice-surface interaction and snow accumulation. Additionally, useful data can be extracted and used in the detailed multiphase model that is developed throughout this project. The main tests that are conducted are the following:

1. An ice-surface friction, static test. This aims to investigate the effect of temperature and material the effect of temperature and material on the friction coefficient.
2. An ice-surface friction/adhesion test. This aims to investigate the effect of adhesion on the ice-surface friction. Adhesion is taken into account by controlling the residence time of the ice cubes on the test surface.
3. A snow accumulation test. This aims to investigate the effect of temperature and material on the angle of repose of snow.

Background

Ice-surface adhesion is an important field of investigation, especially for the development of anti-icing surfaces [69]. There are four methods widely used in research for testing of ice-surface adhesion: Vertical Shear Test, Horizontal Shear Test, Tensile Test and Centrifuge Adhesion Test, as discussed in [70]. In this work, a simpler testing method is proposed. With this method, the friction coefficient is measured, but the adhesion force is introduced as an additional input alongside material, temperature and relative humidity.

In addition to the ice-surface adhesion tests, a snow accumulation test is performed to investigate how snow accumulates on different surfaces. In this case the measured property is the angle of repose of the accumulated snow. This type of test is typically performed using real snow as in [16]. However, the availability of real snow is limited and the creation of snow particles is complicated. In this work, a simplified approach, which uses crushed ice to replicate snow, is proposed. Additionally, different granular materials are tested to investigate the possibility of replicating the behavior of dry snow in room temperature conditions.

Objectives

The main objectives of the experiments are the following:

1. Investigation of the effect of temperature and material on the static friction coefficient.
2. Investigation of the effect of adhesion on sliding friction between ice and the surface material.
3. Investigation of the effect of temperature and material on the angle of repose of snow.

Equipment and materials

Equipment

Equipment needed to perform the test includes:

- Temperature sensors (one for ambient temperature and one for the test surface)
- Test rig. The test rig is described in more detail in the Test setup section.
- Ice cube molds. Silicone molds are used in order to allow for easier removal of ice cubes without damaging them.

- Ice crusher. Any kind of ice crusher can be used, e.g. a hammer or an ice crushing/shaving device. However, the choice of device will affect the size distribution of the produced snow.
- Grid. This is used to pour snow on the surface. The size of the grid affects the size distribution of the snow that falls on the surface. Two grids are used in this work, a 7 x 10 mm grid for the large surface and a 4 x 4 mm grid for the small surface.
- Measuring cup. This is used to measure the volume of the created snow.
- Spray bottle. This is used to add moisture to the substitute materials in order to alter their adhesive properties.
- Camera (preferably 2 action cameras and a DSLR or any other type of camera capable of producing high quality images). The action cameras are used to record the angles and the ice cube behavior on the test surface. The DSLR camera is used to take pictures of the snow pile, which can be analyzed using image processing software.

Materials

The materials tested for ice-surface friction/adhesion are presented in Table A.1. The materials tested for snow accumulation are presented in Table A.2.

Test setup

Test rig

In general, any kind of device that allows for secure placement and rotation of a test surface, can be used as a rig. However it needs to satisfy two conditions. The first is that it should be possible to lock the rotating surface into any desired angle. The second is that it should be possible to rotate the surface smoothly. As an example, the rig used when testing for this project is described in detail. The test rig, presented in Figure A.1, consists of two plates and a hinge that allows the top surface to be tilted. The base plate is made of wood and metal. Metal is used to ensure that the rig has a substantial weight which prevents it from moving. The top plate is smaller in size and features a frame on two of its edges. The frame ensures that the test samples stay in place when positioned on the plate. Additionally, double sided tape can be used to provide extra security. The angle of the top plate is controlled with a hinge. It can be locked at the desired angle with the use of a bolt. The addition of a protractor to the lower hinge part and a marker on the upper part can make the process of changing angle faster and more accurate.

Ice cube creation

Ice cubes are created using silicone molds, to facilitate the removal of the ice cubes without damaging them. It is essential that all the ice cubes used are of the same shape and size in order to have repeatability of the tests

Table A.1: Materials used in the ice-surface friction/adhesion experiments.

Material
ABS plastic with smooth surface
ABS plastic with rough surface
Coated aluminum
Non-coated aluminum
Glass

Table A.2: Materials used in the angle of repose experiments. Both materials used where of cylindrical shape. Their dimensions are included in the table.

Material	**Diameter, [mm]**
Metal	35
Silicone rubber	90

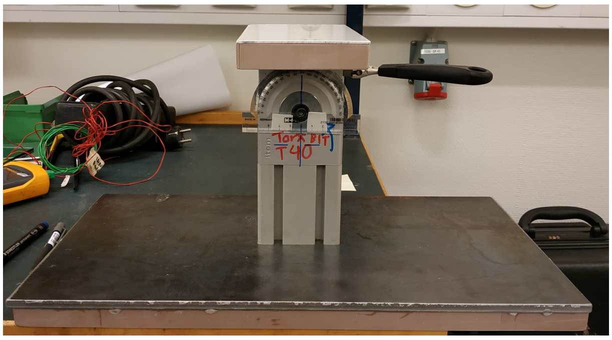

Figure A.1: *Picture of the test rig used for the friction/adhesion tests.*

and directly comparable results. It is more convenient to use square ice cubes.

Snow (crushed ice) creation

In the case that real snow is not available, an ice crusher (or ice shaver) can be used to replicate snow. It is essential to crush the ice in a low temperature environment in order to prevent it from melting and/or becoming sticky.

Adjustment of the wetness level of substitute materials

Adjusting the wetness level of a substance can significantly affect its adhesive properties. It is important to do this in a controlled way so that results are meaningful and comparable. Additionally, it is better if water is sprayed and the mixture is stirred simultaneously. This helps to avoid the entire mass of the material becoming a single entity, with all particles adhered to each other. In this work, a spray bottle is used in order to control the amount of water added to the material. Before starting the test, the amount of water that is released during one injection is measured. The specific spray bottle used for the experiments injects 1.35 g of water per injection. Table A.3 presents the typical amounts of water added to the test substances.

Test method

Ice-surface friction/adhesion tests

This section contains detailed description of all the steps required to perform each of the proposed ice-surface friction/adhesion tests.

Ice-surface friction static test

A simple drawing of the test process with all the relevant forces included, is presented in Figure A.2. The procedure is presented below:

1. Set the ambient temperature and relative humidity (or measure these properties if there is no way to control them).
2. Mount and secure the test surface on the support plate of the test rig.
3. Measure the surface temperature.

Table A.3: Materials used in the angle of repose experiments. Both materials used where of cylindrical shape. Their dimensions are included in the table.

Number of injections	**Water mass, [g]**
10	13.5
30	40.5
50	67.5

4. Set the angle of the top plate.
5. Position the desired number of ice cubes on the surface.
6. Record the number of ice cubes that slide.
7. Change material and repeat steps 3-6. If all materials are tested, go to step 8.
8. Change ambient temperature and repeat steps 3-7.

Ice-surface friction/adhesion test

The exact steps needed to perform this test are presented below:

1. Set the ambient temperature and relative humidity (or measure these properties if there is no way to control them).
2. Mount and secure the test surface on the support plate.
3. Measure the surface temperature.
4. Position the desired amount of ice cubes on the test surface. Each ice cube should be placed after a set amount of time. For this project, the time gap between placement of each ice cube is thirty seconds.
5. Change the angle of the top plate:
    - One option is to change the angle of the plate continuously until an ice cube starts sliding. The rotation is paused in order to record the angle and then it is resumed. This process is repeated until all ice cubes have slided. The advantage of this option is that there is no need to have a double-camera setup. However, there is increased probability that the results are affected by the repeated interventions in the test process. Additionally, it is harder to achive accuracy regarding the movement of ice cubes, especially in cases where a lot of them move in quick succession.
    - The second option is to use a double-camera setup in order to record both the ice cube movement and the angle at which this happens. In this case, the process is simplified to just rotating the test plate until all ice cubes have slided. It is important to position the camera properly so that the angle measurement is not distorted. Additionally, the start of the test should be marked (by shouting something or making a gesture) in order to make the synchronization of the two separate videos easier.
6. Change material and repeat steps 3-6. If all materials are tested go to step 7.
7. Change ambient temperature and repeat steps 3-7.

Snow accumulation test

This experiment is performed to investigate the effect of temperature and material on the angle of repose of the accumulated snow. Results from this test can be used to validate the DEM model results. A picture of the test procedure is presented in Figure A.3. Note that the grid support serves two purposes: it supports the grid and it defines the fall height. The best option is to use natural snow. However, availability of snow is usually

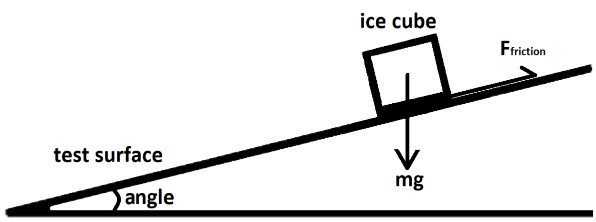

Figure A.2: *Simple drawing of the test process, including all the relevant forces.*

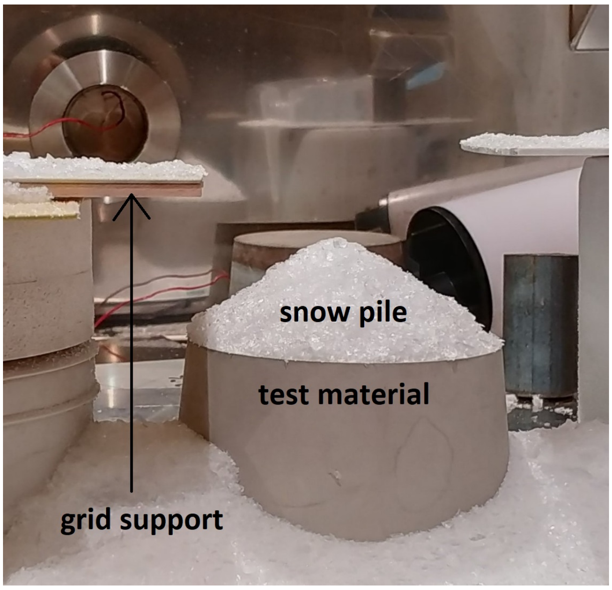

Figure A.3: *Angle of repose test setup.*

limited and therefore an alternative of using shaved ice is proposed. The same procedure (excluding the steps that refer to change of temperature) is used when testing substitute materials with the aim of evaluating the possibility of replicating snow. The test is performed as follows:

1. Crush ice using an ice crusher (alternatively the ice can be crushed with a hammer). An ice shaver is a better option since it can produce finer ice.

2. Place the crushed ice inside a measuring cup. Measuring the volume and mass of the ice will give its density.

3. Pour the ice over a sieve.

    - Ideally, a two-layer mesh consisting of a coarse first grid and then a finer one would help break ice clusters that might have formed and create a snowfall that consists of smaller particles. However this requires very fine snow (or crushed ice) and a low temperature. Otherwise, the bigger ice particles will probably stick together and clog the grid holes. Therefore, using a coarser grid might be a better option.

4. Shake the sieve in order to create snowfall. Shaking the sieve will help to break up particle clusters and create random particle injection.

5. Take a picture of the snow pile. Try to position the camera in such a way that the base of the pile is horizontal and the pile is centered in order to avoid having a distorted image.

Postprocessing of results

Analysis of static test results

The static test allows the extraction of the following data:

- temperature
- material on which the ice cube is tested
- angle (at which the ice cube is tested)
- percentage of ice cubes that slide at a particular angle

The main result of the experiment is the percentage of ice cubes that slide at a particular angle. Using this data the friction coefficient can be estimated. The angle that is used for the calculation is defined as the angle at which 50% of the ice cubes slide. The reasoning behind this decision is that the static friction coefficient is defined by the angle at which the ice cube is about to slide. Therefore, if half of the ice cubes are sliding and the rest remain still this can be a satisfactory approximation.

Analysis of continuous rotation test results

The continuous rotation test allows the extraction of the following data for each ice cube:

- temperature
- material (surface on which the ice cube is tested)
- residence time of the ice cube on the surface
- angle at which the ice cube slides

In order to analyze the effect of adhesion, the ice cubes can be groupped together using one or more of the available data. Residence time should always be taken into account since this is the parameter that defines adhesion. The following groups are created:

1. Data groupped by residence time. Using this groupping, a general trend for the effect of adhesion can be obtained, regardless of temperature and/or material.
2. Data groupped by residence time and temperature. Using this groupping, a trend for the effect of adhesion at different temperatures can be obtained, while the effect of material is ignored.
3. Data groupped by residence time and material. Using this groupping, a trend for the effect of material can be established, while the effect of temperature is ignored.

Note that by disregarding certain parameters it is not implied that they have not significant effect on adhesion. By creating groups with the same attributes, an attempt to isolate certain properties and study their effect on adhesion is made. An additional remark is that the sample population is reduced as the number of groupping criteria increases. This makes any conclusions less trustworthy and is the main reason for not groupping data by residence time, temperature and material. Curve fitting methods are used in order to capture trends related to adhesion. The method that is found to best fit the data is a quadratic polynomial curve.

Methods for estimating the angle of repose

In this section, two methods used to estimate the angle of repose of accumulated snow are described. When performing snow accumulation tests in the climate chamber, both methods are evaluated. Later, in the substitute materials experiments as well as the DEM simulations, the one considered more consistent is chosen.

Method 1 - Visual estimation

The first method used to estimate the angle of repose is rather simple. First, the image of the snow pile is checked to see if there is a need to rotate it in order to ensure that the base of the pile is horizontal. Afterwards the image is inported in a CAD software. The aim is to enclose the pile in an isosceles triangle that has a base length equal to the base of the snow pack. This method has the advantage of being simple and fairly quick. On the other hand it can lead to biased estimation of the angle of repose, especially since the snow pile is often non-symmetrical and its top can be flat. As a result the margin of error for this method is around ± 5 degrees. An example of angle estimation using this method is presented in Figure A.4(a).

Method 2 - Equivalent triangle method

The second method is used in [18] and takes a different approach. The aim is to calculate the projected area of the snow pile and then construct the equivalent isosceles triangle of equal area. The angle of repose can then be obtained. The projected area can be easily calculated using an image processing software. To simplify the process, the surrounding area of the snow pile should be of different colour with a high contrast to the colour

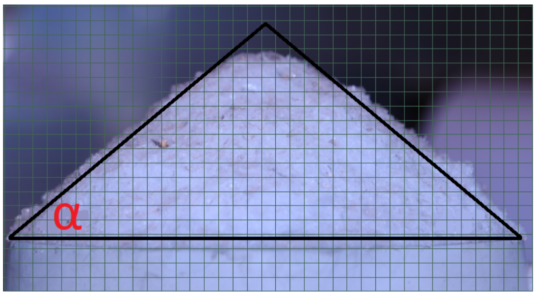

(a) Visual estimation of angle of repose

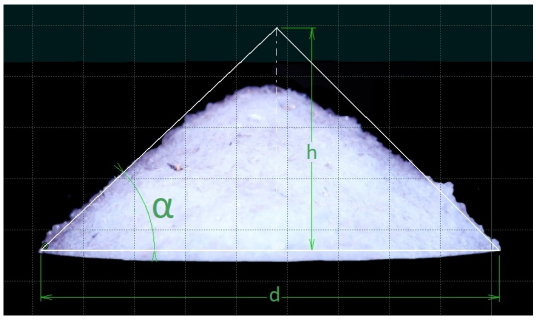

(b) Estimation of angle of repose with the equivalent triangle method.

Figure A.4: *Different methods of estimating the angle of repose. Visual estimation allows for a quick but possibly biased evaluation while the equivalent method provides a more consistent estimation.*

of the pile. Otherwise the background needs to be removed in order to clearly define the snow pile boundaries. After the area has been calculated, the equivalent isosceles triangle is constructed using CAD software. The margin of error is around ± 2 degrees. The main contributor to this error is the distortion from the camera. The CAD and image processing software contributions are deemed as very small. The main advantage of this method is that it gives an unbiased and consistent estimation, by disregarding potential non-symmetry of the pile. On the other hand it is more time consuming since it requires additional processing of the image. An example of angle estimation using this method is presented in Figure A.4(b). Note that this method will never give a angle of repose equal or greater than 90° since above this angle a triangle cannot be defined.

Recommendations

Best practice guidelines

The following recommendations are based on observations made during the experiments:

- One should always aim for the minimum possible interference with the experiment. Avoid opening the chamber door if there is no real need and try to do as much as possible through the test hole. Human presence in the chamber can affect temperature, humidity and add more forces to the balance. Therefore, the tests (especially the continuous rotation) should be performed as smoothly as possible, without applying any excessive forces.
- The temperature at which ice is created is important. The same applies to snow creation, which is especially problematic, since it needs to be done in the chamber.
- Temperatures close to the melting temperature are crucial. The behaviour of ice changes significantly with small changes in temperature in these regions. Monitoring the chamber and surface temperatures is important in order to ensure that the temperature is maintained at acceptable values. For example, if a test is performed at 0° C, but the surface temperature is higher, there is a risk of ice cubes melting on the surface, which would greatly affect the results.
- Camera position should be such, that the image is as less distorted as possible. This will reduce the margin of error when analyzing results.
- If possible, the snow pile and its surroundings should have a high contrast. Additionally, try to have a ruler or any other item of known size in the picture. This will result in easier processing of the image.

Alternative methods

The proposed method for taking adhesion into account relies only on residence time. An alternative method where a force is applied, in the direction normal to the test surface, in order to replicate adhesion would allow for a better study of the effect of adhesion. This alternative method, however, requires more complicated test setup in order to ensure the proper application of the force and the minimal human interference in the process.

DEPARTMENT OF MECHANICS AND
MARITIME SCIENCES
CHALMERS UNIVERSITY OF TECHNOLOGY
Gothenburg, Sweden 2021
www.chalmers.se

CHALMERS
UNIVERSITY OF TECHNOLOGY